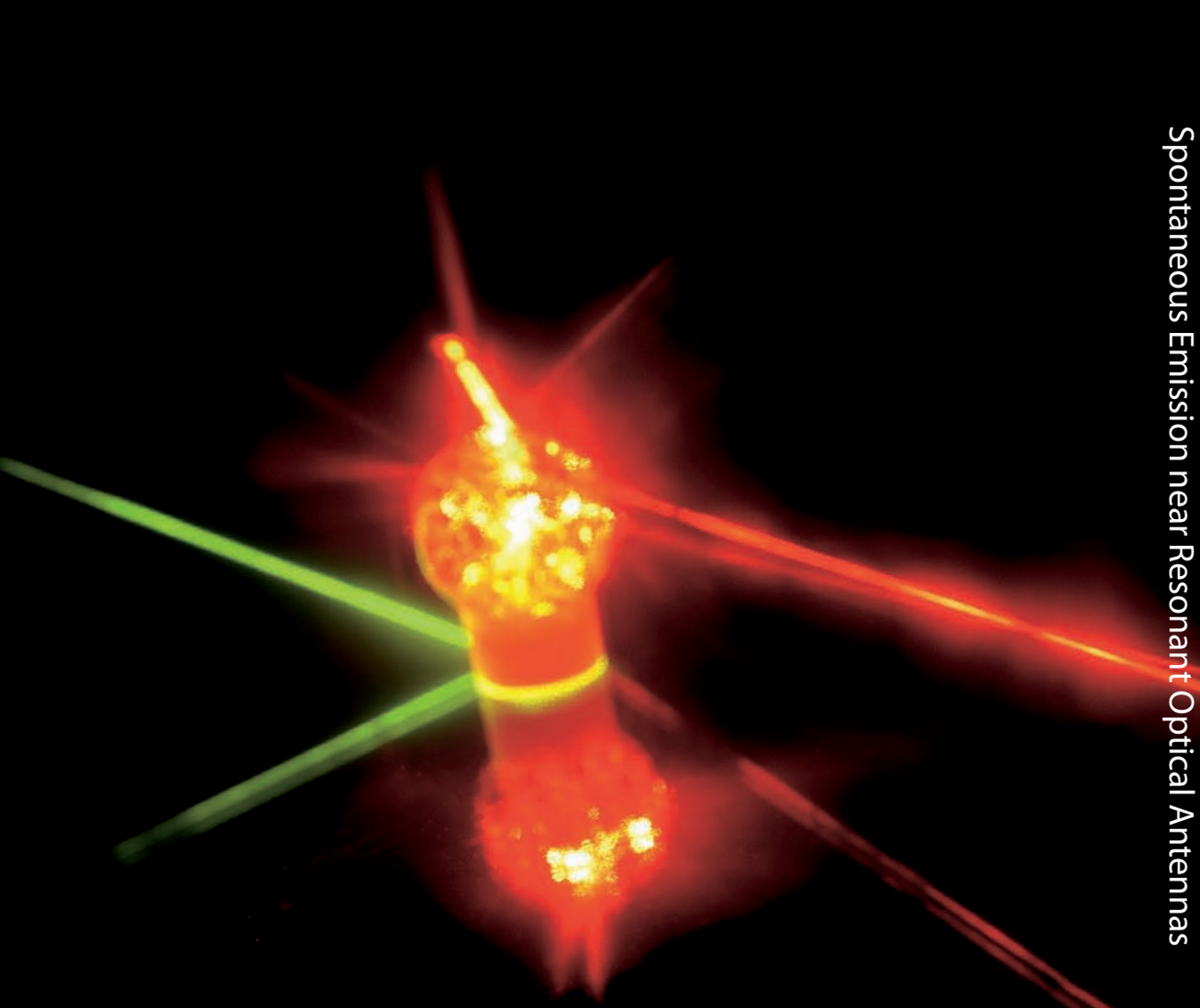

Spontaneous Emission near Resonant Optical Antennas Martin Frimmer 2012

Spontaneous Emission near Resonant Optical Antennas

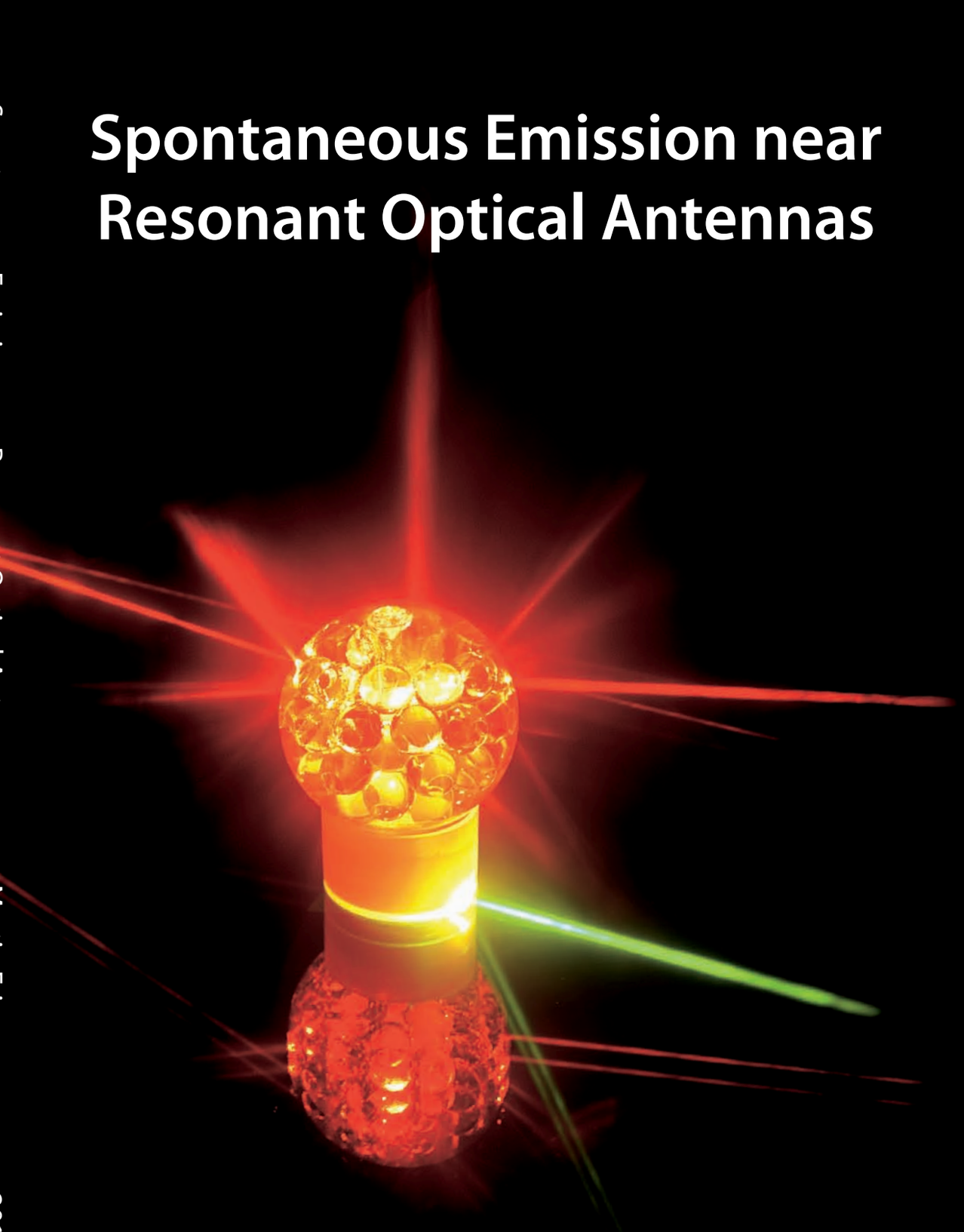

Martin Frimmer

Spontaneous Emission near Resonant Optical Antennas

Cover photograph by Henk-Jan Boluijt and Martin Frimmer.

Ph.D. thesis University of Amsterdam, November 2012
Spontaneous Emission near Resonant Optical Antennas
Martin Frimmer

ISBN 978-90-77209-68-4

A digital version of this thesis can be downloaded from http://www.amolf.nl.

SPONTANEOUS EMISSION NEAR RESONANT OPTICAL ANTENNAS

ACADEMISCH PROEFSCHRIFT

ter verkrijging van de graad van doctor
aan de Universiteit van Amsterdam
op gezag van de Rector Magnificus
prof. dr. D. C. van den Boom
ten overstaan van een door het college voor promoties
ingestelde commissie,
in het openbaar te verdedigen in de Agnietenkapel
op woensdag 14 november 2012, te 10 uur

door

Martin Frimmer

geboren te München in Duitsland

Promotor: prof. dr. A. F. Koenderink

Overige leden: prof. dr. M. Bonn
prof. dr. T. Gregorkiewicz
prof. dr. L. Kuipers
prof. dr. A. Lagendijk
prof. dr. M. Orrit
prof. dr. V. Sandoghdar

Faculteit der Natuurwetenschappen, Wiskunde en Informatica

The work described in this thesis is part of the research program of the
"Stichting voor Fundamenteel Onderzoek der Materie (FOM)"
which is financially supported by the
"Nederlandse Organisatie voor Wetenschappelijk Onderzoek (NWO)".

This work was carried out at the
Center for Nanophotonics,
FOM Institute for Atomic and Molecular Physics AMOLF,
Science Park 104, 1098 XG Amsterdam, The Netherlands,
where a limited number of copies of this dissertation is available.

Contents

1

Introduction

Light is the most fascinating part of the electromagnetic spectrum since it is mankind's most powerful probe of his environment. This Chapter first gives a very general introduction to the phenomenon of 'light' and its interaction with matter to then focus on spontaneous emission as a fundamental process of light-matter interaction. We introduce the fluorescence lifetime as one property of a spontaneous emitter that depends on and can be controlled by the environment. After acknowledging the giants on whose shoulders we stand we give a brief description of state of the art techniques to control various aspects of spontaneous emission to put our work into context. We conclude with an overview over the content of this thesis.

1.1 Electromagnetic radiation and light

While electric charges create electric fields and electric currents are the sources of magnetic fields, accelerated charges create electromagnetic radiation, a wave of related electric and magnetic fields which in vacuum travels at the characteristic speed of light and varies harmonically in space and time [1, 2]. Throughout this thesis with 'light' we refer to the visible part of the electromagnetic spectrum, which spans roughly from 400 to 650 nm in vacuum wavelength or equivalently from about 2–3 eV in photon energy. It is instructive to remind ourself why it is exactly this energy range that animals can perceive and plants can harvest. The answer to this question is that the photon energies of the visible spectrum match the energies of electronic excitations in molecules. Naturally, there is only a very narrow energy range for biological processes to happen in. That range has as its upper bound the atomic ionization energy which is of the order of one Ry, so around 10 eV. The lower bound for the

energy range on which biochemical processes can take place is given by the thermal energy on the surface of our planet, which is about $k_B T \approx 25\,\mathrm{meV}$. All processes happening at these low energies will be largely obscured by thermal noise. Therefore, the energy range of a few eV, well out of the noisy thermal background and still far from dangerous ionizing energies, is the range where bio-chemistry works. In other words, the visible range of electromagnetic radiation is the energy range of electronic transitions in matter where *life* happens. Not coincidentally it is the very same energy range where quantum physics impacts our daily lives in the form of technological devices: Artificial lighting is increasingly dominated by light emitting diodes and thereby relies on spontaneous emission. Furthermore, current and future optical data-storage and communication are based on optical read, write, and transfer processes at or close to visible frequencies. Understanding and controlling light-matter interaction is therefore of utmost technological interest. The interaction of light and matter includes the phenomena of emission and absorption, which are intimately related to each other. This thesis focuses on the control of spontaneous emission, which is a specific process of light generation. We therefore now give a brief introduction to spontaneous emission.

1.2 Spontaneous emission and the local density of optical states

With spontaneous emission we refer to the process of a quantum-mechanical system in an excited state undergoing a spontaneous transition to an energetically lower lying state under the emission of a photon. Consider a molecule as a quantum-mechanical system with a discrete energy level scheme. Furthermore, let the molecule be embedded in a host material that acts as a thermal bath but does not change the molecule's electronic level scheme [3]. For simplicity, we restrict our discussion to only two electronic states [4]. Vibrational excitations further broaden the electronic states into bands as sketched in the Jabłoński diagram in Fig. 1.1(a). Assume the molecule is initially in its ground state at a low level of thermal excitation, denoted as $|0\rangle$. After the absorption of a photon the system populates the both electronically and thermally excited state $|3\rangle$. Via the generation of lattice vibrations that are passed on to the embedding matrix the system relaxes to a state $|2\rangle$ close to the lower edge of the band of excited electronic states. The molecule now remains in state $|2\rangle$ until it decays to a state $|1\rangle$ in the band of electronic ground states, from which it can reach its initial state $|0\rangle$ by the emission of lattice vibrations. We are interested in the time the molecule remains in its excited state $|2\rangle$ before it relaxes under emission of a photon.* Since we are dealing with a quantum-mechanical system, there only is a certain probability per unit time that the system will decay. This probability per unit time is called the decay rate γ of the excited state $|2\rangle$.

*It is of course equally valid to ask for the time the molecule remains in its thermally excited state $|3\rangle$ before it decays to the state $|2\rangle$. It turns out that in practical systems thermal decay processes happen on time scales that are orders of magnitude faster than the radiative fluorescence process [4], a fact that will prove integral to our scheme of measuring the lifetime of state $|2\rangle$ outlined in Chapter 2.

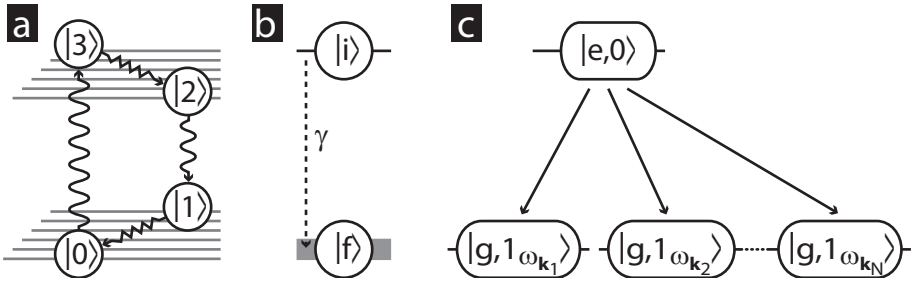

Figure 1.1: (a) Jabłoński diagram of a molecule. The two electronic states under consideration are both broadened into bands by vibrational excitations. Transitions involving a photon are indicated by the sinuous lines, while 'dark' transitions involving lattice vibrations are drawn jagged. (b) Quantum-mechanical system undergoing a transition from its initial state $|i\rangle$ to a set of final states $|f\rangle$. (c) Illustration of the transition from an initial state $|i\rangle = |e,0\rangle$ consisting of the emitter in its excited state and no photon, to a set of final states $|g,1_{\omega_{\boldsymbol{k}_i}}\rangle$ consisting of the emitter in its ground state and a photon (adopted from Reference [2]).

According to Fermi's Golden Rule the transition rate γ of a quantum-mechanical system from an initial state $|i\rangle$ to a set of final states $|f\rangle$ as sketched in Fig. 1.1(b) is

$$\gamma = \sum_f \frac{2\pi}{\hbar} \left|\langle f| \hat{\mathscr{H}} |i\rangle\right|^2 \delta(E_i - E_f). \tag{1.1}$$

The δ-function ensures that we only consider final states which are allowed by energy conservation and the interaction operator is in our case the Hamiltonian $\hat{\mathscr{H}} = -\hat{\boldsymbol{\mu}} \cdot \hat{\boldsymbol{E}}$ describing the electric dipole interaction, which couples the atom and the radiation field. It is most important to realize [5] that the states $|i\rangle$ and $|f\rangle$ are states of the complete emitter-radiation system [2]. Therefore, as illustrated in Fig. 1.1(c), the initial state $|i\rangle$ describes the excited emitter without a photon present, which we write as the state $|e,0\rangle$, where the first symbol denotes the electronic state of the atom and the second symbol the state of the radiation field.[†] Accordingly, we can denote the final state of the transition $|f\rangle$ as $|g,1_{\omega_{\boldsymbol{k}_i}}\rangle$, where the first symbol denotes the emitter in its ground state and the second symbol indicates that the electromagnetic mode of the embedding system described by its frequency ω and the wavevector $\boldsymbol{k}_i$ is now populated with one photon. Figure 1.1(c) illustrates that even though only a single electronic ground state is available the sum in Eq. (1.1) has to be carried out over all photon states $\boldsymbol{k}_i$ available at the transition frequency ω. For a continuum of final states, we can therefore rewrite Eq. (1.1) as [2, 5]

$$\gamma = \frac{\pi\omega}{3\hbar\epsilon_0} |\boldsymbol{\mu}|^2 \, \rho_\mu(\omega, \boldsymbol{r}), \tag{1.2}$$

[†]Since the electrons are much lighter than the atomic nuclei the electrons are considered to follow the vibrations of the molecule practically instantaneously. Under this assumption of adiabaticity, called the Born-Oppenheimer approximation, the molecule's wave-function can be separated into an electronic and a vibrational part [2].

where we introduced the transition dipole matrix element $\boldsymbol{\mu} = \langle g | \hat{\boldsymbol{\mu}} | e \rangle$ describing the atomic part of the transition. Furthermore, Eq. (1.2) contains the Local Density of Optical States $\rho_\mu(\omega, \boldsymbol{r})$, first recognized by Sprik *et al.* [5], which comprises a sum over all photon states at frequency ω available to an emitter with dipole orientation $\boldsymbol{\mu}$. Most importantly, the Local Density of Optical States (LDOS) depends on the position $\boldsymbol{r}$ of the emitter; it describes the density of photon states available at a certain position of the source. While the molecule's ground state $|g\rangle$ is intrinsic to the molecule, given by the atomic constituents and their interactions, the final state of the transition $|f\rangle$, or rather the density of final states of the radiation field, is a quantity that we can tune by changing the emitter's environment. Therefore, if we manage to create an environment with a large density of photon states at the emitter position and transition frequency, the excited emitter will decay faster than in an environment with very few photon states available, where the emitter just has no opportunity to get rid of the energy of the decay process. Going beyond the rate of the transition, by providing an environment with a large density of states with a desired $\boldsymbol{k}$ at the transition frequency ω we can increase the probability of emission into such a favorable state. Therefore, deliberate structuring of an emitter's environment allows to control both *when* light is emitted and *where* it is emitted *to*.

1.3 Spontaneous-emission control on the nanoscale

Historically, we trace the development of spontaneous-emission control on sub-wavelength scales back to two seminal works. The realization that the decay rate of a quantum-mechanical system depends on its photonic environment is attributed to Purcell [6], who suggested in 1946 to boost the transition rate of a nuclear magnetic moment at radio frequencies by coupling the emitter to a resonator of volume V and quality factor $Q = \omega/\Delta\omega$, resonant at the transition frequency. Purcell simply argued that the observed decay-rate enhancement should be the ratio of the density of states provided by the cavity and that of free space. Since in the cavity there is one mode per volume V and per Lorentzian frequency band $\Delta\omega$ and the density of states of free space is $\rho_{\text{vac}} = \frac{\omega^2}{\pi^2 c^3}$ [7] the famous Purcell factor describing the achievable spontaneous-emission rate enhancement by a cavity reads

$$F_p = \frac{3}{4\pi^2} \frac{Q}{V} \lambda^3. \tag{1.3}$$

The second historic milestone was set independently by Drexhage, who measured the spontaneous-emission rate of rare-earth ions as a function of their distance to a mirror at the end of the 1960s [8]. He found characteristic oscillations of the spontaneous-emission rate as a function of emitter-mirror distance and thereby established for the first time experimentally that the decay rate of a spontaneous emitter depends on the emitter's position with respect to its photonic environment. Nowadays, both Purcell's and Drexhage's work are well embedded in the framework of cavity quantum electrodynamics (cQED) in its weak-coupling limit [9, 10].

During the decades after Drexhage's work, spontaneous-emission control remained largely divided between two communities. On the one hand, physical chemists such as Chance, Prock and Silbey [11], and Lukosz and Kunz [12, 13], were dedicated to understand molecular fluorescence and molecular radiation patterns near dielectric interfaces. On the other hand, controlling spontaneous emission in cavities via the Purcell effect, initially with Rydberg atoms at microwave frequencies, was largely the realm of atomic physics. A hallmark experiment is the first enhancement of spontaneous emission of a single atom at GHz frequencies in 1983 by Goy *et al.* [14]. The inhibition of spontaneous emission was first observed on the peculiar model system of a single electron on a cyclotron orbit in 1985 by Gabrielse and Dehmelt [15], immediately followed by the first demonstration of inhibited spontaneous emission of a single Rydberg atom by Hulet *et al.* [16]. For completeness we cannot go without mentioning that while spontaneous-emission control originated from controlling the lifetime of an emitter, coupling to a cavity also shifts the emitter's emission frequency depending on its distance from the cavity walls [17, 18].

Continuing our brief historical account of cQED, we note that the route of the atomic-physics community was dominated by the pursuit of two main goals. The first goal was to move from microwave to optical frequencies. One of the reasons to move to higher photon energies is that optical modes are practically not thermally populated at ambient temperature. There is a further difference between microwave and optical cQED experiments. In microwave cQED the atoms are detected as they leave the cavity and serve as a probe of the evolution of the field in the resonator. The situation is reversed in the optical domain where the light field escaping the cavity tells the observer about the evolution of the atom inside the resonator [10]. The first microcavity at optical wavelengths was assembled by Martini *et al.* [19] from two plane mirrors with a solution of dye molecules in between, an experiment that can be regarded as the first direct meeting point of the developments started by Purcell and Drexhage independently.

The second and major goal that has driven cQED forward throughout the decades has been the desire for ever stronger coupling rates between the emitter and the field in the cavity. There exists a critical coupling strength beyond which the process of spontaneous emission becomes reversible and the atom reabsorbs its own photon that has not left the cavity yet. The process of the emitter cycling between its ground and excited state by exchanging a photon with the cavity is called vacuum Rabi oscillation [10] and is the fingerprint of the regime of 'strong coupling' in cQED [9]. In the regime of strong coupling the coupled atom-radiation system evolves coherently and the predictions of quantum mechanics can be tested and its promises harnessed. Even though cQED with atomic systems in the strong-coupling regime is still going strong we conclude our short history of cQED in atomic systems with mentioning the landmark experiment of Thompson *et al.* who observed the strong-coupling regime with single atoms at optical frequencies in 1992 [20]. For further reading about cQED in the weak-coupling and the strong-coupling regime we refer to the most enjoyable textbooks by Haroche and Raimond [10], and Dutra [9].

To appreciate the promise of nano-optics for spontaneous-emission control we

have to remember that the atomic-physics community had been considering a cavity as a 'box for light' [9, 10] in Purcell's spirit for most of the time. While such a conventional cavity with an atomic emitter provides an ideal model system to explore the interaction of light and matter at a most fundamental level, it has some intrinsic limitations. For instance, since the size of the cavity has to be at least half a wavelength there is a strict lower bound on the mode volume. Light-matter coupling strength can only be boosted further by increasing the quality factor of the cavity, which naturally means an extremely narrow band of operation. In general, it seemed that an impact of cQED on real-world devices outside a tightly-controlled laboratory environment would remain elusive. Three major game changers have brought spontaneous-emission control outside the realm of atomic physics and into the solid state. First, III-V materials have emerged as the material of choice to realize quantum devices in the weak-coupling and strong-coupling regime, due to their excellent electrical and optical addressability and spin-coherence properties [21]. Second, the proposal of the photonic bandgap by Yablonovitch [22] and John [23] in 1987 brought the possibility of spontaneous-emission control in the solid state to the fore. The community realized that cQED not only provides a playground to test our understanding of the oddities of quantum physics in the strong-coupling regime but already in the weak-coupling limit is powerful enough to turn solid-state light sources like LEDs and ultra-low-threshold lasers into mass-produced devices [24, 25] and boost the efficiency of solar cells [22]. The third major development is the advent of nanotechnology that offers the opportunity to structure matter and thereby the LDOS on length scales comparable to and even much smaller than optical wavelengths in many different material systems [26]. There exists an entire zoo of micro- and nanostructures that allow an amazing control of spontaneous emission. In the following, we will first give a short overview over dielectric structures and both their achievements and limitations regarding spontaneous-emission control. We are then prepared to turn our attention to plasmonic nanostructures, which are mainly in the focus of this thesis.

1.3.1 Dielectric micro- and nanostructures

Photonic crystals. Photonic crystals have become one of the major devices for controlling spontaneous emission in condensed-matter systems [32]. Photonic crystals are periodic arrangements of dielectric scatterers for light, in full analogy to the crystal lattice forming a periodic scattering potential for electrons [33]. A scanning-electron micrograph (SEM) of a three-dimensional photonic crystal is shown in Fig. 1.2(a). At the edge of a silicon wafer arrays of holes have been drilled in orthogonal directions to create the periodic scattering potential for light [27, 28]. Photonic crystals have found wide use in the context of spontaneous-emission control [32]. Due to interference of the fields scattered by the periodic structure energy bandgaps form, corresponding to frequencies which cannot propagate inside the photonic crystal since their fields destructively interfere. Therefore, the decay of a spontaneous emitter located inside a photonic crystal with a transition energy falling into the bandgap of the surrounding structure will be inhibited while a decay-rate enhancement is expected close to the

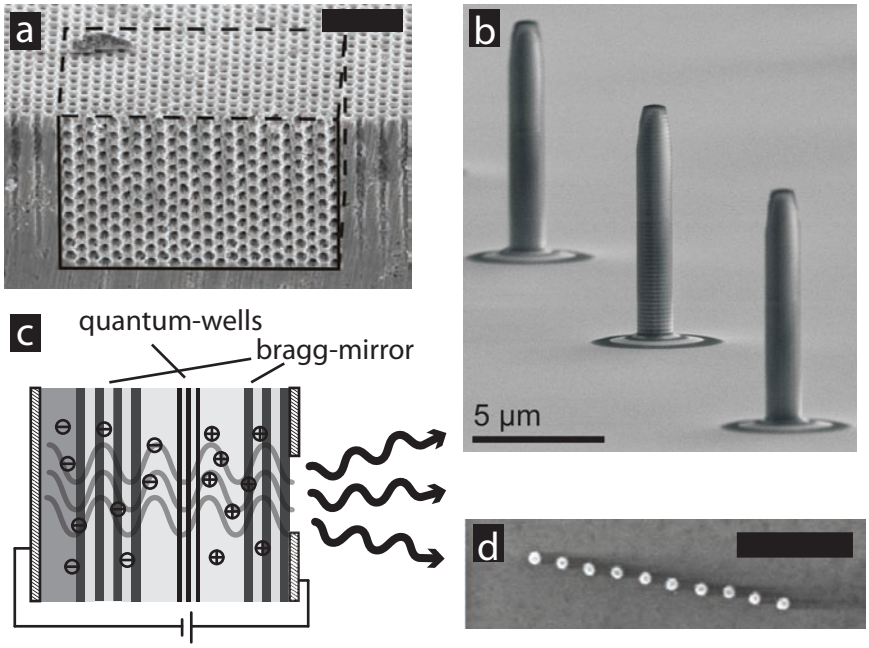

Figure 1.2: (a) 3D photonic-bandgap crystal fabricated in silicon by drilling two perpendicularly oriented arrays of holes into a wafer. Scalebar denotes 4 µm (fabricated by the Complex Photonic Systems group at the University of Twente in collaboration with groups in Dutch industry (ASML, TNO, Philips), see References [27, 28]). (b) Micropillar cavities confining an optical mode in three dimensions by Bragg mirrors in the vertical direction and the pillar-shape in the radial direction (image courtesy of Monika Emmerling, Adriana Wolf, and Prof. Stephan Reitzenstein, Department of Applied Physics at the University of Würzburg. See References [29, 30]). (c) Schematic of VCSEL. The structure consists of epitaxially grown multi-layers sandwiched between Ohmic contacts. Two oppositely doped Bragg mirrors confine the lasing mode to the region of the quantum wells, where carriers are confined and effectively recombine (adopted from Reference [25]). (d) SEM micrograph of silver nanoparticles arranged in a chain. These plasmonic nanoparticles strongly scatter light and can be used to confine propagating radiation (scalebar denotes 500 nm, image courtesy of René de Waele, see Reference [31]).

band edge. Suppression and enhancement in three-dimensional photonic crystals has been observed across a bandwidth of $\frac{\Delta\omega}{\omega} \approx 10\%$ of the optical emission wavelength by Lodahl *et al.* [34]. Recent fabrication advances produced 3D photonic crystals in which decay rates of emitters close to and within the photonic bandgap differ by an order of magnitude [35]. While the fabrication of three-dimensional photonic crystals is a challenge on its own [36, 37], the available mature planar processing techniques have produced two-dimensional photonic crystals of superior quality. Dramatic suppression of spontaneous emission by almost two orders of magnitude has been reported in 2D

photonic crystals [38]. Since for frequencies within the photonic bandgap a photonic crystal acts as a mirror, a cavity can be formed by surrounding a region with a photonic crystal or, in other words, creating a defect within the crystal [32, 39]. Photonic crystals rely on Bragg scattering, so the fields and therefore also the LDOS vary on length scales of $\lambda/2$. Therefore, photonic-crystal cavities, just like conventional mirror bounded cavities, can be reduced to approximately λ^3 in volume and Q-factors of the order of 10^4 have been achieved [39]. When a spontaneous emitter, like a quantum dot, is incorporated into such a defect its spontaneous-emission rate can be strongly enhanced [32]. The enhancement of the fraction of photons emitted into the cavity mode, called β-factor, was used to construct a photonic-crystal-cavity laser already in 1999 by Painter *et al.* [40]. Cavities in two-dimensional photonic crystals with embedded emitters are sturdy and small devices in which cQED can be studied in the solid state even in the regime of strong coupling [41].

Other dielectric photonic structures. Besides photonic crystals there exists a plethora of other dielectric structures to tailor light-matter interaction. We use their dimensionality to roughly order the presented systems. Zero-dimensional micropillar cavities are conceptually closely related to photonic-crystal cavities [42]. While 2D photonic-crystal cavities use Bragg reflection for confinement in two dimensions and total internal reflection in the third, micropillar cavities reverse the roles of the employed confinement mechanisms and confine radiation between two Bragg mirrors in a pillar [43]. A SEM micrograph of micropillar resonators fabricated in III-V semiconductor material is shown in Fig. 1.2(b). Epitaxial techniques allow layer-by-layer growth with atomic precision to yield Bragg mirrors of superior quality. The pillars are etched out of the stratified substrate in a second processing step [29]. Micropillar cavities have been used to enhance the rate of spontaneous emission by a factor of five in the first demonstration by Gérard *et al.* [43] and soon reached the regime of strong coupling [29]. Zero-dimensional confinement can furthermore be achieved in dielectric microspheres and microtoroids that can be relatively easily fabricated with such extraordinary quality that Q-factors in excess of 10^6 are considered to be routine [39]. Such whispering-gallery-mode systems have been used to tailor spontaneous emission of fluorescing dye molecules [44] and to construct microlasers [45].

Moving on from 0-D structures, confinement of optical modes in one dimension is technologically crucial for optical communication [46]. Next-generation optical data-transfer and data-processing systems require single-photon sources efficiently interfaced with optical waveguides [47]. Therefore, the direct coupling of quantum emitters to dielectric waveguides is currently heavily investigated [48] and β-factors in excess of 85% have been reported to date [49]. A strongly directional and highly efficient single-photon source can be engineered by coupling a quantum emitter to a cleverly terminated 1D-waveguide with a tightly confined mode [50]. Furthermore, employing an elliptically shaped truncated 1D-waveguide such a microscopic ‘photon gun’ can control the polarization of spontaneous emission to a degree of 95% [51].

Increasing dimensionality further, layered 2D media do not provide emission rate

enhancements beyond factors of about two as a consequence of the poor confinement of photonic modes. However, stratified media are potentially useful in microscopy applications, as they allow to create inexpensive substrates that control collection efficiency. A simple stack of only a few stratified layers of dielectric materials was shown to yield near-unity collection efficiency for emission of a single oriented molecular source by Lee *et al.* [52]. Technologically, layered photonic structures currently have the largest impact on our daily lives. In vertical-cavity surface-emitting lasers (VCSELs), multi-layers with high reflectivity form cavities that enable low-threshold lasing by designs directly inspired by cQED and put to work in mass produced devices [25, 53]. A schematic of a typical VCSEL design is drawn in Fig. 1.2(c). Epitaxially grown semiconductor multilayers form Bragg mirrors to define an optical mode within the device. One of the mirrors is made from p-doped material, the other one from n-doped material. Thereby, carriers injected via Ohmic contacts can be transported to the quantum wells in the center of the device, where they recombine under photon emission into the cavity mode. Closely related are resonant-cavity LEDs which harness the Purcell effect to boost extraction efficiencies from notoriously high-index semiconductor devices, a design that has turned LEDs into light sources of record-high efficiencies [54].

Finally, we note that 'perfect order' as a design criterion is not required. Another class of dielectric photonic structures are disordered materials, which are essentially random assemblies of high-index grains. The LDOS within three-dimensional random-scattering materials exhibits drastic variations, which have been observed by embedding fluorescing sources and measuring the Purcell effect [55]. Decay-rate enhancements up to a factor of eight have been demonstrated in strongly scattering samples [56]. Random-scattering materials with embedded sources can furthermore exhibit gain [57] and random lasing [58]. Random scattering in two dimensions, created by deliberately disordering a 2D photonic crystal, has been used to enhance the spontaneous-emission rate of a single-photon source by a factor of 15 [59] and funnel 95% of the emitted photons into the chosen optical mode.

1.3.2 Metallic nanostructures

In dielectric structures electric fields and therefore also the LDOS always vary on length scales comparable to the wavelength in the medium. Metallic nanostructures, in stark contrast, can confine fields to sizes well below the wavelength. A typical plasmonic nanostructure is depicted in Fig. 1.2(d). The SEM micrograph shows a chain of plasmonic nanoparticles, each with a diameter of 50 nm, that have been used to controllably transport and focus light [31]. The initial milestone on the way to truly sub-wavelength optics was set by Ebbesen *et al.* with their work on the transmission of light through arrays of sub-wavelength sized holes in metal films [60], which initiated the field of plasmonics [44, 61–63]. In metallic structures the free-electron gas strongly interacts with the light field giving rise to polaritonic charge-density waves termed plasmon polaritons [2]. John gives a strikingly simple argument why metals interact so strongly with light [64]: The classical wave equation can be brought into a form

resembling the time-independent Schrödinger equation

$$-\nabla^2 \boldsymbol{E} + \nabla(\nabla \cdot \boldsymbol{E}) - \frac{\omega^2}{c^2}\epsilon_{\text{fluct}}(\boldsymbol{r})\boldsymbol{E} = \epsilon_0 \frac{\omega^2}{c^2}\boldsymbol{E}.$$

The 'potential' is given by the dielectric contrast $-\epsilon_{\text{fluct}}(\boldsymbol{r})\frac{\omega^2}{c^2}$ and the average dielectric constant $\epsilon_0 \frac{\omega^2}{c^2}$ plays the role of the energy eigenvalue, where both potential and eigenvalue are scaled with the square of the wavenumber. Clearly, bound states only exist for negative ϵ_{fluct} whereas photon states in dielectric structures are always propagating, i.e., have energy above the potential. Localization in dielectric structures hence always requires interference [64].[‡] The large (negative) epsilon of metals furthermore gives rise to surface plasmon polaritons, charge-density oscillations at a metal-dielectric interface, with a wavelength significantly shorter than the free-space photon wavelength in order to satisfy the boundary conditions at the interface [2]. In turn, the fact that the plasmon wavelengths can be much smaller than λ means that large Purcell factors can be achieved without requiring high quality factors at all. Indeed, one enormous strength of plasmonic resonators is their strong interaction with optical fields in extremely small volumes with modest to low quality factors on the order of ten, which makes them extraordinarily broad-band [65] and ideally suited to control spontaneous emission of ubiquitous broad-band emitters like dye molecules and semiconductor nanocrystals [66].

Interestingly, plasmonics currently unites the field of quantum optics with single-photon sources with the field of single-molecule microscopy and manipulation, which we encounter in detail in Chapter 2. This joining of fields is especially evident in a set of landmark experiments that strongly motivates the work reported in this thesis. The main question we target is how we can control how fast and where to a photon is emitted simply by placing the excited source judiciously inside a plasmonic nanostructure. A ground-breaking achievement in spontaneous-emission control with plasmonic nanostructures was the controlled coupling of a single quantum emitter to an optical antenna on a scanning probe by Farahani *et al.* [67], Kühn *et al.* [68] and Anger *et al.* [69]. The large gain achievable with plasmon antennas is evident from the decay-rate enhancement by a factor of 20 observed together with an equal enhancement in brightness by Kühn *et al*. Most importantly, these achievements relied on the precise positioning of the emitter with respect to the nanophotonic structure to within about $\lambda/10$.

1.4 Motivation and overview over this thesis

As shown in the previous section, structuring and engineering of the LDOS on a sub-wavelength scale offers a plethora of opportunities to tailor light-matter interaction. The first observations of the controlled coupling of a spontaneous emitter to a truly

[‡] Also in photonic crystals light propagation is halted by dielectric media due to the *periodicity* of the structure.

nano-optical structure [67–69] affirm the notion that a precise spatial positioning of the emitter with respect to the nanostructure is indispensable in order to harness the promise of plasmonics. The results furthermore raise the question if drastically different emission properties can be achieved simply by changing the position of the emitter, possibly by only a sub-wavelength distance, with respect to a nanophotonic structure. Therefore, this thesis targets the question how the rate and directionality of spontaneous emission can be controlled by positioning an emitter with respect to its photonic environment.

In order to address this question we have developed an experimental setup that is able to map the LDOS of any planar sample. Chapter 2 introduces the techniques of single-molecule spectroscopy and scanning-probe microscopy and details our experimental apparatus. Our strategy to map the LDOS relies on a combination of fluorescence-lifetime imaging and scanning-probe microscopy. We attach a fluorescent source to a scanning probe and move it with sub-wavelength precision over a sample while continuously monitoring the decay rate.

A first demonstration of the developed technique is presented in Chapter 3 where we map the LDOS of a noble-metal nanowire. By judiciously positioning the fluorescent source with respect to the wire we demonstrate both repeatable and reversible temporal control over spontaneous emission and furthermore funnel a significant fraction of the emitted light into a guided plasmonic excitation of the wire.

A significant part of this thesis is concerned with the theoretical modeling of nanophotonic systems. Therefore, Chapter 4 gives an overview over the theoretical framework that was applied in the subsequent Chapters. We review the coupled-dipole model and emphasize its application in the context of nanoplasmonics and spontaneous-emission control. We put special emphasis on the radiative damping experienced by any strongly scattering system to prepare the ground for the subsequent Chapters.

In Chapter 5 we investigate the LDOS in the vicinity of plasmonic meta-molecules. We use a focused electron beam as a localized source to spatially map the LDOS. Our experiments reveal a peculiar spatial redistribution of the LDOS with frequency. Our theoretical treatment exploits the symmetry of the plasmonic meta-molecules to unveil the intimate relation between scattering and the LDOS.

With the insight gained on systems of coupled strong scatterers we turn our attention to their behavior in hybrid photonic systems. In Chapter 6 we theoretically pursue the idea of a spontaneous emitter coupled to an optical antenna immersed in a much larger background system. While the nano-antenna modifies the LDOS on a length scale drastically smaller than the wavelength we consider background systems that modulate the LDOS on a wavelength scale. Our analysis identifies the scattering strength of the antenna to govern a truly counter-intuitive behavior. Surprisingly, an enhanced LDOS offered by the background system spoils the enhancement provided by a strongly scattering antenna.

Finally, in Chapter 7, we put our predictions from the previous Chapter to the test in the laboratory. To this end we couple dye molecules to strongly scattering optical-antennas. We return to the roots of our field by performing a Drexhage experiment with such a ‘superemitter’ to indeed find the predicted counter-intuitive behavior.

References

[1] J. D. Jackson, *Classical Electrodynamics*, Wiley, New York, 1999.

[2] L. Novotny and B. Hecht, *Principles of Nano-Optics*, Cambridge University Press, Cambridge, 2006.

[3] J. R. Lakowicz, *Principles of Fluorescence Spectroscopy*, Springer Berlin / Heidelberg, 2006.

[4] O. Svelto, *Principles of Lasers*, Springer, 2009.

[5] R. Sprik, B. A. van Tiggelen, and A. Lagendijk, *Optical emission in periodic dielectrics*, Europhys. Lett. **35**, 265 (1996).

[6] E. M. Purcell, *Spontaneous emission probabilities at radio frequencies*, Phys. Rev. **69**, 681 (1946).

[7] J.-M. Gérard and B. Gayral, *Strong Purcell effect for InAs quantum boxes in three-dimensional solid-state microcavities*, J. Lightwave Technol. **17**, 2089 (1999).

[8] K. H. Drexhage, *Influence of a dielectric interface on fluorescence decay time*, J. Lumin. **1-2**, 693 (1970).

[9] S. Dutra, *Cavity Quantum Electrodynamics: The Strange Theory Of Light In A Box*, Wiley Series in Lasers and Applications, J. Wiley, 2005.

[10] S. Haroche and J. Raimond, *Exploring the Quantum: Atoms, Cavities, And Photons*, Oxford graduate texts in mathematics, Oxford University Press, 2006.

[11] R. R. Chance, A. Prock, and R. Silbey, *Molecular Fluorescence and Energy Transfer Near Interfaces*, pages 1–65, John Wiley & Sons, Inc., 2007.

[12] W. Lukosz and R. E. Kunz, *Light emission by magnetic and electric dipoles close to a plane interface. I. Total radiated power*, J. Opt. Soc. Am. **67**, 1607 (1977).

[13] W. Lukosz and R. E. Kunz, *Light emission by magnetic and electric dipoles close to a plane dielectric interface. II. Radiation patterns of perpendicular oriented dipoles*, J. Opt. Soc. Am. **67**, 1615 (1977).

[14] P. Goy, J. M. Raimond, M. Gross, and S. Haroche, *Observation of cavity-enhanced single-atom spontaneous emission*, Phys. Rev. Lett. **50**, 1903 (1983).

[15] G. Gabrielse and H. Dehmelt, *Observation of inhibited spontaneous emission*, Phys. Rev. Lett. **55**, 67 (1985).

[16] R. G. Hulet, E. S. Hilfer, and D. Kleppner, *Inhibited spontaneous emission by a Rydberg atom*, Phys. Rev. Lett. **55**, 2137 (1985).

[17] D. J. Heinzen and M. S. Feld, *Vacuum radiative level shift and spontaneous-emission linewidth of an atom in an optical resonator*, Phys. Rev. Lett. **59**, 2623 (1987).

[18] V. Sandoghdar, C. I. Sukenik, E. A. Hinds, and S. Haroche, *Direct measurement of the van der Waals interaction between an atom and its images in a micron-sized cavity*, Phys. Rev. Lett. **68**, 3432 (1992).

[19] F. D. Martini, G. Innocenti, G. R. Jacobovitz, and P. Mataloni, *Anomalous spontaneous emission time in a microscopic optical cavity*, Phys. Rev. Lett. **59**, 2955 (1987).

[20] R. J. Thompson, G. Rempe, and H. J. Kimble, *Observation of normal-mode splitting for an atom in an optical cavity*, Phys. Rev. Lett. **68**, 1132 (1992).

[21] C. Klingshirn, *Semiconductor Optics*, Advanced texts in physics, Springer, 2006.

[22] E. Yablonovitch, *Inhibited spontaneous emission in solid-state physics and electronics*, Phys. Rev. Lett. **58**, 2059 (1987).

[23] S. John, *Strong localization of photons in certain disordered dielectric superlattices*, Phys. Rev. Lett. **58**, 2486 (1987).

[24] Y. Yamamoto and R. E. Slusher, *Optical processes in microcavities*, Phys. Today **46**, 66 (1993).

[25] P. L. Gourley, *Microstructured semiconductor lasers for high-speed information processing*, Nature **371**, 571 (1994).

[26] M. Wilson, *Nanotechnology: Basic Science and Emerging Technologies*, Chapman & Hall/CRC, 2002.

[27] R. W. Tjerkstra, L. A. Woldering, J. M. van den Broek, F. Roozeboom, I. D. Setija, and W. L. Vos, *Method to pattern etch masks in two inclined planes for three-dimensional nano- and microfabrication*, J. Vac. Sci. Technol. B **29**, 061604 (2011).

[28] J. M. van den Broek, L. A. Woldering, R. W. Tjerkstra, F. B. Segerink, I. D. Setija, and W. L. Vos, *Inverse-woodpile photonic band gap crystals with a cubic diamond-like structure made from single-crystalline silicon*, Adv. Funct. Mater. **22**, 25 (2012).

[29] J. Reithmaier, G. Sek, A. Löffler, C. Hofmann, S. Kuhn, S. Reitzenstein, L. Keldysh, V. Kulakovskii, T. Reinecke, and A. Forchel, *Strong coupling in a single quantum dot-semiconductor microcavity system*, Nature **432**, 197 (2004).

[30] S. Ates, S. M. Ulrich, A. Ulhaq, S. Reitzenstein, A. Löffler, S. Höfling, A. Forchel, and P. Michler, *Non-resonant dot-cavity coupling and its potential for resonant single-quantum-dot spectroscopy*, Nature Photon. **3**, 724 (2009).

[31] R. de Waele, A. F. Koenderink, and A. Polman, *Tunable nanoscale localization of energy on plasmon particle arrays*, Nano Lett. **7**, 2004 (2007).

[32] S. Noda, M. Fujita, and T. Asano, *Spontaneous-emission control by photonic crystals and nanocavities*, Nature Photon. **1**, 449 (2007).

[33] J. D. Joannopoulos, P. R. Villeneuve, and S. Fan, *Photonic crystals: putting a new twist on light*, Nature **386**, 143 (1997).

[34] P. Lodahl, A. F. van Driel, I. S. Nikolaev, A. Irman, K. Overgaag, D. Vanmaekelbergh, and W. L. Vos, *Controlling the dynamics of spontaneous emission from quantum dots by photonic crystals*, Nature **430**, 654 (2004).

[35] M. R. Jorgensen, J. W. Galusha, and M. H. Bartl, *Strongly modified spontaneous emission rates in diamond-structured photonic crystals*, Phys. Rev. Lett. **107**, 143902 (2011).

[36] J. E. G. J. Wijnhoven and W. L. Vos, *Preparation of photonic crystals made of air spheres in titania*, Science **281**, 802 (1998).

[37] K. Aoki, D. Guimard, M. Nishioka, M. Nomura, S. Iwamoto, and Y. Arakawa, *Coupling of quantum-dot light emission with a three-dimensional photonic-crystal nanocavity*, Nature Photon. **2**, 688 (2008).

[38] Q. Wang, S. Stobbe, and P. Lodahl, *Mapping the local density of optical states of a photonic crystal with single quantum dots*, Phys. Rev. Lett. **107**, 167404 (2011).

[39] K. J. Vahala, *Optical microcavities*, Nature **424**, 839 (2003).
[40] O. Painter, R. K. Lee, A. Scherer, A. Yariv, J. D. O'Brien, P. D. Dapkus, and I. Kim, *Two-dimensional photonic band-gap defect mode laser*, Science **284**, 1819 (1999).
[41] T. Yoshie, A. Scherer, J. Hendrickson, G. Khitrova, H. M. Gibbs, G. Rupper, C. Ell, O. B. Shchekin, and D. G. Deppe, *Vacuum Rabi splitting with a single quantum dot in a photonic crystal nanocavity*, Nature **432**, 200 (2004).
[42] K. Vahala, editor, *Optical Microcavities (Advanced Series in Applied Physics, Vol. 5)*, World Scientific, Singapore, 2005.
[43] J. M. Gérard, B. Sermage, B. Gayral, B. Legrand, E. Costard, and V. Thierry-Mieg, *Enhanced spontaneous emission by quantum boxes in a monolithic optical microcavity*, Phys. Rev. Lett. **81**, 1110 (1998).
[44] M. D. Barnes, C.-Y. Kung, W. B. Whitten, J. M. Ramsey, S. Arnold, and S. Holler, *Fluorescence of oriented molecules in a microcavity*, Phys. Rev. Lett. **76**, 3931 (1996).
[45] V. Sandoghdar, F. Treussart, J. Hare, V. Lefèvre-Seguin, J. M. Raimond, and S. Haroche, *Very low threshold whispering-gallery-mode microsphere laser*, Phys. Rev. A **54**, R1777 (1996).
[46] G. Agrawal, *Fiber-optic communication systems*, Wiley series in microwave and optical engineering, Wiley-Interscience, 2002.
[47] C. Santori, D. Fattal, and Y. Yamamoto, *Single-Photon Devices and Applications*, Physics Textbook, John Wiley & Sons, 2010.
[48] M. Fujiwara, K. Toubaru, T. Noda, H.-Q. Zhao, and S. Takeuchi, *Highly efficient coupling of photons from nanoemitters into single-mode optical fibers*, Nano Lett. **11**, 4362 (2011).
[49] A. Laucht, S. Pütz, T. Günthner, N. Hauke, R. Saive, S. Frédérick, M. Bichler, M.-C. Amann, A. W. Holleitner, M. Kaniber, and J. J. Finley, *A waveguide-coupled on-chip single-photon source*, Phys. Rev. X **2**, 011014 (2012).
[50] J. Claudon, J. Bleuse, N. S. Malik, M. Bazin, P. Jaffrennou, N. Gregersen, C. Sauvan, P. Lalanne, and J.-M. Gérard, *A highly efficient single-photon source based on a quantum dot in a photonic nanowire*, Nature Photon. **4**, 174 (2010).
[51] M. Munsch, J. Claudon, J. Bleuse, N. S. Malik, E. Dupuy, J.-M. Gérard, Y. Chen, N. Gregersen, and J. Mørk, *Linearly polarized, single-mode spontaneous emission in a photonic nanowire*, Phys. Rev. Lett. **108**, 077405 (2012).
[52] K. G. Lee, X. Chen, H. Eghlidi, P. Kukura, R. Lettow, A. Renn, V. Sandoghdar, and S. Götzinger, *A planar dielectric antenna for directional single-photon emission and near-unity collection efficiency*, Nature Photon. **5**, 166 (2011).
[53] K. Iga, *Surface-emitting laser — its birth and generation of new optoelectronics field*, IEEE J. Sel. Topics Quantum Electron. **6**, 1201 (2000).
[54] D. Delbeke, R. Bockstaele, P. Bienstman, R. Baets, and H. Benisty, *High-efficiency semiconductor resonant-cavity light-emitting diodes: a review*, IEEE J. Sel. Topics Quantum Electron. **8**, 189 (2002).
[55] M. D. Birowosuto, S. E. Skipetrov, W. L. Vos, and A. P. Mosk, *Observation of spatial fluctuations of the local density of states in random photonic media*, Phys. Rev. Lett. **105**, 013904 (2010).
[56] R. Sapienza, P. Bondareff, R. Pierrat, B. Habert, R. Carminati, and N. F. van Hulst, *Long-tail statistics of the Purcell factor in disordered media driven by near-field interactions*, Phys. Rev. Lett. **106**, 163902 (2011).
[57] R. G. S. El-Dardiry, *Sources and Gain in Photonic Random Media*, PhD thesis, University of Amsterdam, 2012.
[58] D. S. Wiersma, *The physics and applications of random lasers*, Nature Phys. **4**, 359 (2008).

[59] L. Sapienza, H. Thyrrestrup, S. Stobbe, P. D. Garcia, S. Smolka, and P. Lodahl, *Cavity quantum electrodynamics with Anderson-localized modes*, Science **327**, 1352 (2010).

[60] T. W. Ebbesen, H. J. Lezec, H. F. Ghaemi, T. Thio, and P. A. Wolff, *Extraordinary optical transmission through sub-wavelength hole arrays*, Nature **391**, 667 (1998).

[61] E. Ozbay, *Plasmonics: Merging photonics and electronics at nanoscale dimensions*, Science **311**, 189 (2006).

[62] D. K. Gramotnev and S. I. Bozhevolnyi, *Plasmonics beyond the diffraction limit*, Nature Photon. **4**, 83 (2010).

[63] J. A. Schuller, E. S. Barnard, W. Cai, Y. C. Jun, J. S. White, and M. L. Brongersma, *Plasmonics for extreme light concentration and manipulation*, Nature Mater. **9**, 193 (2010).

[64] S. John, *Localization of light*, Phys. Today **May**, 32 (1991).

[65] A. F. Koenderink, *On the use of Purcell factors for plasmon antennas*, Opt. Lett. **35**, 4208 (2010).

[66] U. Resch-Genger, M. Grabolle, S. Cavaliere-Jaricot, R. Nitschke, and T. Nann, *Quantum dots versus organic dyes as fluorescent labels*, Nat. Methods **5**, 763 (2008).

[67] J. N. Farahani, D. W. Pohl, H.-J. Eisler, and B. Hecht, *Single quantum dot coupled to a scanning optical antenna: A tunable superemitter*, Phys. Rev. Lett. **95**, 017402 (2005).

[68] S. Kühn, U. Håkanson, L. Rogobete, and V. Sandoghdar, *Enhancement of single-molecule fluorescence using a gold nanoparticle as an optical nanoantenna*, Phys. Rev. Lett. **97**, 017402 (2006).

[69] P. Anger, P. Bharadwaj, and L. Novotny, *Enhancement and quenching of single-molecule fluorescence*, Phys. Rev. Lett. **96**, 113002 (2006).

2

Experimental Setup and Techniques

This Chapter describes the technical aspects of the scanning-emitter fluorescence-lifetime imaging microscope that was developed for this thesis. Our experimental setup, which is the combination of a conventional fluorescence-lifetime imaging microscope and a scanning near-field microscope, is detailed regarding the choice of individual components and their assembly. At hand of our own measurements we illustrate the employed techniques while at the same time benchmarking the performance of our setup. Furthermore, we give an overview of the achievements of the community towards a fluorescent scanning LDOS probe thus far and review promising fluorescing sources for our purpose. This Chapter is therefore intended both as a review of our field and a technical reference for the remainder of this thesis.

2.1 Fluorescing molecules as local probes

This thesis is devoted to studying the Local Density of Optical States (LDOS) in nanophotonic systems. These systems have characteristic dimensions smaller than the wavelength of light and they modulate the LDOS on sub-wavelength scales [1]. The decay rate of a spontaneous emitter is an unambiguous measure for the LDOS at the source position [2]. Since we want to measure the LDOS in complex solid-state photonic systems we require a source of spontaneous emission that can be embedded in a solid host material while retaining its internal structure. Fluorescent dye molecules have been proven to be ideal for this purpose [3]. Already the very first reports on the

optical detection of single molecules [4] recognize the potential of a single molecule as "a truly local probe addressable by the macroscopic light field" [5]. During the last two decades the field of single-molecule fluorescence spectroscopy [6] has developed at an enormous pace [7], making it a mature technology [8] and an indispensable tool for a variety of disciplines as diverse as the life-sciences [9] all the way to most fundamental quantum optics [10]. Thanks to the development of a variety of suitable excitation light sources and single-photon detectors [11] spectroscopy and lifetime measurements of few or single molecules at ambient conditions have become routine [12].

For our goal of studying the LDOS on sub-wavelength scales conventional diffraction-limited imaging is insufficient [13, 14]. The diffraction limit in optical imaging has first been broken with scanning-aperture techniques [15], which were soon applied to localize and characterize the orientation of single fluorescent molecules [16]. Arguably the first observation of the impact of the LDOS on the decay rate of a single molecule stems from the interrogation of fluorescing molecules under illumination by a scanning probe [17]. Since then, scanning probes have been employed to redirect emission of single emitters [18] and control their polarization [19, 20]. Brightness [21] and decay rate of single emitters were enhanced by approaching sub-wavelength scatterers attached to [22] or moved by pushing with a scanning probe [23]. Naturally, the next challenge has been to reverse the system and illuminate the sample with a sub-wavelength sized fluorescent source attached to a scanning probe [24–28]. In fact, the dream of interrogating a sample with a truly point-like scannable light source [29, 30] has been pursued since the advent of the near-field microscope [15].

Mapping the LDOS of a planar sample by measuring the lifetime of a fluorescent source attached to a scanning probe as it is scanned across the sample surface is an outstanding challenge and the overall goal to reach with the setup developed for this thesis. Since the LDOS is a local quantity [2], three requirements have to be met in order to map it spatially with a source attached to a scanning probe [31]: First, we require a source of spontaneous emission that is confined to a volume smaller than the length scale on which the LDOS varies in the system under study. Second, we need to move the LDOS probe relative to the sample with a precision better than the length scale of LDOS variation. Finally, we need to measure the source's decay rate while it is located where the LDOS is to be measured. These three requirements set the boundary conditions for our experimental setup. This Chapter introduces the building blocks that were combined to map the LDOS of planar samples on a sub-wavelength scale. Despite the fact that fluorescence-lifetime imaging and scanning-probe microscopy are both standard techniques we discuss them in great detail as a service to the uninitiated readers. At the same time, we illustrate the techniques at hand of measurements taken with our own setup. These measurements thereby serve as a benchmark and a reference for the later Chapters to make our experimental procedures fully transparent.

In Section 2.2 we introduce the technique of fluorescence-lifetime imaging microscopy to then detail our experimental apparatus and data-analysis technique. We discuss sources of spontaneous emission in Section 2.3 with special emphasis on their suitability to measure LDOS, and then turn to the scanning-probe part of our setup in Section 2.4.

2.2 Fluorescence-lifetime imaging

Fluorescence-lifetime imaging microscopy (FLIM) forms a spatial image of a sample where instead of intensity the lifetimes of the emitting sources in the specimen are mapped [14]. The method of choice to measure lifetimes in the ns range of few to single emitters is Time-Correlated Single-Photon Counting (TCSPC) [12]. As the acronym implies, even when performed on an ensemble of emitters, TCSPC relies on the precise detection of the arrival time of single photons. Practically all modern methods of FLIM combine TCSPC with confocal fluorescence microscopy [32] in order to gain both temporal and spatial resolution. This Section describes our confocal FLIM setup. We follow the light path through the system, sketched in Fig. 2.1, starting from the excitation source, continuing with the confocal imaging system to finally reach the detectors for the emitted fluorescence.

2.2.1 Excitation light source

Measuring fluorescence lifetimes using TCSPC relies on the precise measurement of the time elapsed between excitation of a fluorescent system and detection of the subsequently emitted photon [12]. Accordingly, the excitation light source must emit light pulses much shorter than the lifetime of the emitter under study. At the same time the repetition time of the excitation source should be significantly longer than the lifetime of the emitter to make sure that the fluorophore has decayed before the arrival of the subsequent pump pulse.

Light sources with duty cycles and repetition rates suitable for fluorescence-lifetime measurements have become readily available since the development of mode-locked lasers [33] which are currently increasingly replaced by cheaper laser diodes [34]. The source employed for all lifetime measurements in this thesis is a mode-locked diode-pumped Nd:YVO_4 laser manufactured by Time-Bandwidth Products with a repetition rate of 10 MHz emitting at 1064 nm. The laser output is frequency doubled by focusing through a non-linear KTP-crystal. The infrared component is then transmitted by a dielectric mirror and safely dumped while the 532 nm second-harmonic component is used to pump the emitters. We furthermore use a short-pass filter (D535/50x, Chroma Technology) to exclude any remaining IR-signal in the pump beam. In the green, the pulse duration is about 10 ps at a time-averaged power of about 30 mW. Our laser source is ideally suited to excite a broad range of readily available fluorescent dyes with lifetimes typically around 1 to 10 ns as well as semiconductor quantum dots with lifetimes typically around tens of ns. In the sketch of our setup in Fig. 2.1 we have left out the frequency-doubling components and the sketched laser beam is therefore only the 532 nm component entering the experiment. We can either send the collimated laser beam into the back-aperture of the used microscope objective to obtain a diffraction-limited laser spot in the focal plane of the objective. Alternatively, the movable epi-lens can be flipped into the beam path to focus the laser into the back-focal plane of the objective which ideally leads to a collimated beam illuminating the sample. In practise, we obtain an illuminated area of about 20 µm in diameter.

2.2.2 Confocal fluorescence microscope

Our setup is based on an inverted microscope (Ti-2000, Nikon) and is sketched in Fig. 2.1. For quick and easy inspection the sample can be illuminated in wide-field mode by a thermal white-light source (WL in Fig. 2.1) via a beam-splitter (BS). The light reflected and scattered by the sample is collected with the same objective, passes the beam-splitter and with the rotatable mirror (M1) the image created by the tube-lens is focused on the CCD camera (DS-Qi1Mc, Nikon). Our camera uses a thermoelectrically cooled Sony ICX285 CCD chip that provides up to 65% quantum efficiency around 500 nm and above 30% up to 725 nm at low read-out and dark noise. The magnification of the microscope is given by the ratio of the focal lengths of the objective and of the tube-lens ($f_{\mathrm{TL}} = 200\,\mathrm{mm}$). The tube-lens is fixed inside the microscope body and the magnification is chosen via the used objective.

In fluorescence microscopy, instead of using the scattered illumination light to form an image of a sample, one uses the fluorescent light emitted by the specimen [7] upon laser excitation. Since the typical absorption cross-section of a fluorophore is around $\sigma_{\mathrm{abs}} \approx 10^{-20}\,\mathrm{m}^2$ even in a diffraction-limited spot about 10^8 pump photons are necessary to excite the emitter [7, 14], such that pump light is present in abundance. The Stokes shift exhibited by practically all fluorophores embedded in a solid matrix provides a convenient way to spectrally separate the fluorescent from the pump light with a color filter [14]. A first spectral selection is made by the dichroic beam-splitter (DC, 565DCXT, Chroma Technology), which reflects the laser wavelength into the objective but transmits only the red-shifted fluorescence wavelength. An additional long-pass filter (LP, E590LPv2, Chroma) transmits only fluorescent light with an extinction ratio exceeding 10^6 such that the pump wavelength is in total suppressed by more than 8.5 orders of magnitude on the way to the detector.

When the photon detector of choice is not a pixelated array like a CCD camera it becomes necessary to form a spatial image by scanning the sample point after point with the detector. In a confocal setup an image of the sample is formed in a plane where a pinhole is located which is subsequently imaged onto the detector. Now the specimen is scanned and an image of the whole sample is generated point after point [1, 13]. In our setup, the pump laser is focused to a diffraction-limited spot on the sample when the epi-lens is removed. With the rotatable mirror (M1) flipped to the left port in Fig. 2.1, the fluorescence signal passes a collimating lens (CL, $f_{\mathrm{CL}} = 150\,\mathrm{mm}$). With the flip-mirror (M2) and the removable beam-splitter (BS2) removed from the path, the signal is focused onto an avalanche photodiode (APD1, id100-20 ULN, ID-Quantique) by a lens with focal length $f_{\mathrm{APD}} = 30\,\mathrm{mm}$. Therefore, for a 100× objective the magnification between the sample and the APD is 20. The small size of the active area of the APD being 20 µm the detector itself in our case functions as the pinhole which has to be confocally imaged onto the point where the pump laser illuminates the sample. The resolution of our microscope is determined by the diffraction limit at the pump wavelength. The APD is connected to an electronic circuit and finally to a computer to determine the number of detected photons. The sample can be raster scanned with a piezoelectric stage (P-542.2CL, Physik Instrumente GmbH) to obtain

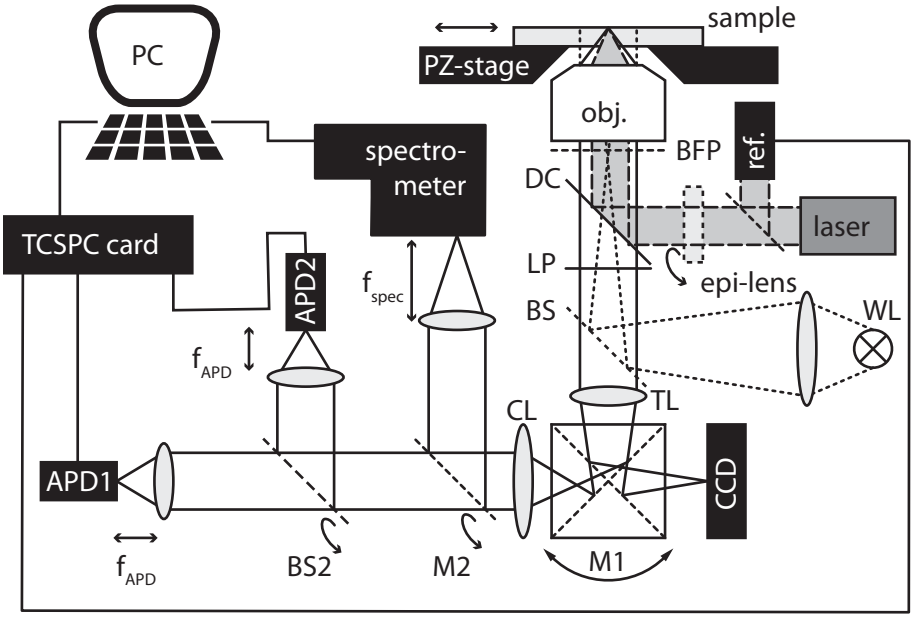

Figure 2.1: Sketch of our fluorescence-lifetime imaging microscope. The sample is mounted on a scanning stage and can be illuminated by a thermal white-light source (WL) or a laser. A rotatable mirror (M1) is used to either image the sample on a CCD camera via the tube-lens ($f_{\mathrm{TL}} = 200\,\mathrm{mm}$) or send the light to the collimating lens ($f_{\mathrm{CL}} = 150\,\mathrm{mm}$). With the flip mirror (M2) in place the sample is imaged ($f_{\mathrm{CL}} = 150\,\mathrm{mm}$) onto the entrance slit of a grating spectrograph ($f_{\mathrm{spec}} = 50\,\mathrm{mm}$). Alternatively, with M2 removed, the light arrives to a Hanbury Brown-Twiss setup, where time-resolved detectors (APD1 and APD2, $f_{\mathrm{APD}} = 30\,\mathrm{mm}$) behind a beam-splitter (BS2) allow correlation measurements. The beam-splitter BS2 can be removed for simple FLIM on APD1. The APDs are connected to a TCSPC card which is connected to a PC together with all other detectors.

an image. With the removable beam-splitter (BS2) in place the two APDs (APD1, APD2) form a Hanbury Brown-Twiss setup that allows photon-photon correlation measurements [35]. Furthermore, when the flip-mirror (M2) is in the beam path, a lens with focal length $f_{\mathrm{spec}} = 50\,\mathrm{mm}$ images the sample on the entrance slit of a grating spectrograph (SpectraPro 2300i, Acton Research) equipped with a thermo-electrically cooled Si-CCD image sensor (PIXIS:100B, Princeton Instruments) allowing spectral characterization of the detected light.

To illustrate the principle of confocal fluorescence microscopy by way of example and demonstrate the performance of our setup we show a representative measurement in Fig. 2.2. The sample is a glass coverslip onto which silver nanowires with nominal diameter of 300 nm have been spun from a solution (SLV-NW-300, Blue Nano Inc.). In a second step, a solution of polystyrene beads (F-8801, Invitrogen) with nominal

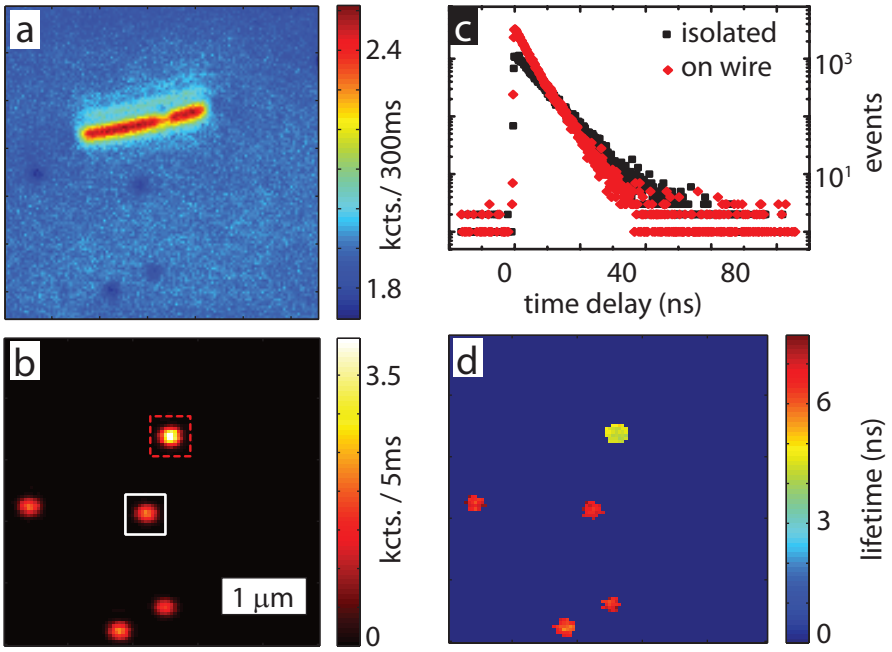

Figure 2.2: (a) Sample under white-light epi-illumination. A silver nanowire lying horizontally scatters strongly and shows up brightly. Polystyrene beads on the sample are barely visible as dark spots. (b) Confocal fluorescence-intensity image of same sample as in (a). Fluorescing beads show up as diffraction-limited bright spots. (c) Decay traces of fluorescence signal from two bright spots marked in (b). Black squares are data from fluorescing bead marked with white rectangle in (b), while red diamonds correspond to bright spot marked with dashed box in (b). (d) Fluorescence-lifetime image of area shown in (b) where false color indicates lifetime of signal collected in different pixels. The lifetime of pixels holding less than 1000 photons was clamped to zero. The fluorescing bead marked with the dashed box in (b) and located in vicinity of the nanowire, as seen from comparison with (a), has a reduced lifetime compared to its isolated neighbors, as already established in (c).

diameter 100 nm was spun onto the sample. The beads are infiltrated with fluorescing dye molecules with an emission maximum at 620 nm. Figure 2.2(a) shows a camera image of the sample under white-light epi-illumination. The dominant signal is the light scattered by an Ag nanowire lying horizontally in the upper half of the image. The polystyrene beads are barely visible as dark spots in the white-light image. The negative contrast of the beads is caused by destructive interference on the camera of the light scattered by the bead with the light reflected from the sample surface [36]. Imaging the fluorescence of the area depicted in Fig. 2.2(a) confocally with an excitation power of 0.3 µW leads to the image shown in Fig. 2.2(b). As expected, only the polystyrene beads fluoresce. Comparing the signal received from a fluorescing bead to the average number of roughly 4 background counts in a pixel yields a signal to noise ratio exceeding 500 in

Fig. 2.2(b). This background signal of several 100 Hz is dominated by the light level in the laboratory and can be easily reduced to a few 10 Hz by covering the sample, which is however unfeasible when operating the scanning probe, where a full enclosure would be necessary. At the sub-µW pump powers used in our experiments auto-fluorescence of conventional glass substrates and the optical components in our setup plays a negligible role.

2.2.3 Time-correlated single-photon counting

The technique of TCSPC measures the lifetime of a spontaneous emitter by determining the time delay $\tau = t_d - t_0$ between its excitation with a short light pulse at t_0 and the detection of the emitted fluorescent photon at t_d [12]. The thermo-electrically cooled silicon APDs (id100-20 ULN, ID-Quantique) in our setup are single-photon detectors with a timing resolution specified as 40 ps. The single-photon detection probability peaks at 35% around 500 nm and falls below 15% for wavelengths longer than 700 nm. The major strength of our APD is its extremely low dark-count rate of less than 2 Hz. This low dark-count rate together with the insensitivity of the temporal response function against count rate discriminates our APDs against the popularly used Perkin Elmer SPCM-AQR with its exceptional quantum efficiency of up to 65%.

One important restriction of all single-photon detectors is their dead time after a detection event [11]. The dead time of our APDs is specified as 50 ns. Since fluorescent photons arriving during the detector dead time are not accounted for, one would, at high detection rates, preferentially measure photon events which arrive early after the pump pulse. In order to perform a valid measurement without photon-counting statistics skewed to short times it is therefore necessary that the time between subsequent detection events is much longer than the dead time of the detector. We typically aim at photon detection rates at least a factor 10 lower than the repetition rate of our laser, in order to have practically negligible probability of missing a photon due to the detector dead time. The arrival times of the pump pulses are measured by splitting a small part of the pump beam off and sending it to a reference diode with precise timing. We employ a trigger diode (OFC-402, Becker & Hickl GmbH, ref. in Fig. 2.1) for the purpose of measuring the arrival times of the pump pulses, which we also refer to as reference pulses. Both detectors, the reference trigger diode and the APD detecting the fluorescence photons, are connected to a timing card (DPC 230, Becker & Hickl GmbH), which records the time stamps of every single reference and fluorescence event. The fact that we have at least ten times as many reference events than fluorescence photons would lead to a huge data load to be processed and stored. This problem is commonly solved by only processing the reference events directly following the detection of a signal photon [12]. Since the repetition rate of modern pulsed lasers is extremely stable, especially regarding the pulse-to-pulse variation, it is possible to infer the time delay between an excitation pulse and the emission of a fluorescent photon from the time between the fluorescent photon and the subsequent pump pulse. A very special feature of our timing card is that besides performing conventional TCSPC it can store the absolute arrival times of signals in up to 16 channels simultaneously without

any mutual dead times. The absolute-timing mode of the card makes it most versatile to measure photon-photon correlations from sub-ns timescales, as necessary for lifetime or bunching/anti-bunching measurements on fluorophores, up to ms timescales as encountered in fluorescence-correlation spectroscopy (FCS) characterizing diffusion times of fluorophores in liquid media [37].

To illustrate the working principle of FLIM and the performance of our setup at hand of an example we return to Fig. 2.2. FLIM is naturally done in parallel with confocal fluorescence imaging. The signal forming the fluorescence-intensity image, like in Fig. 2.2(b), is simply the *number* of photons collected on each position of the sample. Since each of the collected photons is recorded with its arrival time with respect to the following excitation pulse one can build a decay trace for each position on the sample. In Fig. 2.2(c) we show two such decay traces. The black squares in Fig. 2.2(c) show a histogram of the arrival times of the photons collected from the bead marked with the white square in the center of Fig. 2.2(b) as a function of time delay between the excitation pulse and their detection. Note that the number of decay events in Fig. 2.2(c) is plotted on a logarithmic scale. Before leveling off at the background level at long time delays, the decay curve follows a straight line with the slope being the fluorescence lifetime. A more detailed explanation of the functional form of the decay trace will be given in the following Section 2.2.4. The decay curve depicted by the red diamonds in Fig. 2.2(c) are the photon events collected from the top-most bead in Fig. 2.2(b), marked with the dashed box, and located in close proximity to the Ag wire [cf. Fig. 2.2(a)]. From the decay trace of the bead on the wire [Fig. 2.2(c), red diamonds] we can immediately judge that the excited molecules in that bead decay faster than those in the isolated bead [Fig. 2.2(c), black squares].

We apply the principle just illustrated for two positions on the sample to the whole scan of Fig. 2.2(b) and fit a decay trace to the photon events in every individual pixel to arrive at the fluorescence-lifetime image in Fig. 2.2(d), where we have clamped the lifetime of pixels holding less than a fixed number of photons to zero. We can immediately see that all fluorescing beads exhibit the same lifetime, except the one that was found in close proximity of the metal nanowire. It has been shown that metallic nanowires possess an enhanced LDOS in sub-wavelength vicinity of their surface [38–40]. Our fluorescence-lifetime image in Fig. 2.2(d) therefore clearly confirms that the fluorescing bead is located within the spatially tightly confined LDOS enhancement of the nanowire.

2.2.4 The maximum-likelihood fitting procedure

The decay traces in Fig. 2.2(c) hold temporal information about the decay of the molecules in the fluorescing beads used in the experiment. This Section describes how we fit a physical model to the measured data to extract quantitative information.

The number of detected photons at a certain time t after exciting the system at $t_0 = 0$ is proportional to the probability of the system to still be in its excited state at time t. If the decay rate γ of the system is a constant the functional dependence of the

decay trace must read

$$F_{A,B,\gamma}(t) = A\exp[-\gamma\, t] + B, \tag{2.1}$$

with the proportionality constant A given by the experimental circumstances and B describing background counts uncorrelated to the excitation laser. Our goal in this Section is to determine the decay rate γ, or its inverse the lifetime τ, of the excited state of the emitter from the measured decay trace $D(t)$. It is well known that the low count rates encountered in single-emitter and few-emitter experiments require special care regarding the fitting procedures to extract decay parameters [14]. For example, a least-squares fitting procedure is not applicable [41]. Nevertheless, very few publications in the field of spontaneous-emission control report how lifetimes were precisely extracted from the measured data. The treatment given here largely follows Reference [42].

We refer to the measured data-set as $\{D(t_i)\}$ from now on to make clear that it is actually a set of discrete data-points. A specific $D(t_i)$ is the number of photons detected in time bin $i \in \{1,\ldots,N\}$, which lasts from $(i-1)\Delta t$ until $i\,\Delta t$ where Δt is the constant bin size and the total measurement time is $N\Delta t$. It is clear that given the noisy measured data-set at hand it will be impossible to find a set of parameters $\{A,B,\gamma\}$ such that $F_{A,B,\gamma}(t_i) = D(t_i)$ for all t_i. However, a sensible approach is to find the parameter set $\{A,B,\gamma\}$ for which the probability of obtaining the measured data-set $\{D(t_i)\}$ is maximized. Accordingly, the term 'maximum-likelihood approach' has been coined for this procedure.

Our first task in finding the most likely set of parameters $\{A,B,\gamma\}$ is to find an expression for the probability to measure a certain set of N data-points $\{D(t_i)\}$, assuming that the true 'noiseless' set of values is given by $\{F_{A,B,\gamma}(t_i)\}$. We denote with $p\big(D(t_i), F_{A,B,\gamma}(t_i)\big)$ the probability to measure the value $D(t_i)$ at time t_i given that the underlying true value without noise sources is given by $F_{A,B,\gamma}(t_i)$. Accordingly, the probability to acquire the entire data-set $\{D(t_i)\}$ reads

$$P\big(\{D(t_i)\},\{F_{A,B,\gamma}(t_i)\}\big) = \prod_{i=1}^{N} p\big(D(t_i), F_{A,B,\gamma}(t_i)\big). \tag{2.2}$$

To proceed, we require the statistical nature of the noise in our data, i.e., we need to specify the function $p\big(D(t_i), F_{A,B,\gamma}(t_i)\big)$. Since we are counting the photons arriving within time bin i it is reasonable to assume a Poissonian probability distribution

$$p(k,\lambda) = \frac{\lambda^k}{k!}\exp[-\lambda], \tag{2.3}$$

where $p(k,\lambda)$ is the probability to measure a value k, given that the expectation value is λ. We can now evaluate $P\big(\{D(t_i)\},\{F_{A,B,\gamma}(t_i)\}\big)$ for any given data-set $\{D(t_i)\}$ after assuming a parameter set $\{A,B,\gamma\}$. The most likely parameter set $\{A,B,\gamma\}$ will be the one for which the probability P reaches its maximum. To make the task of finding the most likely parameters computationally easier it is common to minimize $-\log[P]$. Instead of maximizing the product in Eq. (2.2) we can therefore simply minimize the

merit function $M^F_{\{D(t_i)\}}\left(A,B,\gamma\right)$, which is the sum

$$\begin{aligned} M = -\log\left[P\left(\{D(t_i)\},\{F_{A,B,\gamma}(t_i)\}\right)\right] &= -\sum_{i=1}^{N}\log\left[p\left(D(t_i),F_{A,B,\gamma}(t_i)\right)\right] \\ &= -\sum_{i=1}^{N} D(t_i)\log\left[F_{A,B,\gamma}(t_i)\right] + F_{A,B,\gamma}(t_i) \\ &\quad + \log\left[D(t_i)!\right]. \end{aligned} \tag{2.4}$$

The general procedure of maximum-likelihood fitting is of course neither limited to physical processes of the form of Eq. (2.1), nor to noise of Poissonian nature described by Eq. (2.3) but can, or rather *should* be generally applied for any fitting procedure in order to relate a measurement to a physical model. It is instructive to consider the maximum-likelihood procedure for noise that leads to a normal distribution of measurement values of the form

$$p(k,\lambda,\sigma^2) = \frac{1}{\sqrt{2\pi}\sigma}\exp\left[-\frac{(k-\lambda)^2}{2\sigma^2}\right], \tag{2.5}$$

where $p(k,\lambda,\sigma^2)$ is the probability to measure the value k, given that the expectation value was λ and the distribution is characterized by the standard deviation σ. Recall that for large expectation values λ the Poissonian distribution Eq. (2.3) approaches the normal distribution Eq. (2.5) with $\sigma = \sqrt{\lambda}$. For normally distributed errors the merit function Eq. (2.2) becomes

$$M_{\{\lambda_i\},\{\sigma_i\}}(k_i) = \sum_i \frac{(k_i-\lambda_i)^2}{\sigma_i^2}. \tag{2.6}$$

We immediately recognize Eq. (2.6) as the merit function of the method of the sum of least squares. Therefore, the sum of squares as the merit function is the maximum-likelihood method for normally distributed errors. For small expectation values λ_i, the Poissonian distribution Eq. (2.3) differs significantly from the normal distribution Eq. (2.5), such that fitting procedures minimizing the sum of squares according to Eq. (2.6) give erroneous results. Often in this thesis we will encounter low count rates and small expectation values. Accordingly, all fitting procedures in this work use the merit function in Eq. (2.4). Note that the last term in Eq. (2.4) can be neglected since it only depends on the data and not on the fit parameters. We explicitly emphasize that also in the presence of a large uncorrelated background signal the maximum-likelihood method is the method of choice to arrive at fit parameters with largest fidelity. Even though it might seem counter-intuitive, subtraction of a background prior to fitting [43] will lead to erroneous results since it inevitably obscures the noise statistics.

Having established a procedure to fit our experimental decay traces it is now a valid question to ask for the uncertainty of the fit. In other words: How much less likely are other choices of decay parameters to lead to the measured data-set? Instead of a strict mathematical proof we just give qualitative insight in the approach to quantitatively

determine the certainty of the fit [42]. Recall that we arrived at our set of most-likely fit parameters by minimizing the merit function $M_{\{D(t_i)\}}(A, B, \gamma)$ given in Eq. (2.4). Since $M_{\{D(t_i)\}}(A, B, \gamma)$ has a minimum at the found fit parameters A_0, B_0, γ_0 its second derivative with respect to its arguments is a measure of the steepness of the found minimum of M. A minimum in a steep valley indicates a certain fit: Only a small variation of the fit parameter would lead us far away of the minimal value of the merit function. Mathematically, the curvature of the merit function $M(A, B, \gamma)$ with respect to the fit parameters is given by its Hessian matrix

$$H_{\alpha\beta}(M) = \frac{1}{2}\frac{\partial^2 M(A, B, \gamma)}{\partial\alpha\,\partial\beta}, \qquad \text{with } \alpha, \beta \in \{A, B, \gamma\}, \tag{2.7}$$

evaluated at the best fitting parameter set $\{A_0, B_0, \gamma_0\}$. The variances $\sigma^2(\alpha)$ for the fitting parameters $\alpha \in \{A, B, \gamma\}$ are given by the diagonal elements of the covariance matrix $\boldsymbol{V} \approx \boldsymbol{H}^{-1}$, which is well approximated by the inverse of the Hessian $\boldsymbol{H}$ given in Eq. (2.7) [42].

2.3 Suitable sources of spontaneous emission for probing LDOS

At the beginning of this Chapter we have presented fluorescing molecules as ideal local probes of the electromagnetic environment. There is however a much wider range of spontaneous emitters available in condensed matter. In the following, we will give a short overview of sources of spontaneous emission that have been put forward as promising emitters in the context of scanning-probe experiments. Our focus will be on organic dye molecules, semiconductor nanocrystals, diamond NV-centers, and rare-earth ions, all of which have successfully been attached to scanning probes. We will not review further sources of fluorescence, for example porous silicon grown on AFM tips [44] and tips coated with LiF [45] due to their limited usability as LDOS probes. For clarity, we first discuss the properties that decide about the suitability of a source as a fluorescent LDOS probe to then review the most promising candidates. We summarize the properties of the different emitters in Table 2.1.

Absorption cross-section. The absorption cross-section of a quantum emitter determines its probability to absorb a photon from the pump beam. Typically, absorption cross-sections of single emitters are many orders of magnitude smaller than the area covered by a diffraction-limited spot. Therefore, intense laser beams are necessary to efficiently excite single fluorophores. A large absorption cross-section yields large count rates while keeping parasitic background fluorescence, for example from the substrate, at a minimum.

Quantum efficiency. The quantum efficiency of an emitter is the ratio of decay events under emission of a photon compared to the total number of decays. If the rate

of non-radiative decay is denoted as γ_{nr} and the radiative decay rate as γ_r the quantum efficiency QE is

$$QE = \frac{\gamma_r}{\gamma_{nr} + \gamma_r}.$$

Measurements of a decay-rate enhancement via a brightness enhancement rely on emitters with limited quantum efficiency [46]. At constant excitation rate the intensity detected from a quantum emitter is proportional to its quantum efficiency. Since $\gamma_r \propto$ LDOS the signal from a low-QE emitter is proportional to LDOS, while for a high-QE source the brightness is independent of LDOS and only depends on pump rate [47]. Since we measure the total decay rate we favor emitters with high quantum efficiency to maximize both the response to a modified LDOS and the number of detected photons per decay event.

Decay rate. The total decay rate $\gamma_{tot} = \gamma_{nr} + \gamma_r$ of a quantum emitter should on the one hand be as high as possible to achieve the highest cycling rate. On the other hand, in TCSPC the upper bound for measurable decay rates is set by the timing resolution of the timing card or the pulse width of the exciting laser. In our case, the 165 ps resolution of our timing card sets the upper limit for measurable decay rates. In contrast, emitters with very low decay rates are difficult to measure simply because of the vanishing signal intensity. Furthermore, data analysis becomes cumbersome for emitters with decay rates much smaller than the laser repetition rate since the emitter then has likely not decayed until the arrival of the subsequent laser pulse. For our setup, we prefer emitters with lifetimes between approximately 1 and 20 ns.

Blinking. Most quantum emitters exhibit a behavior called blinking. Under constant pumping they show intermediate time periods orders of magnitude longer than their fluorescence lifetime in which they are optically inactive and therefore appear dark [48]. Most commonly, blinking is attributed to an inter-system crossing of the emitter from the optically addressable singlet state to a triplet state from which no optical transition is allowed back to the ground state, such that the triplet state has a long lifetime during which the system appears dark in an experiment [7]. Since a quantum emitter in its dark state is not available as an LDOS probe we favor emitters with as little blinking as possible.

Bleaching. Practically all fluorophores bleach after a certain number of excitation-emission cycles [14]. Bleaching can be regarded as an irreversible blinking event. Most frequently bleaching is explained as a chemical alteration of the emitter enabled by the photon energy. Since photo-bleaching permanently disables a fluorescent LDOS probe we desire emitters with high photo-stability.

Organic dye molecules

Organic dye molecules are the most widely spread sources of fluorescence. While the original push to create versatile dyes came from the dye-laser community [49],

fluorescent dyes are nowadays mostly known due to their ubiquity as fluorescent labels in the life-sciences [50–52]. The great strength of organic dye molecules is that chemists can easily add and replace functional groups in order to tune the spectral properties of absorption and emission, change the solvation behavior of the dye, or tether it to a target as a fluorescent label [53]. The typical absorption cross-section of a dye-molecule is about $\sigma_{\text{ext}} \approx 10^{-20}\,\text{m}^2$ [7, 54, 55]. Fluorescent dyes are available with quantum efficiencies ranging from only a few percent to practically unity [49]. The typical fluorescence lifetime of dye molecules is of the order of a few ns and significantly shorter total decay rates are typically a result of low quantum efficiency [51]. Blinking is encountered in practically all dye molecules and has been studied in great detail [56, 57], including effects of the environment [55, 58–60]. The greatest drawback of fluorescent molecules is that at room temperature they irreversibly bleach after typically no more than 10^6 detection events [14, 59, 61, 62]. There are only a few known molecule-host systems that do not suffer from photo-bleaching, even at room temperature, that rely on embedding the fluorophores into a crystalline matrix [63]. The growth of these crystals and the embedding of the molecules require some sophistication and only few techniques appear to be manageable by the non-specialist [64, 65].

The first report of a scanning probe decorated with fluorescing dye molecules used a micron-sized piece of a p-terphenyl crystal doped with terrylene molecules [25]. At cryogenic temperatures the excitation lines of the molecules in the crystal could be separated such that the experiment by Michaelis *et al.* constitutes the first report of microscopy done with a single molecule as a scannable light source. The rather large size of the used crystal prevents this approach from constructing a truly nanoscopic LDOS probe. We are not aware of a report of organic dye molecules attached to a scanning probe as a scannable source of fluorescence and probe for LDOS at room temperature and we speculate that photo-bleaching has been the prohibiting factor. An outstanding merit of organic dye molecules is that they can be incorporated into polymer beads which can be grown in a bottom up process and whose size can therefore be controlled on a nanometer scale [51]. These fluorescing beads are widely used as very bright sources that do not suffer from blinking due to the ensemble [51]. Recently, 20 nm sized fluorescing beads have been used as local reporters of the LDOS in strongly scattering [66] and on disordered media [67]. Due to their high brightness and small but well defined size fluorescing beads are an extremely attractive sub-wavelength source of fluorescence which we will focus on in this thesis to construct a scanning LDOS probe in Chapter 3, even at the expense of giving up the merit of having a truly single quantum system as a local reporter.

Semiconductor nanocrystals

Besides dye molecules II-VI semiconductor nanocrystals, also referred to as quantum dots, have appeared as versatile sources of fluorescence [68] and have made their breakthrough as commercially available fluorescent markers [51]. Reference [54] contains a very useful comparison between organic dyes and semiconductor nanocrystals. Measured against most organic dye molecules, which typically have a size of

about 1 nm, semiconductor nanocrystals are significantly larger, reaching up to 60 nm in diameter [54, 69]. The strength of nanocrystals is their broad-band absorption together with narrow emission spectra which can be conveniently tuned by changing the crystal size and therefore the quantum confinement [70]. The fluorescence lifetimes of semiconductor nanocrystals are typically in the range of several ns to several tens of nanoseconds. The complicated internal level scheme can lead to non-single-exponential decays [54]. Regarding photostability semiconductor nanocrystal can be superior to dye molecules [7, 69, 71], but their performance is severely limited by their pronounced blinking behavior exhibiting off-times well into the 10 s regime [54, 72]. While the exact mechanism of blinking remains a topic of intense debate, the fact that quantum dots can be intermittently off for periods ranging from ms to many seconds makes them especially troublesome candidates for scanning-probe applications [73–75]. Nevertheless, semiconductor nanocrystals have been grafted at the end of scanning probes [76]. Microscopy by illuminating a sample with the fluorescence of single nanocrystals on a scanning probe has been demonstrated by Sonnefraud *et al.* but has been severely hampered by blinking [27].

We take the opportunity to illustrate the phenomenon of blinking to also demonstrate the capability of our setup to characterize single emitters in Fig. 2.3.* The confocal fluorescence-intensity image in Fig. 2.3(a) was acquired on a single quantum dot located on a glass coverslide while illuminated with our pulsed green laser at an average power of around 3 µW. The image was acquired with the fast scan direction horizontally. Therefore, blinking causes horizontal dark stripes in the image. The instantaneous switching from on to off within a single pixel already indicates that we are dealing with a single quantum system. A rigorous proof is given in the inset of Fig. 2.3(a), where a second order correlation measurement of the emitter scanned in the main panel is depicted. The correlation function $g^2(\tau)$ was measured using a continuous-wave pump laser at 532 nm. The clear anti-bunching dip of the photon-photon correlation at $\tau = 0$ reaching below 0.5 is an unambiguous proof that we are probing a single-photon emitter.† When we plot the number of detected photons in time bins of 10 ms as a function of the time from the start of the experiment, we obtain the intensity trace depicted in Fig. 2.3(b). The intensity fluctuates strongly as a function of time. Specifically, there are two distinct values between which the brightness of the emitter switches, one being around 1 kcounts/10 ms, which corresponds to the quantum dot being in its 'bright' state, the other one lying close to zero intensity, which is the signature of the quantum dot being in its 'dark' state.

*The CdSe-core CdS/ZnCdS/ZnS-multi-shell quantum dots measured in Fig. 2.3 were synthesized by Relinde Moes in the group of Prof. Daniel Vanmaekelberg at Utrecht University following References [77, 78].

†The theoretical value of the second order correlation function at zero time delay is $g^2(\tau = 0) = (n-1)/n$, where n is the number of emitters probed [35]. Therefore, a measured value of $g^2(\tau = 0) < 0.5$ is typically taken as proof of probing a single emitter.

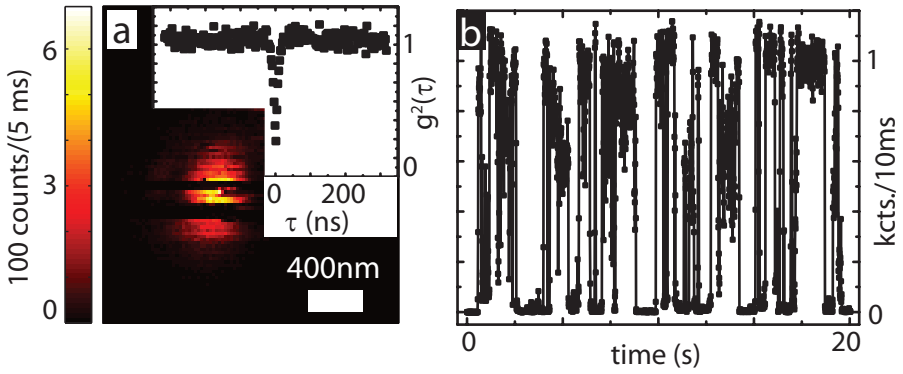

Figure 2.3: (a) Main panel shows a confocal fluorescence-intensity image of a single quantum dot. The horizontal stripes are the result of blinking. The inset shows a measurement of the second-order correlation function. The quantum dot shows a clear anti-bunching in the photon coincidences. (b) Photon arrival-time trace of single quantum dot. The two brightness plateaus and the distinct switching between them illustrate the blinking behavior of the quantum dot, interpreted as the spontaneous switching between a 'bright' and a 'dark' state.

Rare-earth ions

A very prominent source of fluorescence embedded in a transparent host medium are rare-earth ions such as erbium and yttrium which have found wide use in optical telecommunication devices [79–81]. Ensembles of erbium ions have successfully been used as LDOS probes at near infrared wavelengths in stratified systems [82]. While a multitude of excitation and emission channels are available for rare-earth ions in glass [83], a major downside of these emitters can be their excessively long lifetimes in the ms range [84, 85]. Taking typical collection efficiencies of less than 10% into account these long lifetimes entail count rates not exceeding hundreds of Hz, which would lead to prohibitively long pixel dwell time and overall measurement times in a scanning-probe application. Together with the extremely small absorption cross-sections, measured to be $10^{-25}\,\mathrm{m}^2$ for erbium in a SiO_2 matrix [80, 85], and the limited quantum yield [80, 84], signal rates are so severely limited that interrogation of a single rare-earth ion in a solid state matrix has to our knowledge remained elusive to date [86]. Aigouy *et al.* have attached erbium-doped glass particles of sub-micron size to a scanning probe and illuminated a sample with the emission of the rare-earth ions in the probe [26]. In this approach it is especially cumbersome to reduce the size of the particle containing the emitter in a top-down approach since it is composed of hard glass [83].

Diamond NV-centers

The NV-defect center is one of more than 100 defect centers in diamond [87] and has attracted enormous attention thanks to its practically unlimited photostability and optically addressable spin properties [88]. The NV-center consists of a nitrogen atom replacing a carbon atom in the diamond lattice neighboring a vacancy lattice site. At room temperature, the NV-center has a very broad emission spectrum spanning from 600 nm to about 800 nm and its lifetime in bulk diamond is 11.6 ns [87] and slightly higher in nanocrystals [23, 39]. Literature reports about the absorption cross-section and the quantum yield of diamond NV-centers, especially in nanocrystals, are contradictory. Some authors report cross-sections of NV-centers comparable to those of single dye molecules [89, 90] while the observed brightness typically suggests differently [88, 91]. Also the quantum yield is still being debated [87, 88, 90]. In our lab, Mohtashami *et al.* have explored commercially available diamond nanocrystals hosting single NV-centers [92]. Mohtashami *et al.* estimate absorption cross-sections two to three orders of magnitude lower than for dye molecules and have extracted typical quantum efficiencies of single NV-centers around 20–40% from Drexhage calibration measurements [82, 93–96]. Moreover, the decay rate of nominally identical NV-centers varies widely from nanocrystal to nanocrystal, such that a thorough characterization of each individual source is in order before it can potentially be used as an LDOS probe [39]. Despite the controversy about their properties, NV-centers hosted by nanocrystals have become widely used LDOS probes. Nanocrystals containing single NV-centers have been used to feed plasmonic antennas [23] and plasmonic waveguides [40] in experiments where they were pushed over a sample surface with the tip of an AFM. A pick-and-place technique pioneered by van der Sar *et al.* [97] was used to couple a single NV-defect to a photonic crystal cavity [98]. As truly scanning light sources diamond nanocrystals have first been attached to dielectric tips by Kühn *et al.* [24], an achievement repeated by Cuché *et al.* [99] who subsequently launched quanta of surface plasmons [28] from a single NV-center in a nanocrystal attached to a scanning probe.

2.4 A scanning probe to position a source of spontaneous emission

It is commonly agreed upon that diffraction limits the resolution obtainable by a far-field microscope [1]. Nonetheless, a multitude of methods to overcome the diffraction limit in far-field microscopy has been suggested and demonstrated in the past [103, 104]. Arguably the oldest and most wide-spread method to boost spatial resolution consists of scanning a mechanical probe whose interaction volume with the sample is small [15, 105]. When referring to scanning-probe techniques in optics one usually speaks about Near-field Scanning Optical Microscopy (NSOM) [1]. It is the precise knowledge about the probe position that enables sub-wavelength resolution in NSOM. The superior resolution obtained by scanning mechanical probes relies on two facts. First, it is

Table 2.1: Overview over relevant properties of quantum emitters for scanning-emitter lifetime-imaging microscopy.

	σ_{abs} [m^2]	QE	lifetime	blinking †	bleaching ‡
Dye molecules	$\approx 10^{-20}$ [7, 54, 55]	50–100% [51]	1–10 ns [51, 54]	10–100 ms [55, 58–60]	10^6 [59, 61, 62]
colloidal QDs	$\approx 10^{-19}$ [54, 100]	10–90% [54, 101]	10–100 ns [51, 54]	≈1 s [72, 102]	10^6–10^9 [7, 69, 71]⋆
NV-cent. in nanocrystals	10^{-24}–10^{-23} [88, 91]♭ 10^{-21}–10^{-20} [90]	100% [87] § 70% [88]	10–20 ns [23, 39]	n.a. [88, 91]	∞ [88, 91]
Er^{3+} in glass #	10^{-25} [80, 85]	26% [84]	≈ 10 ms [80, 84, 85]	n.a.	∞

† typical off-time
‡ typical number of detected photons before bleaching
♭ deduced assuming QE=1
§ QE for NV-centers is quoted to be 'high' throughout the literature. However, to our knowledge QE has never been measured on a single NV-center in a nanocrystal. Reference [87] cites a bulk value.
⋆ QDs in solution have been shown to exceed bleaching times of molecules by 2–3 orders of magnitude [71].
We chose Er^{3+} in glass as a representative of rare-earth ions in transparent dielectrics.

possible to fabricate extremely small probes, which are essentially needles with a very sharp point, which can even reach the ultimate sharpness of being terminated by a single atom at the apex [105]. Second, with piezo-electric elements these probes can be positioned and scanned with extreme precision, well below interatomic distances in solids. It has been shown in the past that it is possible to attach a fluorescent light source to the apex of a scanning probe [24–28]. In this thesis we scan a source of spontaneous emission over a sample and investigate the effect of the sample on the source. By measuring the lifetime of the scanning source as a function of position we map the LDOS of the sample.

Shear-force microscopy

In order to exploit the advantages of scanning-probe microscopy some feedback mechanism is necessary to track the surface of the sample. The most common method in NSOM to measure the interaction between the scanning probe and the sample is tuning-fork shear-force feedback [106]. In short, the scanning probe is attached to a piezo-electric quartz tuning fork [107]. The tuning fork is an electro-mechanical resonator, which can be set into mechanical oscillation when driven with an AC voltage at the resonance frequency [108]. Due to the tuning fork's complex impedance the

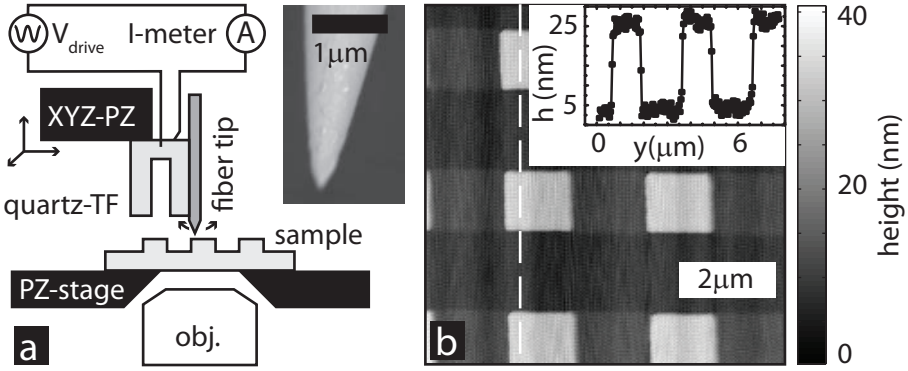

Figure 2.4: (a) Schematic of the shear-force scanning-probe setup mounted on top of our optical microscope. The sample is located on the piezo scanning stage such that it can be imaged with the objective from the bottom and accessed with the scanning probe from the top. The scanning probe is attached to a piezo scanning head. Inset: SEM image of tip of scanning probe which is a pulled glass fiber. (b) Topography measurement on a test grating with square-shaped extrusions with a period of 3 µm and a height of 21.5 nm. The inset shows a cross-section along the dashed line in the main panel.

current flowing in response to the driving voltage exhibits a typical resonance behavior as a function of driving frequency [109]. At fixed driving frequency a change in resonance frequency of the tuning fork reflects in a change in phase of the current which we employ to keep the distance between the scanning probe and the sample surface constant [1].

Our shear-force microscope

Our shear-force NSOM microscope is schematically illustrated in Fig. 2.4(a). The scanning probe, an optical glass fiber (SMF-28e, Corning) pulled to a sharp tip (Fiber Puller P-2000, Sutter Instruments Co.), is attached to the tuning fork (X32K768L104, AEL Crystals) with a small amount of super-glue (4062, Loctite). A scanning-electron micrograph of a typical fiber tip is shown in the inset of Fig. 2.4(a). The end radius of our probe is typically below 100 nm. In our setup, the scanning probe addresses the sample from the top, as shown in Fig. 2.4(a), while we can optically access the sample from the bottom with our inverted optical microscope that was discussed in detail in Section 2.2.2. We characterize the tuning fork's electromechanical resonance by driving it with an AC voltage source and varying the oscillation frequency while measuring the phase of the current flowing in response [108]. We now set the driving frequency slightly to the blue of the resonance frequency of the tuning fork. When the probe gets close to the sample surface the arising shear force effectively leads to a stiffening of the spring constant of the oscillator which causes its resonance frequency to shift [109]. Even though the microscopic origin of the shear force is not entirely

clear it has been established to work over distances of the order of 10 nm [1, 109]. The shift in resonance frequency of the tuning fork upon the probe interacting with the sample is measured in the phase of the current. A conventional PD-feedback loop is now engaged in order to keep the shift in resonance frequency constant by adjusting the height of the probe above the sample, which is achieved via a piezo-electric actuator, that can also laterally scan the probe (XYZ-PZ in Fig. 2.4(a), PXY 80 D12 and PZ 20 D12, piezosystem jena). Both the piezo-scanners for the lateral movement of the scanning head and for the sample stage are equipped with gauges that read out the precise position of the actuator which allows to both monitor the instantaneous position of the actuator and to engage a feedback loop to correct for hysteretic and drift effects.

With the scanning probe in contact with the sample and the shear-force feedback loop closed the topography of the sample surface is tracked by the probe when it is scanned across the sample plane which can be done by either moving the scanning probe or the sample stage laterally. We show a reference topography measurement in Fig. 2.4(b). The sample is a silicon test grating (TGQ1, NT-MDT Co.) with rectangular protrusions with a periodicity of 3 µm and a nominal height of 21.5 nm. The inset of Fig. 2.4(b) shows a cross-section along the dashed vertical line in the main panel, from which we can infer a vertical resolution better than 5 nm judging the spread of the data points on the horizontal plateaus. We can determine the lateral resolution of our scanning-probe setup from the fact that the steps of the sample are resolved within two sampling points, which corresponds to roughly 80 nm in the presented measurement which is limited by the sharpness of the used probe.

2.5 Conclusions

In conclusion, we have demonstrated that our confocal microscope is capable of detecting the fluorescence emitted by a single-photon source in the visible. Furthermore, our setup has the required timing resolution to perform fluorescence-lifetime imaging of single emitters with lifetimes in the nanosecond range and we have detailed the appropriate procedure to extract decay parameters from low-count-rate time-resolved data-sets. In addition to its state of the art FLIM capabilities our setup is equipped with a shear-force scanning probe that can access the near-field of any planar sample with a precision of a few ten nanometers. Regarding the choice of source we have extensively reviewed several available options and identified polymer beads infiltrated with dye molecules as the most promising candidate to construct a scanning LDOS probe. We therefore conclude that we have assembled all necessary tools for probing the LDOS of a nanophotonic structure by measuring the lifetime of a fluorescent source attached to a scanning probe.

References

[1] L. Novotny and B. Hecht, *Principles of Nano-Optics*, Cambridge University Press, Cambridge, 2006.

[2] R. Sprik, B. A. van Tiggelen, and A. Lagendijk, *Optical emission in periodic dielectrics*, Europhys. Lett. **35**, 265 (1996).

[3] B. Lounis and W. E. Moerner, *Single photons on demand from a single molecule at room temperature*, Nature **407**, 491 (2000).

[4] W. E. Moerner and L. Kador, *Optical detection and spectroscopy of single molecules in a solid*, Phys. Rev. Lett. **62**, 2535 (1989).

[5] M. Orrit and J. Bernard, *Single pentacene molecules detected by fluorescence excitation in a p-terphenyl crystal*, Phys. Rev. Lett. **65**, 2716 (1990).

[6] E. B. Shera, N. K. Seitzinger, L. M. Davis, R. A. Keller, and S. A. Soper, *Detection of single fluorescent molecules*, Chem. Phys. Lett. **174**, 553 (1990).

[7] W. E. Moerner and M. Orrit, *Illuminating single molecules in condensed matter*, Science **283**, 1670 (1999).

[8] R. Rigler, M. Orrit, and T. Basché, editors, *Single Molecule Spectroscopy*, Springer Berlin / Heidelberg, 2002.

[9] W. Moerner, *New directions in single-molecule imaging and analysis*, PNAS **104**, 12596 (2007).

[10] R. Lettow, Y. L. A. Rezus, A. Renn, G. Zumofen, E. Ikonen, S. Götzinger, and V. Sandoghdar, *Quantum interference of tunably indistinguishable photons from remote organic molecules*, Phys. Rev. Lett. **104**, 123605 (2010).

[11] W. E. Moerner and D. P. Fromm, *Methods of single-molecule fluorescence spectroscopy and microscopy*, Rev. Sci. Instrum. **74**, 3597 (2003).

[12] W. Becker, *Advanced Time-Correlated Single Photon Counting Techniques*, Springer Berlin / Heidelberg, 2005.

[13] R. L. Price and W. G. Jerome, editors, *Basic Confocal Microscopy*, Springer Berlin / Heidelberg, 2011.

[14] J. R. Lakowicz, *Principles of Fluorescence Spectroscopy*, Springer Berlin / Heidelberg, 2006.

[15] D. W. Pohl, W. Denk, and M. Lanz, *Optical stethoscopy: Image recording with resolution lambda/20*, Appl. Phys. Lett. **44**, 651 (1984).

[16] E. Betzig and R. J. Chichester, *Single molecules observed by near-field scanning optical microscopy*, Science **262**, 1422 (1993).

[17] W. P. Ambrose, P. M. Goodwin, R. A. Keller, and J. C. Martin, *Alterations of single molecule fluorescence lifetimes in near-field optical microscopy*, Science **265**, 364 (1994).

[18] H. Gersen, M. F. García-Parajó, L. Novotny, J. A. Veerman, L. Kuipers, and N. F. van Hulst, *Influencing the angular emission of a single molecule*, Phys. Rev. Lett. **85**, 5312 (2000).

[19] T. Taminiau, F. Stefani, F. Segerink, and N. van Hulst, *Optical antennas direct single-molecule emission*, Nature Photon. **2**, 234 (2008).

[20] R. J. Moerland, T. H. Taminiau, L. Novotny, N. F. van Hulst, and L. Kuipers, *Reversible polarization control of single photon emission*, Nano Lett. **8**, 606 (2008).

[21] P. Anger, P. Bharadwaj, and L. Novotny, *Enhancement and quenching of single-molecule fluorescence*, Phys. Rev. Lett. **96**, 113002 (2006).

[22] S. Kühn, U. Håkanson, L. Rogobete, and V. Sandoghdar, *Enhancement of single-molecule fluorescence using a gold nanoparticle as an optical nanoantenna*, Phys. Rev. Lett. **97**, 017402 (2006).

[23] S. Schietinger, M. Barth, T. Aichele, and O. Benson, *Plasmon-enhanced single photon emission from a nanoassembled metal-diamond hybrid structure at room temperature*, Nano Lett. **9**, 1694 (2009).

[24] S. Kühn, C. Hettich, C. Schmitt, J.-P. Poizat, and V. Sandoghdar, *Diamond colour centres as a nanoscopic light source for scanning near-field optical microscopy*, J. Microsc. **202**, 2 (2001).

[25] J. Michaelis, C. Hettich, J. Mlynek, and V. Sandoghdar, *Optical microscopy using a single-molecule light source*, Nature **405**, 325 (2000).

[26] L. Aigouy, Y. D. Wilde, and M. Mortier, *Local optical imaging of nanoholes using a single fluorescent rare-earth-doped glass particle as a probe*, Appl. Phys. Lett. **83**, 147 (2003).

[27] Y. Sonnefraud, N. Chevalier, J.-F. Motte, S. Huant, P. Reiss, J. Bleuse, F. Chandezon, M. T. Burnett, W. Ding, and S. A. Maier, *Near-field optical imaging with a CdSe single nanocrystal-based active tip*, Opt. Express **14**, 10596 (2006).

[28] A. Cuché, O. Mollet, A. Drezet, and S. Huant, *"Deterministic" quantum plasmonics*, Nano Lett. **10**, 4566 (2010).

[29] K. Lieberman, S. Harush, A. Lewis, and R. Kopelman, *A light source smaller than the optical wavelength*, Science **247**, 59 (1990).

[30] V. Sandoghdar and J. Mlynek, *Prospects of apertureless SNOM with active probes*, J. Opt. A **1**, 523 (1999).

[31] A. F. Koenderink, M. Kafesaki, C. M. Soukoulis, and V. Sandoghdar, *Spontaneous emission in the near field of two-dimensional photonic crystals*, Opt. Lett. **30**, 3210 (2005).

[32] P. I. Bastiaens and A. Squire, *Fluorescence lifetime imaging microscopy: spatial resolution of biochemical processes in the cell*, Trends Cell Biol. **9**, 48 (1999).

[33] A. E. Siegman, *Lasers*, University Science Books, Sausalito, California, 1986.

[34] W. W. Chow and S. W. Koch, *Semiconductor-Laser Fundamentals*, Springer Berlin / Heidelberg, 1999.

[35] R. Loudon, *The Quantum Theory of Light*, Oxford Science Publications, 1983.

[36] K. Lindfors, T. Kalkbrenner, P. Stoller, and V. Sandoghdar, *Detection and spectroscopy of gold nanoparticles using supercontinuum white light confocal microscopy*, Phys. Rev. Lett. **93**, 037401 (2004).

[37] R. Rigler, *Fluorescence correlations, single molecule detection and large number screening applications in biotechnology*, J. Biotechnol. **41**, 177 (1995).

[38] A. V. Akimov, A. Mukherjee, C. L. Yu, D. E. Chang, A. S. Zibrov, P. R. Hemmer, H. Park, and M. D. Lukin, *Generation of single optical plasmons in metal nanowires coupled to quantum dots*, Nature **450**, 402 (2007).

[39] R. Kolesov, B. Grotz, G. Balasubramanian, R. J. Stöhr, A. A. L. Nicolet, P. R. Hemmer, F. Jelezko, and J. Wrachtrup, *Wave-particle duality of single surface plasmon polaritons*, Nature Phys. **5**, 470 (2009).

[40] A. Huck, S. Kumar, A. Shakoor, and U. L. Andersen, *Controlled coupling of a single nitrogen-vacancy center to a silver nanowire*, Phys. Rev. Lett. **106**, 096801 (2011).

[41] J. Tellinghuisen and C. W. Wilkerson, *Bias and precision in the estimation of exponential decay parameters from sparse data*, Anal. Chem. **65**, 1240 (1993).

[42] Ž. Bajzer, T. M. Therneau, J. C. Sharp, and F. G. Prendergast, *Maximum likelihood method for the analysis of time-resolved fluorescence decay curves*, Eur. Biophys. J. **20**, 247 (1991).

[43] B. H. Husken, *Spontaneous Emission of Near-Infrared Quantum Dots Controlled with Photonic Crystals*, PhD thesis, University of Twente, 2009.

[44] H. Göttlich and W. Heckl, *A novel probe for near field optical microscopy based on luminescent silicon*, Ultramicroscopy **61**, 145 (1995).

[45] S. Sekatskii, G. Dietler, F. Bonfigli, S. Loreti, T. Marolo, and R. Montereali, *Subwavelength-size local fluorescent sources based on color centers in LiF for scanning near-field optical microscopy*, J. Lumin. **122-123**, 362 (2007).

[46] A. Kinkhabwala, Z. Yu, S. Fan, Y. Avlasevich, K. Müllen, and W. E. Moerner, *Large single-molecule fluorescence enhancements produced by a bowtie nanoantenna*, Nature Photon. **3**, 654 (2009).

[47] A. F. Koenderink, L. Bechger, H. P. Schriemer, A. Lagendijk, and W. L. Vos, *Broadband fivefold reduction of vacuum fluctuations probed by dyes in photonic crystals*, Phys. Rev. Lett. **88**, 143903 (2002).

[48] W. P. Ambrose, P. M. Goodwin, J. H. Jett, A. Van Orden, J. H. Werner, and R. A. Keller, *Single molecule fluorescence spectroscopy at ambient temperature*, Chem. Rev. **99**, 2929 (1999).

[49] U. Brackmann, *Lambdachrome Laser Dyes*, Lambda Physik, 2000.

[50] S. Weiss, *Fluorescence spectroscopy of single biomolecules*, Science **283**, 1676 (1999).

[51] I. Johnson and M. T. Spence, editors, *Molecular Probes Handbook, A Guide to Fluorescent Probes and Labeling Technologies, 11th Edition*, Invitrogen, 2010.

[52] R. W. Sabnis, *Handbook of Biological Dyes and Stains: Synthesis and Industrial Applications*, Wiley, New York, 2010.

[53] M. S. T. Gonçalves, *Fluorescent labeling of biomolecules with organic probes*, Chem. Rev. **109**, 190 (2009).

[54] U. Resch-Genger, M. Grabolle, S. Cavaliere-Jaricot, R. Nitschke, and T. Nann, *Quantum dots versus organic dyes as fluorescent labels*, Nat. Methods **5**, 763 (2008).

[55] R. Zondervan, F. Kulzer, S. B. Orlinskii, and M. Orrit, *Photoblinking of rhodamine 6G in poly(vinyl alcohol): Radical dark state formed through the triplet*, J. Phys. Chem. A **107**, 6770 (2003).

[56] E. K. L. Yeow, S. M. Melnikov, T. D. M. Bell, F. C. De Schryver, and J. Hofkens, *Characterizing the fluorescence intermittency and photobleaching kinetics of dye molecules immobilized on a glass surface*, J. Phys. Chem. A **110**, 1726 (2006).

[57] J. P. Hoogenboom, J. Hernando, E. M. H. P. van Dijk, N. F. van Hulst, and M. F. García-Parajó, *Power-law blinking in the fluorescence of single organic molecules*, ChemPhysChem **8**, 823 (2007).

[58] J. Schuster, F. Cichos, and C. von Borczyskowski, *Blinking of single molecules in various environments*, Opt. Spectrosc. **98**, 712 (2005).

[59] J. P. Hoogenboom, E. M. H. P. van Dijk, J. Hernando, N. F. van Hulst, and M. F. García-Parajó, *Power-law-distributed dark states are the main pathway for photobleaching of single organic molecules*, Phys. Rev. Lett. **95**, 097401 (2005).

[60] J. Vogelsang, R. Kasper, C. Steinhauer, B. Person, M. Heilemann, M. Sauer, and P. Tinnefeld, *A reducing and oxidizing system minimizes photobleaching and blinking of fluorescent dyes*, Angew. Chem. Int. Ed. **47**, 5465 (2008).

[61] T. Gensch, M. Böhmer, and P. F. Aramendía, *Single molecule blinking and photobleaching separated by wide-field fluorescence microscopy*, J. Phys. Chem. A **109**, 6652 (2005).

[62] C. Eggeling, A. Volkmer, and C. A. M. Seidel, *Molecular photobleaching kinetics of rhodamine 6G by one- and two-photon induced confocal fluorescence microscopy*, ChemPhysChem **6**, 791 (2005).

[63] T. Plakhotnik, E. A. Donley, and U. P. Wild, *Single molecule spectroscopy*, Annu. Rev. Phys. Chem. **48**, 181 (1997).

[64] R. Pfab, J. Zimmermann, C. Hettich, I. Gerhardt, A. Renn, and V. Sandoghdar, *Aligned terrylene molecules in a spin-coated ultrathin crystalline film of p-terphenyl*, Chem. Phys. Lett. **387**, 490 (2004).

[65] C. Toninelli, K. Early, J. Bremi, A. Renn, S. Götzinger, and V. Sandoghdar, *Near-infrared single-photons from aligned molecules in ultrathin crystalline films at room temperature*, Opt. Express **18**, 6577 (2010).

[66] M. D. Birowosuto, S. E. Skipetrov, W. L. Vos, and A. P. Mosk, *Observation of spatial fluctuations of the local density of states in random photonic media*, Phys. Rev. Lett. **105**, 013904 (2010).

[67] V. Krachmalnicoff, E. Castanié, Y. De Wilde, and R. Carminati, *Fluctuations of the local density of states probe localized surface plasmons on disordered metal films*, Phys. Rev. Lett. **105**, 183901 (2010).

[68] A. P. Alivisatos, *Semiconductor clusters, nanocrystals, and quantum dots*, Science **271**, 933 (1996).

[69] W. G. J. H. M. van Sark, P. L. T. M. Frederix, A. A. Bol, H. C. Gerritsen, and A. Meijerink, *Blueing, bleaching, and blinking of single CdSe/ZnS quantum dots*, ChemPhysChem **3**, 871 (2002).

[70] M. Bruchez, M. Moronne, P. Gin, S. Weiss, and A. P. Alivisatos, *Semiconductor nanocrystals as fluorescent biological labels*, Science **281**, 2013 (1998).

[71] A. Sukhanova, J. Devy, L. Venteo, H. Kaplan, M. Artemyev, V. Oleinikov, D. Klinov, M. Pluot, J. H. Cohen, and I. Nabiev, *Biocompatible fluorescent nanocrystals for immunolabeling of membrane proteins and cells*, Anal. Biochem. **324**, 60 (2004).

[72] M. Kuno, D. P. Fromm, H. F. Hamann, A. Gallagher, and D. J. Nesbitt, *Nonexponential "blinking" kinetics of single CdSe quantum dots: A universal power law behavior*, J. Chem. Phys. **112**, 3117 (2000).

[73] P. Frantsuzov, M. Kuno, B. Jankó, and R. A. Marcus, *Universal emission intermittency in quantum dots, nanorods and nanowires*, Nature Phys. **4**, 519 (2008).

[74] C. Galland, Y. Ghosh, A. Steinbrück, M. Sykora, J. A. Hollingsworth, V. I. Klimov, and H. Htoon, *Two types of luminescence blinking revealed by spectroelectrochemistry of single quantum dots*, Nature **479**, 203 (2011).

[75] X. Wang, X. Ren, K. Kahen, M. A. Hahn, M. Rajeswaran, S. Maccagnano-Zacher, J. Silcox, G. E. Cragg, A. L. Efros, and T. D. Krauss, *Non-blinking semiconductor nanocrystals*, Nature **459**, 686 (2009).

[76] N. Chevalier, M. J. Nasse, J. C. Woehl, P. Reiss, J. Bleuse, F. Chandezon, and S. Huant, *CdSe single-nanoparticle based active tips for near-field optical microscopy*, Nanotechnology **16**, 613 (2005).

[77] R. Koole, M. M. van Schooneveld, J. Hilhorst, C. de Mello Donegá, D. C. t. Hart, A. van Blaaderen, D. Vanmaekelbergh, and A. Meijerink, *On the incorporation mechanism of hydrophobic quantum dots in silica spheres by a reverse microemulsion method*, Chem. Mat. **20**, 2503 (2008).

[78] R. Xie, U. Kolb, J. Li, T. Basché, and A. Mews, *Synthesis and characterization of highly luminescent CdSe-core CdS/Zn0.5Cd0.5S/ZnS multishell nanocrystals*, J. Am. Chem. Soc. **127**, 7480 (2005).

[79] M. J. F. Digonnet, editor, *Rare-Earth-Doped Fiber Lasers and Amplifiers*, CRC Press, 2001.

[80] A. Polman, *Erbium implanted thin film photonic materials*, J. Appl. Phys. **82**, 1 (1997).

[81] I. Hemmilä and V. Laitala, *Progress in lanthanides as luminescent probes*, J. Fluor. **15**, 529 (2005).

[82] E. Snoeks, A. Lagendijk, and A. Polman, *Measuring and modifying the spontaneous emission rate of erbium near an interface*, Phys. Rev. Lett. **74**, 2459 (1995).

[83] L. Aigouy, Y. D. Wilde, M. Mortier, J. Giérak, and E. Bourhis, *Fabrication and characterization of fluorescent rare-earth-doped glass-particle-based tips for near-field optical imaging applications*, Appl. Opt. **43**, 3829 (2004).

[84] J. Kalkman, L. Kuipers, A. Polman, and H. Gersen, *Coupling of Er ions to surface plasmons on Ag*, Appl. Phys. Lett. **86**, 041113 (2005).

[85] W. Barnes, R. Laming, E. Tarbox, and P. Morkel, *Absorption and emission cross section of Er3+ doped silica fibers*, IEEE J. Quantum Electron. **27**, 1004 (1991).

[86] P. Bharadwaj and L. Novotny, *Plasmon-enhanced photoemission from a single Y3N@C80 fullerene*, J. Phys. Chem. C **114**, 7444 (2010).

[87] A. Gruber, A. Dräbenstedt, C. Tietz, L. Fleury, J. Wrachtrup, and C. v. Borczyskowski, *Scanning confocal optical microscopy and magnetic resonance on single defect centers*, Science **276**, 2012 (1997).

[88] F. Jelezko and J. Wrachtrup, *Single defect centres in diamond: A review*, phys. stat. sol. (a) **203**, 3207 (2006).

[89] T. Plakhotnik and R. Chapman, *Nitrogen-vacancy centers in nano-diamond reversibly decrease the luminescence quantum yield under strong pulsed-laser irradiation*, New J. Phys. **13**, 045001 (2011).

[90] R. Chapman and T. Plakhotnik, *Quantitative luminescence microscopy on nitrogen-vacancy centres in diamond: Saturation effects under pulsed excitation*, Chem. Phys. Lett. **507**, 190 (2011).

[91] C. Kurtsiefer, S. Mayer, P. Zarda, and H. Weinfurter, *Stable solid-state source of single photons*, Phys. Rev. Lett. **85**, 290 (2000).

[92] A. Mohtashami and A. F. Koenderink, to be published.

[93] K. H. Drexhage, *Influence of a dielectric interface on fluorescence decay time*, J. Lumin. **1-2**, 693 (1970).

[94] B. C. Buchler, T. Kalkbrenner, C. Hettich, and V. Sandoghdar, *Measuring the quantum efficiency of the optical emission of single radiating dipoles using a scanning mirror*, Phys. Rev. Lett. **95**, 063003 (2005).

[95] M. D. Leistikow, J. Johansen, A. J. Kettelarij, P. Lodahl, and W. L. Vos, *Size-dependent oscillator strength and quantum efficiency of CdSe quantum dots controlled via the local density of states*, Phys. Rev. B **79**, 045301 (2009).

[96] A. I. Chizhik, A. M. Chizhik, D. Khoptyar, S. Bär, A. J. Meixner, and J. Enderlein, *Probing the radiative transition of single molecules with a tunable microresonator*, Nano Lett. **11**, 1700 (2011).

[97] T. van der Sar, E. C. Heeres, G. M. Dmochowski, G. de Lange, L. Robledo, T. H. Oosterkamp, and R. Hanson, *Nanopositioning of a diamond nanocrystal containing a single nitrogen-vacancy defect center*, Appl. Phys. Lett. **94**, 173104 (2009).

[98] T. van der Sar, J. Hagemeier, W. Pfaff, E. C. Heeres, S. M. Thon, H. Kim, P. M. Petroff, T. H. Oosterkamp, D. Bouwmeester, and R. Hanson, *Deterministic nanoassembly of a coupled quantum emitter-photonic crystal cavity system*, Appl. Phys. Lett. **98**, 193103 (2011).

[99] A. Cuché, A. Drezet, Y. Sonnefraud, O. Faklaris, F. Treussart, J.-F. Roch, and S. Huant, *Near-field optical microscopy with a nanodiamond-based single-photon tip*, Opt. Express **17**, 19969 (2009).

[100] C. A. Leatherdale, W.-K. Woo, F. V. Mikulec, and M. G. Bawendi, *On the absorption cross section of CdSe nanocrystal quantum dots*, J. Phys. Chem. B **106**, 7619 (2002).

[101] X. Michalet, F. F. Pinaud, L. A. Bentolila, J. M. Tsay, S. Doose, J. J. Li, G. Sundaresan, A. M. Wu, S. S. Gambhir, and S. Weiss, *Quantum dots for live cells, in vivo imaging, and diagnostics*, Science **307**, 538 (2005).

[102] M. Nirmal, B. O. Dabbousi, M. G. Bawendi, J. J. Macklin, J. K. Trautman, T. D. Harris, and L. E. Brus, *Fluorescence intermittency in single cadmium selenide nanocrystals*, Nature **383**, 802 (1996).

[103] S. W. Hell, *Far-field optical nanoscopy*, Science **316**, 1153 (2007).

[104] S. W. Hell, *Microscopy and its focal switch*, Nat. Methods **6**, 24 (2009).

[105] G. Binnig, H. Rohrer, C. Gerber, and E. Weibel, *Surface studies by scanning tunneling microscopy*, Phys. Rev. Lett. **49**, 57 (1982).

[106] K. Karrai and I. Tiemann, *Interfacial shear force microscopy*, Phys. Rev. B **62**, 13174 (2000).

[107] K. Karrai and R. D. Grober, *Piezoelectric tip-sample distance control for near field optical microscopes*, Appl. Phys. Lett. **66**, 1842 (1995).

[108] R. D. Grober, J. Acimovic, J. Schuck, D. Hessman, P. J. Kindlemann, J. Hespanha, A. S. Morse, K. Karrai, I. Tiemann, and S. Manus, *Fundamental limits to force detection using quartz tuning forks*, Rev. Sci. Instrum. **71**, 2776 (2000).

[109] A. G. T. Ruiter, J. A. Veerman, K. O. van der Werf, and N. F. van Hulst, *Dynamic behavior of tuning fork shear-force feedback*, App. Phys. Lett. **71**, 28 (1997).

3

Scanning Emitter Fluorescence Lifetime Imaging

We report an experimental technique to map the local density of optical states of arbitrary planar nanophotonic structures. The method relies on positioning a spontaneous emitter attached to a scanning probe deterministically and reversibly with respect to its photonic environment while measuring its lifetime. We demonstrate the method by imaging the enhancement of the local density of optical states around metal nanowires. By nano-positioning, the decay rate of a point-like source of fluorescence can be reversibly and repeatedly changed by a factor of two by coupling it to the guided plasmonic mode of the wire.

3.1 Introduction

Spontaneous-emission control is at the heart of photonics, the science of engineering the generation, propagation, and absorption of light. Since the pioneering work of Purcell it is known that the emission properties of a spontaneous emitter can be tailored by its optical environment, which determines the number of final states available for the photon emitted in the transition [1]. While Purcell's derivation is only valid for certain classes of photonic systems [2], the local density of optical states (LDOS) [3] is always properly defined as the imaginary part of the Green function $\mathrm{Im}\,G$ at the source position [4] and can be thought of as the impedance imposed on a radiating source by its environment [5]. Reaching beyond spontaneous emission, the LDOS is a fundamental quantity that also reflects how the electromagnetic-mode structure affects, for example, thermal emission, radiation by accelerated charges, and forces mediated by vacuum

fluctuations [4, 6, 7]. The LDOS includes all channels offered by the environment, i.e. radiative decay into the far-field, decay into confined photonic or polaritonic resonances, and quenching induced by a lossy photonic environment. Nanophotonic structures exhibiting an LDOS structured at length scales smaller than the wavelength of light include photonic crystals, random scattering materials, and plasmonic structures, all holding promise to achieve control over all aspects of spontaneous emission, including decay rate [8–20], directionality [21, 22] and polarization [23].

To unlock the potential of nanophotonics for quantum optics, one requires tools to spatially image the LDOS on a nanometer scale [6, 7, 24, 25]. Moreover, to exploit the LDOS to its full potential, it is desirable to first image the LDOS, in order to subsequently position a source deterministically at the optimal location for the actually fabricated structure, as retrieved from the LDOS map. Drop casting of emitters, randomly or on selectively functionalized substrates, is often used to obtain LDOS data [15–19, 21]. However, in this method emitter positions are fixed after deposition and photonic properties have to be deduced from ensemble averages. Therefore, it is difficult to obtain calibrated LDOS values and impossible to first map the LDOS to then controllably place an emitter in the mapped structure. Nano-positioning techniques can assemble photonic devices with single emitters by pushing nano-objects to selected locations [26–28]. However, such iterative position-and-probe sequences are time consuming, and irreversible once the emitter is attached to the structure, limiting the applicability as an LDOS-imaging tool. These deficiencies can be overcome by scanning-probe techniques. In a milestone experiment, Ambrose *et al.* imaged the LDOS of a metallized scanning probe using a single emitter fixed in a substrate as a local reporter [29]. Such a metallized probe was furthermore used to control the directionality of emission of a single molecule [30, 31]. A further major achievement was imaging of the LDOS of judiciously engineered optical antennas attached to a scanning probe [12, 14]. Ground-breaking experiments have been performed also in the converse geometry, where the intensity of emitters attached to sharp probes is monitored while scanning them through the near field of sub-wavelength structures [32–34]. Such scanning of point-like light sources holds great promise for LDOS mapping and nano-mechanical manipulation [9], since it is directly compatible with the constraints of planar nano-fabrication technologies. Remarkably, even though eagerly anticipated, application of scanning light sources to map LDOS has remained elusive.

In this Chapter, we report a nanoscale LDOS-imaging technique that combines scanning-probe near-field optical microscopy with fluorescence-lifetime imaging (FLIM) to map the LDOS around nanoscopic structures by reversible and on-demand positioning of a single nanometer-sized source of fluorescence. As a paradigmatic example, we investigate Au and Ag metal nanowires, structures of significant interest for plasmon quantum optics [15–17]. We manipulate the decay rate of point-like sources of fluorescence reversibly and repeatedly by scanning them relative to plasmonic nanowires. At selected source positions a significant fraction of decay events can be funneled into a guided mode, proving the possibility to control nano-mechanically by scanning the source both *when* and *where to* photons are emitted.

3.2 Experimental setup

The building blocks of our experimental setup have been introduced in detail in Chapter 2. The integral components are only briefly reviewed here. In short, our scanning-emitter fluorescence-lifetime imaging microscope is a home-built confocal FLIM system based on an inverted microscope, equipped with a scanning probe that addresses the photonic structure from above [Fig. 3.1(a)]. As a benchmark experiment, we investigate Ag and Au nanowires deposited on a cleaned glass coverslip. The source of spontaneous emission in our experiments, for brevity termed 'the source' in the remainder, is a polystyrene bead with a diameter of 100 nm, infiltrated with approximately 10^3 randomly oriented dye molecules, a fluorescence peak at 560 nm, and a quantum efficiency close to 1 (Fluospheres F8800, Invitrogen). The scanning probe, a pulled glass fiber with an end radius of around 100 nm attached to an xyz-piezo arm, is held at a constant distance of several nm to the sample surface by shear force feedback [4]. This distance and the size of the fluorescing bead minimize the effect of quenching in our experiment [13]. We dip the probe into a solution of PMMA in anisole and subsequently approach it to a bead (deposited by spin-coating on the sample), which we locate by its fluorescence on a CCD camera. The polymer promotes the attachment of a bead to the tip. The light source is pumped by a 532 nm pulsed laser, operating at 10 MHz with a pulse duration <10 ps, focused to a diffraction-limited spot by a 100× objective (NA 0.95). The fluorescence emitted by the source is collected by the same optics, passes the dichroic beam splitter and an additional long-pass filter to be focused onto an avalanche photodiode (APD). The 20 µm active area of the APD and 20× magnification between sample and detector result in a confocal arrangement. The APD is connected to a timing card, recording the arrival times of the laser pulses and the fluorescence photons. Scanning the probe through the laser focus confirms the attachment of a fluorescing bead as shown in the fluorescence-intensity map in Fig. 3.2(a). We determine the lifetime of the source on the probe by analyzing the arrival times of the fluorescence photons in the region marked with the box in Fig. 3.2(a) in Fig. 3.2(b). Our scanning source exhibits a single-exponential decay with a lifetime of 6.4 ns.

3.3 Results

We now use the probe to map the LDOS of a photonic structure, a template grown Au nanowire [35] with a length of several µm and a diameter of ca. 250 nm [Fig. 3.1(c)]. We position the probe in the laser focus, as established in Fig. 3.2(a), such that the source is continuously excited and its fluorescence detected. The sample with the wire is now raster scanned underneath the fixed probe, where it is detected as a signature in the shear-force feedback signal (data not shown). The acquired arrival times of all photons together with the positioning information allow us to determine the decay dynamics of the source for each position relative to the wire. An excellent fit is obtained to a single-exponential decay with a fixed background established from a reference

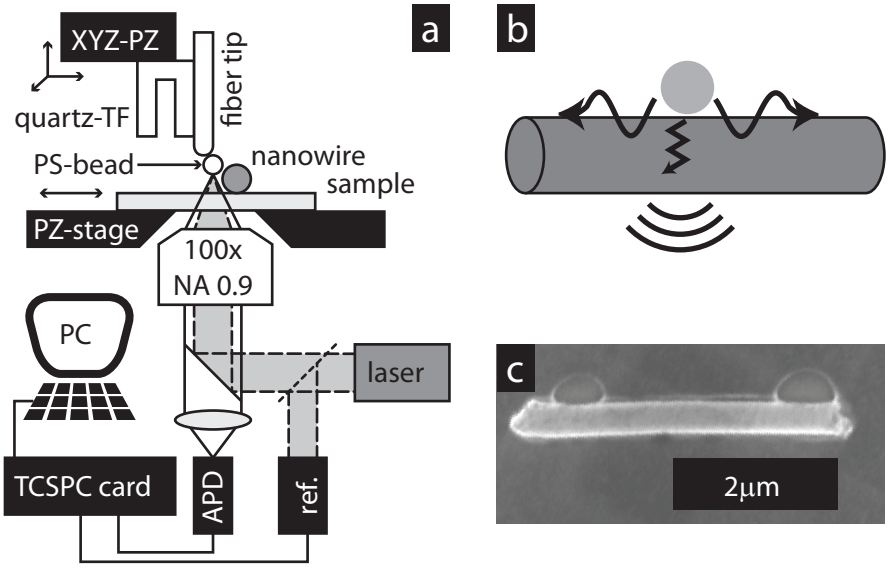

Figure 3.1: (a) Schematic of experimental setup. The fluorescent source is attached to a scanning probe and positioned with respect to the structure of interest. A pulsed pump laser is focused onto the source whose fluorescence is collected by the same microscope objective. The fluorescence is split off by a dichroic beam-splitter and a color filter (not sketched) and focused onto an APD. (b) Schematic of nanowire with light source in its vicinity. The decay channels, radiative, non-radiative, and into surface plasmons are indicated. Plasmons may decay via absorption in the wire or radiation from wire end. (c) SEM micrograph of an Au nanowire.

measurement. We use the Poissonian-statistics maximum-likelihood algorithm outlined in Chapter 2 to fit photon arrival-time data. As the main result of this Chapter, Fig. 3.3(a) shows a spatial map of the lifetime of the source as a function of position with respect to the nanowire. We observe a pronounced reduction in lifetime of the source when it is close to the wire (position confirmed by simultaneously acquired topography, not shown). The black squares in Fig. 3.3(b) show the first row of Fig. 3.3(a), with the grey bars illustrating the 3σ error interval. While the lifetime of the source is around 7 ns when it is far from the wire, it drops rapidly to around 4 ns as soon as the distance between source and wire is of the order of the wire radius. Having passed the wire, the lifetime recovers its original value. The red points in Fig. 3.3(b) take into account all horizontal scan lines in Fig. 3.3(a). This measurement clearly shows that we can reversibly change the excited-state lifetime of the source via its position with respect to the nanowire. The lifetime reported in Fig. 3.3(a) is inversely proportional to and therefore an unambiguous measure for the LDOS, i.e. $\mathrm{Im}\,G$, at the emission frequency. The ability to image $\mathrm{Im}\,G$ for any planar nanophotonic system is the main result of this Chapter. As opposed to position-and-probe techniques [26], our method is a real imaging technique able to repeatedly measure LDOS and calibrate the source

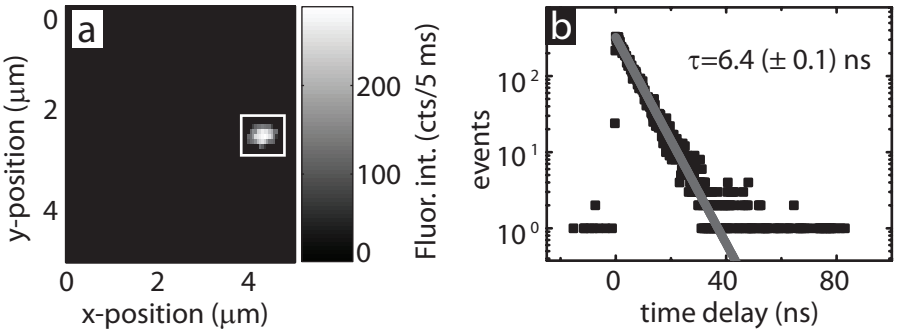

Figure 3.2: (a) Fluorescence-intensity map of fluorescing probe scanned across unpatterned coverglass. The bright region corresponds to where the probe passes the laser focus. The signal to background ratio exceeds 10^3 at a pump power of 0.2 μW. (b) Decay trace of photon events from probe positions within box in (a), revealing a single-exponential decay with 6.4 ns time constant (grey line).

in situ. In contrast to earlier work, where the LDOS around simple plasmon antennas attached to scanning probes was measured by scanning the antenna with respect to an emitter fixed in a substrate [12–14, 29], our technique can map the LDOS in any planar photonic system, such as ubiquitous lithographically prepared plasmonic and metamaterial systems. The vertical resolution of our technique is set by the quality of the feedback mechanism and has been shown to be around 5 nm in Chapter 2. The lateral resolution is set by the size of the fluorescing probe, which has a diameter of 100 nm in the presented measurements. The detection rates achieved with this source are sufficient to determine its lifetime with an accuracy of about 25% within 10 ms, such that a reasonable imaging speed of 100 pixels/s is achievable while no appreciable bleaching of the source is visible within 10^4 pixels.

3.4 Discussion

We proceed to interpret the LDOS measured in the particular structure reported in Fig. 3.3(a). The doubling of the decay rate is a clear indication of the increased LDOS in the vicinity of the nanowire. The spatial extent of the lifetime reduction is of the order of the wire radius, as was theoretically predicted on the basis that the change in decay rate occurs mostly due to coupling of the emitter to a guided plasmonic mode of the nanowire [36]. This scaling is confirmed by the blue line in Fig. 3.3(b), showing the calculated normalized intensity of the fundamental mode.* Surprisingly, the magnitude of the measured LDOS enhancement is comparable to reported values for single NV-centers in diamond attached to Ag nanowires [18], despite the much smaller

*The mode intensity has been calculated by Yuntian Chen using finite element modeling and assuming a lossless nanowire (250 nm diameter, $\epsilon = -7.911$, $\lambda = 560$ nm) in an effective host index $n = 1.25$. This simple model retains all salient spatial features of the LDOS [37].

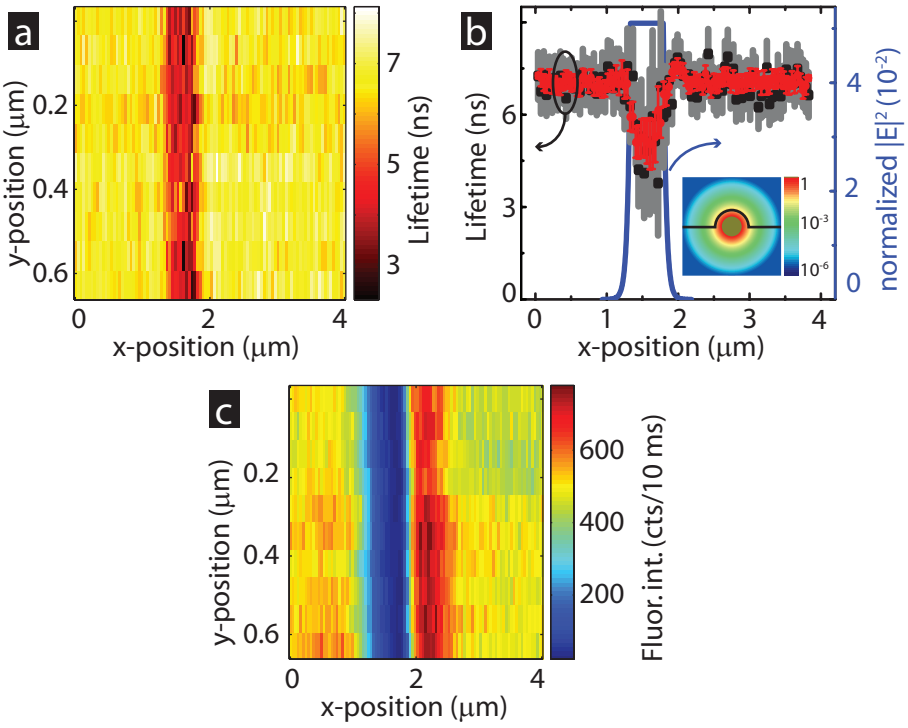

Figure 3.3: (a) Lifetime map of source scanned with respect to an Au nanowire. Close to the wire, the lifetime is reduced to half its original value. (b) Black squares: Cross-section through first row in (a). Grey error-bars indicate 3σ confidence interval obtained from the covariance matrix of the fit. Red circles: Lifetime values obtained from averaging all horizontal scan lines in (a) with 3σ error-bars. Blue line: Intensity of the fundamental wire mode (250 nm diameter) along the probe trace (55 nm from wire surface) as indicated in inset. (c) Fluorescence-intensity map obtained during measurement that yielded (a) showing a change in apparent brightness of the source in the vicinity of the wire.

diamond-nanocrystal size (50 nm). While physical size clearly limits the positioning accuracy, making the bead physically smaller does not necessarily improve resolution, since the two-level system inside the bead does not get optically closer to the wire if the bead index simultaneously increases (as in diamond). This counterintuitive argument is similar to the argument that the perturbative strength of a near-field probe scales with optical size, i.e. polarizability, not simply physical size [9].

Figure 3.3(c) shows the integrated number of detected photons as a function of probe position from the same scan that yielded Fig. 3.3(a). Similar fluorescence-intensity maps were obtained in earlier experiments with fluorescent scanning probes [32]. The wire in close proximity to the source suppresses its apparent brightness by up to ten times, while there is a region of enhanced fluorescence on the right-hand side of the

wire. The spatial width of these features is of the order of the wire diameter. Such fluorescence-intensity data is much more complicated to interpret than lifetime maps as Fig. 3.3(a) [32, 38], since it is a convolution of pump-field intensity, collection efficiency and rate enhancements. The wire causes an enhancement of pump field (polarized perpendicularly to the wire axis) on the wire sides and a suppression behind the wire, similar to the case of metallic Mie-spheres [2]. We attribute the fluorescence enhancement in Fig. 3.3(c) to such pump-field enhancement. The asymmetry can be explained by an asymmetry in the attachment of the bead to the scanning probe. An influence by the scan direction can be ruled out since consecutive rows in Fig. 3.3(c) are acquired in alternating directions. Besides pump-field suppression, non-radiative channels offered by the wire reduce the observed fluorescence intensity. We argue that the dominant non-radiative decay process in our system is the generation of plasmons, since quenching occurs at emitter-metal distances of only few nanometers [12, 13], much smaller than our source diameter and source-wire separation. While both the observed change in rate and intensity are likely not due to quenching, but rather to excitation of plasmons, a measurement of the LDOS = $\mathrm{Im}\, G$ necessarily only reports the sum of all channels [cf. Fig. 3.1(b)].

As an independent, complementary experiment we also studied single-crystalline Ag nanowires. While the plasmonic mode structure of Ag and Au wires is comparable, the exact ratios of decay rates into photons and plasmons will quantitatively differ for different materials [37]. The more advantageous loss characteristics enable us to both report the LDOS in the vicinity of an Ag wire, and simultaneously obtain a quantitative estimate for the fraction of decay events into plasmons launched on the silver wire. With our scanning probe we position a fluorescing bead on an Ag nanowire with a length of about 2 µm and a diameter of 300 nm (SLV-NW-300, Blue Nano Inc.). The deposited bead shows up as a faint signature from the scattered intensity in the wire center on a CCD camera under white-light illumination [Fig. 3.4(a)]. In the fluorescence image from the same system under laser wide-field illumination the fluorescing bead appears as a bright source of emission, while the wire ends are also bright [Fig. 3.4(b)]. This confirms that the emitters indeed decay into a plasmon that can only couple to free space at irregularities such as the wire ends. A cross-section along the wire shows the central peak from the photons emitted into free space and two smaller ones from the wire ends, corresponding to quanta emitted into a plasmon [Fig. 3.4(c)]. The data [black points in Fig. 3.4(c)] are fitted well (red line) with three peaks [green lines]. The area under the central peak is about four times the sum of the areas under the peaks at the wire ends. We therefore conclude that the β factor, i.e. the fraction of quanta emitted into the wire mode, is around 20% where we have neglected plasmon loss en route to the wire ends. We also measured the decay of the source on the probe away from the wire [blue squares in Fig. 3.4(d)] and after coupling to the wire [green diamonds]. Evidently, the lifetime of the source is drastically reduced by positioning it on the wire. We have fitted both curves with a bi-exponential decay [red lines in Fig. 3.4(d)]. The source on the probe is fitted excellently with a slow component of 6.2 ns, a relative amplitude weight of 28%, and a fast component of 1.8 ns. The same source on the wire has a slow component of 1.4 ns, a weight of 4.8%,

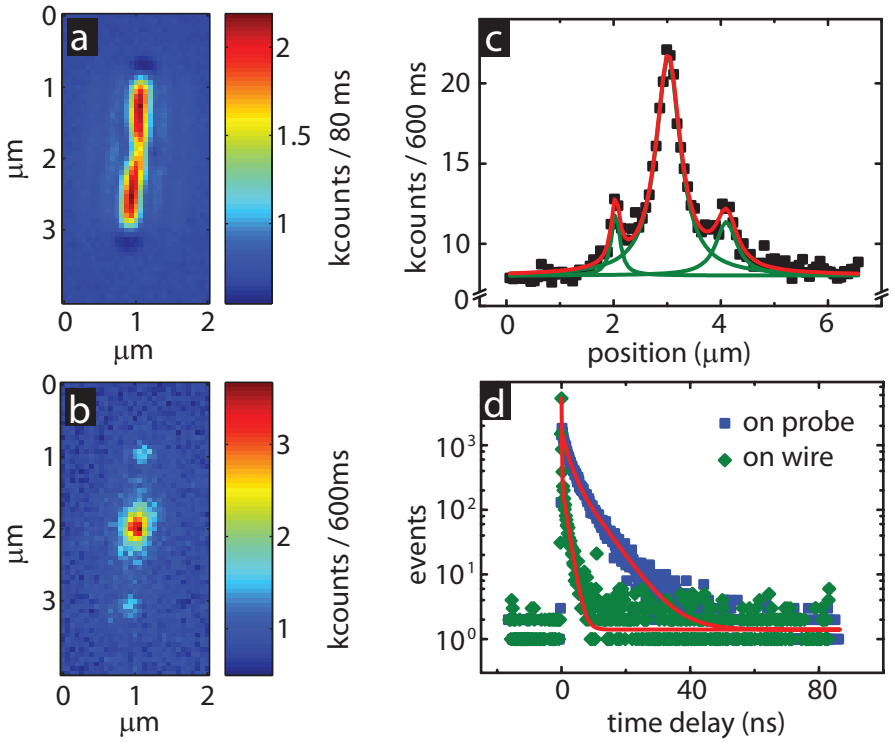

Figure 3.4: (a) Ag wire with attached bead in white-light illumination imaged on CCD camera. (b) Fluorescence image of structure in (a) under wide-field illumination by pump laser. Light emerges from the bead and from wire ends. (c) Black points: Cross-section along wire obtained by binning the central 10 columns in (b). Red line: Fit to data with three peaks (green lines). (d) Decay traces of light source on probe away (blue squares) and after deposition on Ag nanowire (green diamonds). Red lines are bi-exponential fits.

and a fast decay of 0.1 ns. A conservative estimate for the rate enhancement is 4.4 (ratio of slow components). Another estimator is the first moment of the time traces (4.3 ns off vs. 0.5 ns on the wire), which yields an enhancement ratio of 9. Both values are higher than the one obtained in the scanning-emitter experiments which can be attributed to the fact that there the source is kept at a distance of several nm above the surface.

3.5 Conclusions and outlook

In conclusion, we presented a technique to map the local density of optical states, $\mathrm{Im}\,G$, of arbitrary photonic structures with nanometer resolution. Such scanning-emitter lifetime-imaging is suited to exploit the back-action of the photonic environment on a

spontaneous emitter for a plethora of structures of current interest, hitherto inaccessible to established near-field and far-field techniques. Our work shows repeated switching of the decay rate of a point-like light source by a factor of two by reversible and on-demand positioning of an emitter within its nanoscale photonic environment. This constitutes a major step towards full nano-mechanical control over all aspects of spontaneous emission, including decay rate, directionality and spectral composition. In the current race towards scanning just a single quantum system [32, 33], our method will possibly even give access to the reverse process of spontaneous emission, i.e., the absorption of single photons in the vicinity of nanostructures [39, 40], as well as position-dependent coupling, energy transfer and photon-photon correlations between emitters linked by a nanophotonic structure [41].

In our opinion, the main obstacle on the way to a single quantum emitter on a scanning probe as an LDOS reporter is to find a stable, non-blinking source with a high quantum efficiency [42, 43]. Even if a single emitter has successfully been attached to a scanning probe, it first has to be thoroughly characterized regarding its lifetime, quantum efficiency [44] and dipole orientation [45], before it can usefully be employed as an LDOS probe. Although readily available, these characterization procedures already require a significant photon budget and exclude all conventional dyes as single-emitter LDOS probes due to their bleaching behavior. Furthermore, even with an ideal and fully characterized source at hand, for a full characterization of the LDOS one would not only require a single emitter with a known fixed dipole moment but also a technique to rotate the emitter. Since such a manipulation technique currently seems out of reach, fluorescing beads with ensembles of emitters appear as rather favorable candidates for LDOS imaging compared to single emitters.

Finally, attachment of a fluorescing source to a scanning probe remains a painfully tedious process for the experimentalist. We therefore strongly advocate the development of techniques to quickly and reliably attach a fluorescing species to the tip of a scanning probe. Indeed, various functionalization techniques for the specific attachment of nanoscopic objects to surfaces, especially glass, are readily available [46]. The main challenge will be to confine functionalization to the extreme end of a scanning probe. Importantly, however, all chemical functionalization procedures work in liquid environments [46]. In fact, moving scanning-emitter lifetime-imaging microscopy into liquids is not out of reach [47]. Such a watery environment would not only unlock the potential of chemical functionalization and thereby allow quick and easy replenishing of a bleached tip but would furthermore provide the environment in which practically all fluorescing emitters were designed to be used and therefore perform at their best. We believe that all necessary techniques, though currently still spread among very different communities [42, 46], are available to turn scanning-emitter fluorescence-lifetime imaging into a standard method.

References

[1] E. M. Purcell, *Spontaneous emission probabilities at radio frequencies*, Phys. Rev. **69**, 681 (1946).

[2] A. F. Koenderink, *On the use of Purcell factors for plasmon antennas*, Opt. Lett. **35**, 4208 (2010).

[3] R. Sprik, B. A. van Tiggelen, and A. Lagendijk, *Optical emission in periodic dielectrics*, Europhys. Lett. **35**, 265 (1996).

[4] L. Novotny and B. Hecht, *Principles of Nano-Optics*, Cambridge University Press, Cambridge, 2006.

[5] J.-J. Greffet, M. Laroche, and F. Marquier, *Impedance of a nanoantenna and a single quantum emitter*, Phys. Rev. Lett. **105**, 117701 (2010).

[6] Y. D. Wilde, F. Formanek, R. Carminati, B. Gralak, P.-A. Lemoine, K. Joulain, J.-P. Mule, Y. Chen, and J.-J. Greffet, *Thermal radiation scanning tunnelling microscopy*, Nature **444**, 740 (2006).

[7] M. Kuttge, E. J. R. Vesseur, A. F. Koenderink, H. J. Lezec, H. A. Atwater, F. J. García de Abajo, and A. Polman, *Local density of states, spectrum, and far-field interference of surface plasmon polaritons probed by cathodoluminescence*, Phys. Rev. B **79**, 113405 (2009).

[8] P. Lodahl, A. F. van Driel, I. S. Nikolaev, A. Irman, K. Overgaag, D. Vanmaekelbergh, and W. L. Vos, *Controlling the dynamics of spontaneous emission from quantum dots by photonic crystals*, Nature **430**, 654 (2004).

[9] A. F. Koenderink, M. Kafesaki, C. M. Soukoulis, and V. Sandoghdar, *Spontaneous emission in the near field of two-dimensional photonic crystals*, Opt. Lett. **30**, 3210 (2005).

[10] L. Sapienza, H. Thyrrestrup, S. Stobbe, P. D. Garcia, S. Smolka, and P. Lodahl, *Cavity quantum electrodynamics with Anderson-localized modes*, Science **327**, 1352 (2010).

[11] M. D. Birowosuto, S. E. Skipetrov, W. L. Vos, and A. P. Mosk, *Observation of spatial fluctuations of the local density of states in random photonic media*, Phys. Rev. Lett. **105**, 013904 (2010).

[12] S. Kühn, U. Håkanson, L. Rogobete, and V. Sandoghdar, *Enhancement of single-molecule fluorescence using a gold nanoparticle as an optical nanoantenna*, Phys. Rev. Lett. **97**, 017402 (2006).

[13] P. Anger, P. Bharadwaj, and L. Novotny, *Enhancement and quenching of single-molecule fluorescence*, Phys. Rev. Lett. **96**, 113002 (2006).

[14] J. N. Farahani, D. W. Pohl, H.-J. Eisler, and B. Hecht, *Single quantum dot coupled to a scanning optical antenna: A tunable superemitter*, Phys. Rev. Lett. **95**, 017402 (2005).

[15] A. V. Akimov, A. Mukherjee, C. L. Yu, D. E. Chang, A. S. Zibrov, P. R. Hemmer, H. Park, and M. D. Lukin, *Generation of single optical plasmons in metal nanowires coupled to quantum dots*, Nature **450**, 402 (2007).

[16] H. Wei, D. Ratchford, X. E. Li, H. Xu, and C.-K. Shih, *Propagating surface plasmon induced photon emission from quantum dots*, Nano Lett. **9**, 4168 (2009).

[17] Y. Fedutik, V. V. Temnov, O. Schöps, U. Woggon, and M. V. Artemyev, *Exciton-plasmon-photon conversion in plasmonic nanostructures*, Phys. Rev. Lett. **99**, 136802 (2007).

[18] R. Kolesov, B. Grotz, G. Balasubramanian, R. J. Stöhr, A. A. L. Nicolet, P. R. Hemmer, F. Jelezko, and J. Wrachtrup, *Wave-particle duality of single surface plasmon polaritons*, Nature Phys. **5**, 470 (2009).

[19] J. P. Hoogenboom, G. Sanchey-Mosteiro, G. C. des Francs, D. Heinis, G. Lagay, A. Dereux, and N. F. van Hulst, *The single molecule probe: Nanoscale vectorial mapping of photonic mode density in a metal nanocavity*, Nano Lett. **9**, 1189 (2009).

[20] V. Krachmalnicoff, E. Castanié, Y. De Wilde, and R. Carminati, *Fluctuations of the local density of states probe localized surface plasmons on disordered metal films*, Phys. Rev. Lett. **105**, 183901 (2010).

[21] A. G. Curto, G. Volpe, T. H. Taminiau, M. P. Kreuzer, R. Quidant, and N. F. van Hulst, *Unidirectional emission of a quantum dot coupled to a nanoantenna*, Science **329**, 930 (2010).

[22] K. G. Lee, X. Chen, H. Eghlidi, P. Kukura, R. Lettow, A. Renn, V. Sandoghdar, and S. Götzinger, *A planar dielectric antenna for directional single-photon emission and near-unity collection efficiency*, Nature Photon. **5**, 166 (2011).

[23] R. J. Moerland, T. H. Taminiau, L. Novotny, N. F. van Hulst, and L. Kuipers, *Reversible polarization control of single photon emission*, Nano Lett. **8**, 606 (2008).

[24] M. Frimmer, T. Coenen, and A. F. Koenderink, *Signature of a Fano resonance in a plasmonic metamolecule's local density of optical states*, Phys. Rev. Lett. **108**, 077404 (2012).

[25] C. Chicanne, T. David, R. Quidant, J. C. Weeber, Y. Lacroute, E. Bourillot, A. Dereux, G. Colas des Francs, and C. Girard, *Imaging the local density of states of optical corrals*, Phys. Rev. Lett. **88**, 097402 (2002).

[26] S. Schietinger, M. Barth, T. Aichele, and O. Benson, *Plasmon-enhanced single photon emission from a nanoassembled metal-diamond hybrid structure at room temperature*, Nano Lett. **9**, 1694 (2009).

[27] A. Huck, S. Kumar, A. Shakoor, and U. L. Andersen, *Controlled coupling of a single nitrogen-vacancy center to a silver nanowire*, Phys. Rev. Lett. **106**, 096801 (2011).

[28] T. van der Sar, E. C. Heeres, G. M. Dmochowski, G. de Lange, L. Robledo, T. H. Oosterkamp, and R. Hanson, *Nanopositioning of a diamond nanocrystal containing a single nitrogen-vacancy defect center*, Appl. Phys. Lett. **94**, 173104 (2009).

[29] W. P. Ambrose, P. M. Goodwin, R. A. Keller, and J. C. Martin, *Alterations of single molecule fluorescence lifetimes in near-field optical microscopy*, Science **265**, 364 (1994).

[30] H. Gersen, M. F. García-Parajó, L. Novotny, J. A. Veerman, L. Kuipers, and N. F. van Hulst, *Influencing the angular emission of a single molecule*, Phys. Rev. Lett. **85**, 5312 (2000).

[31] T. Taminiau, F. Stefani, F. Segerink, and N. van Hulst, *Optical antennas direct single-molecule emission*, Nature Photon. **2**, 234 (2008).

[32] J. Michaelis, C. Hettich, J. Mlynek, and V. Sandoghdar, *Optical microscopy using a single-molecule light source*, Nature **405**, 325 (2000).

[33] A. Cuché, O. Mollet, A. Drezet, and S. Huant, *"Deterministic" quantum plasmonics*, Nano Lett. **10**, 4566 (2010).

[34] L. Aigouy, Y. D. Wilde, and M. Mortier, *Local optical imaging of nanoholes using a single fluorescent rare-earth-doped glass particle as a probe*, Appl. Phys. Lett. **83**, 147 (2003).

[35] W. Lee, R. Ji, U. Gösele, and K. Nielsch, *Fast fabrication of long-range ordered porous alumina membranes by hard anodization*, Nature Mater. **5**, 741 (2006).

[36] D. E. Chang, A. S. Sørensen, P. R. Hemmer, and M. D. Lukin, *Strong coupling of single emitters to surface plasmons*, Phys. Rev. B **76**, 035420 (2007).

[37] Y. Chen, T. R. Nielsen, N. Gregersen, P. Lodahl, and J. Mørk, *Finite-element modeling of spontaneous emission of a quantum emitter at nanoscale proximity to plasmonic waveguides*, Phys. Rev. B **81**, 125431 (2010).

[38] T. H. Taminiau, F. D. Stefani, and N. F. van Hulst, *Single emitters coupled to plasmonic nano-antennas: angular emission and collection efficiency*, New J. Phys. **10**, 105005 (2008).

[39] M. Celebrano, P. Kukura, A. Renn, and V. Sandoghdar, *Single-molecule imaging by optical absorption*, Nature Photon. **5**, 95 (2011).

[40] A. Gaiduk, M. Yorulmaz, P. V. Ruijgrok, and M. Orrit, *Room-temperature detection of a single molecule's absorption by photothermal contrast*, Science **330**, 353 (2010).

[41] D. Martín-Cano, L. Martín-Moreno, F. J. García-Vidal, and E. Moreno, *Resonance energy transfer and superradiance mediated by plasmonic nanowaveguides*, Nano Lett. **10**, 3129 (2010).

[42] X. Wang, X. Ren, K. Kahen, M. A. Hahn, M. Rajeswaran, S. Maccagnano-Zacher, J. Silcox, G. E. Cragg, A. L. Efros, and T. D. Krauss, *Non-blinking semiconductor nanocrystals*, Nature **459**, 686 (2009).

[43] C. Galland, Y. Ghosh, A. Steinbrück, M. Sykora, J. A. Hollingsworth, V. I. Klimov, and H. Htoon, *Two types of luminescence blinking revealed by spectroelectrochemistry of single quantum dots*, Nature **479**, 203 (2011).

[44] B. C. Buchler, T. Kalkbrenner, C. Hettich, and V. Sandoghdar, *Measuring the quantum efficiency of the optical emission of single radiating dipoles using a scanning mirror*, Phys. Rev. Lett. **95**, 063003 (2005).

[45] M. A. Lieb, J. M. Zavislan, and L. Novotny, *Single-molecule orientations determined by direct emission pattern imaging*, J. Opt. Soc. Am. B **21**, 1210 (2004).

[46] I. Johnson and M. T. Spence, editors, *Molecular Probes Handbook, A Guide to Fluorescent Probes and Labeling Technologies, 11th Edition*, Invitrogen, 2010.

[47] W. H. J. Rensen, N. F. van Hulst, and S. B. Kämmer, *Imaging soft samples in liquid with tuning fork based shear force microscopy*, Appl. Phys. Lett. **77**, 1557 (2000).

4

Scattering and Spontaneous Emission by Electric Dipoles

This Chapter gives an introduction to the theoretical framework that is used to describe the scattering of light by small particles throughout this thesis. Furthermore, it describes the classical electrodynamic approach taken to calculate the decay-rate enhancement of dipolar emitters in complex photonic environments. This Chapter does not contain any new results that could not be found in the literature. It is much rather intended as a concise introduction to dipolar scattering theory for the unfamiliar reader in order to make the theoretical part of this thesis mostly self contained.

4.1 Introduction

The theory of electrodynamics might seem simple when considering that it is set entirely by the four Maxwell equations together with two constitutive equations describing the involved materials [1]. It however turns out that when considering any but the simplest electrodynamic problem, finding a solution to Maxwell's equations is challenging to say the least. Therefore, a variety of schemes and techniques have been developed in order to simplify the search for valid solutions [2]. One well known example is the concept of lumped circuit elements. In a lumped-element framework anyone mastering basic arithmetics can understand and design electrical circuits with powerful functionality and therefore put Maxwell's equations to work [3]—under the constraint that the circuit

formalism describing resistors, capacitors, and inductors connected with conductors breaks down when the signal frequencies correspond to wavelengths that become comparable to the physical circuit size or electrodynamic effects like radiation become important [4].

In this Chapter we discuss another simplification, namely the dipolar approximation leading to a coupled-dipole model [5]. In optics, point-dipole methods are an approximation toolbox as powerful as lumped circuits are in the electrostatic regime [2]. It is its electrodynamic nature that makes a point-dipole model superior to lumped-element descriptions of photonic circuits at optical frequencies [6–8].

The dipolar approximation is a good description of a scatterer if the currents oscillating at frequency ω and thereby generating the fields are constrained to a volume $d^3 \ll \lambda^3$, where $\lambda = 2\pi c/\omega$. Furthermore, the observer, or any other current distribution (i.e. scatterer), must be sufficiently far away, such that $d \ll r$, with r being the distance between the observer and the current generating the field [2]. The dipolar approximation lends itself to describing scattering by small particles and assemblies of small particles. Importantly, the size of the assembly can very well be much larger than λ. For scattering by larger particles we refer to Reference [9].

We point out that this Chapter is not intended as a new scientific result but rather as an introduction and a reference in order to aid the unfamiliar reader in following the theoretical formalism applied throughout the remainder of this thesis. Regarding the origin of this Chapter's content we point at the quoted literature. We consider References [10, 11] and [5] together with [2] to be an ideal starting point for a practical application of the coupled-dipole model.

4.2 The dipolar approximation

Assume we have a known spatial current distribution $\boldsymbol{J}(\boldsymbol{r}', t) = \boldsymbol{J}(\boldsymbol{r}')\exp[-\mathrm{i}\omega t]$ in vacuum with a harmonic time dependence and we would like to know the electric field $\boldsymbol{E}$ generated by $\boldsymbol{J}$ at position $\boldsymbol{r}$. The vector potential $\boldsymbol{A}(\boldsymbol{r}, t) = \boldsymbol{A}(\boldsymbol{r})\exp[-\mathrm{i}\omega t]$ is then given by [1]

$$\boldsymbol{A}(\boldsymbol{r}) = \mu_0 \int_V \boldsymbol{J}(\boldsymbol{r}') \frac{\exp\left[\mathrm{i}k\left|\boldsymbol{r}-\boldsymbol{r}'\right|\right]}{4\pi\left|\boldsymbol{r}-\boldsymbol{r}'\right|} \mathrm{d}^3 r' \tag{4.1}$$

from which assuming the Lorentz gauge the electric field follows as

$$\boldsymbol{E}(\boldsymbol{r}) = \mathrm{i}\omega \left[1 + \frac{1}{k^2}\nabla\nabla\cdot\right] \boldsymbol{A}(\boldsymbol{r}), \tag{4.2}$$

where $k = n\frac{\omega}{c}$ is the wave-number in the medium.

When we consider the case where the current distribution is confined to a region much smaller than the wavelength and the observation point is far away from the source region we can immediately simplify Eq. (4.1) to read

$$\boldsymbol{A}(\boldsymbol{r}) = \mu_0 \frac{\exp[\mathrm{i}kr]}{4\pi r} \int_V \boldsymbol{J}(\boldsymbol{r}')\mathrm{d}^3 r'. \tag{4.3}$$

Performing an integration by parts and introducing the electric dipole moment

$$\boldsymbol{p} = \int_V \boldsymbol{r}' \rho(\boldsymbol{r}') \mathrm{d}^3 r' \tag{4.4}$$

the vector potential can be rewritten as

$$\boldsymbol{A}(\boldsymbol{r}) = -\mathrm{i}\omega\mu_0 \frac{\exp[\mathrm{i}kr]}{4\pi r} \boldsymbol{p}. \tag{4.5}$$

This equation constitutes the remarkable and highly useful fact that the fields generated by *any* current distribution within a volume much smaller than λ^3, observed at sufficient distance, are entirely given by the electric dipole moment of the current distribution. This observation justifies the approximation of scatterers with complex geometries by simple point dipoles as long as the scatterers are small compared to the wavelength. Importantly, the dipolar approximation describes the near fields correctly, such that the observer can go as close as desired compared to the wavelength, as long as he is still sufficiently far away measured against the spatial extent of the current distribution.

4.3 The coupled-dipole model

Restricting the discussion to dipolar interactions simplifies things tremendously. From here on, we only consider the fields generated by dipolar currents. In a homogeneous medium of refractive index n the electric field generated at position $\boldsymbol{r}_1$ by a dipole $\boldsymbol{p}$ at $\boldsymbol{r}_0$ is given by [1]

$$\boldsymbol{E}^0(\boldsymbol{p}, n, \omega, \boldsymbol{r}_1, \boldsymbol{r}_0) = \frac{\omega^2\mu_0}{4\pi r} \exp[\mathrm{i}kr] \left\{ (\hat{\boldsymbol{r}} \times \boldsymbol{p}) \times \hat{\boldsymbol{r}} + [3\hat{\boldsymbol{r}}(\hat{\boldsymbol{r}} \cdot \boldsymbol{p}) - \boldsymbol{p}] \left(\frac{1}{(kr)^2} - \frac{\mathrm{i}}{kr} \right) \right\}, \tag{4.6}$$

where $k = n\frac{\omega}{c}$ is the wavenumber in the medium of refractive index $n = \sqrt{\epsilon}$, $r = |\boldsymbol{r}_1 - \boldsymbol{r}_0|$ and $\hat{\boldsymbol{r}} = (\boldsymbol{r}_1 - \boldsymbol{r}_0)/r$.* We can generalize Eq. (4.6) to any dipolar orientation and strength $\boldsymbol{p}$ by introducing the Green function for a homogeneous medium

$$\boldsymbol{G}^0(n, \omega, \boldsymbol{r}_1, \boldsymbol{r}_0) = \left[\boldsymbol{E}(\mathbf{e}_x, n, \omega, \boldsymbol{r}_1, \boldsymbol{r}_0), \boldsymbol{E}(\mathbf{e}_y, n, \omega, \boldsymbol{r}_1, \boldsymbol{r}_0), \boldsymbol{E}(\mathbf{e}_z, n, \omega, \boldsymbol{r}_1, \boldsymbol{r}_0) \right] \tag{4.7}$$

such that

$$\boldsymbol{E}(\boldsymbol{p}, n, \omega, \boldsymbol{r}_1, \boldsymbol{r}_0) = \boldsymbol{G}(n, \omega, \boldsymbol{r}_1, \boldsymbol{r}_0) \cdot \boldsymbol{p}. \tag{4.8}$$

We have dropped the superscript in Eq. (4.8) since it can be taken as the definition of the dipolar Green function for *any* environment. Note that both dipole moments and electric fields are column vectors and the Green function is a 3×3 dyadic. It is important to keep in mind that Eq. (4.6) is the field generated by a dipole in a homogeneous medium and the field generated in another more complex environment is much more complicated. One typically separates the Green function of a complex background

*In general the refractive index $n = \sqrt{\epsilon\mu}$ depends both on the relative permittivity and permeability of the medium. Since in this thesis we are only dealing with non-magnetic materials we always assume $\mu = 1$.

system $\boldsymbol{G}_\mathrm{B} = \boldsymbol{G}^0 + \boldsymbol{G}^s$ into a sum of the free-space Green function $\boldsymbol{G}^0$ and a scattered part $\boldsymbol{G}^s$. Only for a few examples analytical solutions for $\boldsymbol{G}^s$ are known. In particular, we refer to the book by Tai [12], who calculates the Green function for a sphere, a planar interface, and an infinite cylinder of circular cross-section. Furthermore, dyadic Green functions for stratified multi-layers [2, 13], concentric spherical multi-layers [14], an eccentric spherical inclusion in a sphere [15], clusters of spheres [16] and concentric cylindrical multi-layers [17] are available but challenging to handle.

Besides the fields generated by a dipolar source, we are furthermore interested in the response of a polarizable scatterer to an incident electric field, which is in the linear approximation given by the polarizability tensor $\boldsymbol{\alpha}$, such that

$$\boldsymbol{p} = \boldsymbol{\alpha} \cdot \boldsymbol{E}. \tag{4.9}$$

Equations (4.7) and (4.9) are the ingredients necessary to set up the equations of motion for a system of N coupled dipoles. The scatterers $1,\ldots,N$ acquire dipole moments $\boldsymbol{p}_1,\ldots,\boldsymbol{p}_N$ in proportion to their polarizabilities $\boldsymbol{\alpha}_1,\ldots,\boldsymbol{\alpha}_N$ and the electric fields $\boldsymbol{E}(\boldsymbol{r}_1),\ldots,\boldsymbol{E}(\boldsymbol{r}_N)$ at their locations $\boldsymbol{r}_n$, according to the linear self-consistent set of equations [5, 10, 11]

$$\boldsymbol{p}_n = \boldsymbol{\alpha}_n \left[\boldsymbol{E}_\mathrm{in}(\boldsymbol{r}_n) + \sum_{m \neq n} \boldsymbol{G}_\mathrm{B}(\boldsymbol{r}_n, \boldsymbol{r}_m) \cdot \boldsymbol{p}_m \right], \tag{4.10}$$

where we have just rewritten Eq. (4.9) for dipole n by expressing the electric field it experiences as a superposition of the external driving field $\boldsymbol{E}_\mathrm{in}$ and the fields generated by all other polarizable particles due to the fact that they are polarized as well. By moving all dipole moments to the left of the equality sign we can now cast Eq. (4.10) in matrix form to read

$$\mathscr{P} = \boldsymbol{M}^{-1} \cdot \mathscr{E} \tag{4.11}$$

where we have concatenated the dipole moments $\boldsymbol{p}_i$ to the $3N$ component 'super-vector' for polarization $\mathscr{P}$. Equivalently $\mathscr{E}$ describes the incident field components at the particle positions, and the coupling matrix $\boldsymbol{M}$ is defined as

$$\boldsymbol{M}_{i,j} = \delta_{i,j} \boldsymbol{\alpha}_i^{-1} - (1 - \delta_{i,j}) \boldsymbol{G}_\mathrm{B}(\boldsymbol{r}_i, \boldsymbol{r}_j). \tag{4.12}$$

Note that $\boldsymbol{M}$ is of dimension $3N \times 3N$ and the sub-matrices $\boldsymbol{M}_{i,j}$ defined in Eq. (4.12) have dimension 3×3. For a scatterer with its main axes along the coordinate axes the diagonal of $\boldsymbol{M}$ holds the inverse of the polarizability tensor $\boldsymbol{\alpha}_i$ while the off-diagonal elements are given by the Green function coupling terms $\boldsymbol{G}_\mathrm{B}(\boldsymbol{r}_i, \boldsymbol{r}_j)$.

Just like Eq. (4.9) relates the dipole moment of a single scatterer to the incident electric field, Eq. (4.11) relates the polarization state of an ensemble of scatterers to the driving field, where the inverse of the coupling matrix plays the role of a polarizability tensor for the ensemble. It is instructive to take the analogy between $\boldsymbol{\alpha}$ and $\boldsymbol{M}$ even a step further by considering the procedure of diagonalization. When we consider an anisotropic particle of a conventional material we can always diagonalize its polarizability tensor. The associated coordinate transformation leads us to the

principal axes of the polarization ellipsoid, which just means that a driving field along a principal axis will never lead to a polarization of the particle in a direction orthogonal to the chosen principal axis. Equivalently, for an ensemble of particles diagonalization of the inverse coupling matrix $\boldsymbol{M}^{-1}$ leads to the 'eigen-polarizations' and 'eigen-polarizabilities' [18]. The eigen-vectors of $\boldsymbol{M}^{-1}$ can be regarded as the polarization eigen-modes of the system. We will encounter an example of a system with very peculiar polarization eigen-states in Chapter 5.

4.4 The electrodynamic polarizability

The previous section discussed the mathematical formulation and the physical meaning of the coupling matrix of a system of coupled dipoles. While we have identified the off-diagonal elements of the coupling matrix as the fields generated by the scatterers we will now search an expression for the polarizability tensor $\boldsymbol{\alpha}$ which enters the diagonal of the coupling matrix. For a truly didactic treatment of the radiation reaction discussed in the following we strongly recommend the review by Lagendijk and van Tiggelen [19].

A good starting point to find the dipole moment acquired by a spherical particle of a material described by a dielectric constant ϵ_{part} embedded in a homogeneous medium with dielectric constant ϵ_{med} when exposed to an electric field is to solve the electrostatic problem. We restrict ourself to spherical particles of an isotropic material. This approach leads to the electrostatic polarizability [9]

$$\alpha_0 = 4\pi\epsilon_0 V \frac{\epsilon_{\text{part}} - \epsilon_{\text{med}}}{\epsilon_{\text{part}} + 2\epsilon_{\text{med}}}. \tag{4.13}$$

It is now tempting to insert tabulated experimental values for $\epsilon(\omega)$ into Eq. (4.13) in order to obtain a polarizability at frequencies $\omega > 0$. Nevertheless, the obtained polarizability will remain 'electrostatic', as we will show in a moment. For certain classes of materials analytical expressions for $\epsilon(\omega)$ are known, for example a Drude metal is well described by [20]

$$\epsilon(\omega) = 1 - \frac{\omega_{\text{p}}^2}{\omega(\omega - \mathrm{i}\gamma\omega)}, \tag{4.14}$$

where ω_{p} is the plasma frequency and γ the Ohmic damping rate characterizing the material. Upon inserting Eq. (4.14) into Eq. (4.13) and for simplicity assuming the particle to be in air, we arrive at

$$\alpha_0(\omega) = 4\pi\epsilon_0 V \frac{\omega_0^2}{\omega_0^2 - \omega^2 - \mathrm{i}\gamma\omega} \tag{4.15}$$

which resembles the familiar Lorentzian line shape as the generic frequency response of any linear system with resonance frequency $\omega_0 = \omega_{\text{p}}/\sqrt{3}$. The Ohmic damping rate γ of the Drude model sets the damping of the obtained polarizability. Even though Eq. (4.15)

clearly has a frequency dependence, we still refer to it as the electrostatic polarizability, as indicated by the subscript. The reason is that having inserted a frequency dependent dielectric constant into the electrostatic polarizability Eq. (4.13) by no means ensures that the resulting expression Eq. (4.15) is physically valid. In fact, it turns out that Eq. (4.15) violates energy conservation. Accelerated charges radiate electromagnetic energy according to Larmor's formula [1] and so does any polarizable scatterer [21]. This scattering *must* show up as a loss rate in the polarizability of Eq. (4.15), which so far only contains the Ohmic damping.

We find the missing damping term by exploiting the insight that the energy loss of a scatterer equals the work done on its own current by its own electric field [2]. The apparent damping 'force' acting on the current is called Abraham-Lorentz force and has been a matter of strong debate [1, 2]. With the realization that an oscillating dipole is actually subjected to its own electric field we can rewrite Eq. (4.9) as

$$\boldsymbol{p} = \boldsymbol{\alpha}_0 \boldsymbol{E}_{\text{total}} = \boldsymbol{\alpha}_0 \left[\boldsymbol{E}_{\text{ext}} + \boldsymbol{G}_{\text{B}}(\boldsymbol{r}_0, \boldsymbol{r}_0)\boldsymbol{p} \right], \tag{4.16}$$

where we have included the field generated by the dipole moment $\boldsymbol{p}$ at its own position via the Green function. After rearranging the terms to the form $\boldsymbol{p} = \boldsymbol{\alpha}\boldsymbol{E}_{\text{ext}}$ we find the electrodynamic polarizability

$$\boldsymbol{\alpha} = \left[\boldsymbol{\alpha}_0^{-1} - \boldsymbol{G}_{\text{B}}(\boldsymbol{r}_0, \boldsymbol{r}_0) \right]^{-1}, \tag{4.17}$$

which has an additional correction term $\boldsymbol{G}_{\text{B}}(\boldsymbol{r}_0, \boldsymbol{r}_0)$ describing the back-action of the scatterer on itself. Equation (4.17) is the scattering matrix, often referred to as t-matrix, of a single dipolar point scatterer and its expansion yields the Born series of multiple scattering [22]. Importantly, even a *single* scatterer gives rise to a *multiple* scattering series. Remarkably, with the corrected polarizability in Eq. (4.17) we have found a description of the multiple scattering problem with only a first-order scattering term. The real part $\text{Re}\,\boldsymbol{G}$ gives rise to a shift of the resonance frequency of $\boldsymbol{\alpha}$ while the imaginary part $\text{Im}\,\boldsymbol{G}$ is an additional damping term. Equation (4.17) immediately confronts us with a dramatic problem when evaluating the free-space Green-function $\boldsymbol{G}^0(\boldsymbol{r}, \boldsymbol{r})$ at the origin, since Eq. (4.6) diverges for $r = 0$. From Eqs. (4.2) and (4.5) we can read off the scalar free-space Green function [2]

$$G^0 = \frac{\omega^2 \mu_0}{4\pi r} \exp[\mathrm{i}kr], \tag{4.18}$$

which can readily be split into its real and imaginary part using Euler's formula. The real part of Eq. (4.18) indeed diverges and seems to render Eq. (4.17) useless. The problem of this divergence comes about from describing our scatterer as a true mathematical point, which we now have to approach infinitely closely. Clearly, there must be a cut-off which is sensibly chosen such that the resulting resonance frequency appears where it is experimentally found [19].

Carrying out a Taylor expansion in orders of kr before performing the spatial derivatives in order to return to the vector Green function yields for the imaginary part

of the free-space Green function

$$\operatorname{Im} \boldsymbol{G}^0(\boldsymbol{r}_0, \boldsymbol{r}_0) = \frac{\omega^3 n}{6\pi\epsilon_0 c^3} \mathbb{1}. \tag{4.19}$$

The imaginary part of the Green function evaluated at the origin is therefore the damping term that *has* to be included in any polarizability tensor in order to appropriately take radiation loss into account and ensure energy conservation. A complex photonic system with a scattered part of the Green function $\boldsymbol{G}^s$ changes the damping experienced by the scatterer via its imaginary part $\operatorname{Im} \boldsymbol{G}^s$, which enhances or reduces the free space damping $\operatorname{Im} \boldsymbol{G}^0$. This is the Purcell effect changing the radiative line-width of a *scatterer*. The real part $\operatorname{Re} \boldsymbol{G}^s$ shifts the resonance frequency of the scatterer. Thanks to the tensorial nature of $\boldsymbol{G}$ the polarizability of an isotropic scatterer can acquire an anisotropy due to its environment entering in the correction according to Eq. (4.17).

A straightforward recipe to include radiation damping and obtain a bona-fide electrodynamic polarizability $\boldsymbol{\alpha}$ in a homogeneous medium of refractive index n for any chosen electrostatic $\boldsymbol{\alpha}_0$ is therefore [11, 23]

$$\boldsymbol{\alpha}^{-1} = \boldsymbol{\alpha}_0^{-1} - \mathrm{i} \frac{1}{6\pi\epsilon_0} \frac{\omega^3}{c^3} n \mathbb{1}. \tag{4.20}$$

For spheres, the correction in Eq. (4.20) is sometimes amended by a further depolarization factor [24], which leads to a line-shift to the red with increasing particle size but is not strictly necessary to conserve energy.

4.5 Observables and the optical theorem

With the coupled-dipole model we have outlined a consistent electrodynamic framework to describe scattering. In the present section we derive observables that are experimentally accessible. By purely energetic considerations we will arrive at expressions for the extinction and scattering cross-sections of a single dipolar scatterer in a homogeneous medium as well as an expression for the optical theorem for a single dipolar scatterer in any environment.

We consider a single dipolar current source $\boldsymbol{j} = \dot{\boldsymbol{p}} = \boldsymbol{j}_0 \exp[-\mathrm{i}\omega t]\, \delta(\boldsymbol{r} - \boldsymbol{r}_0)$ located at $\boldsymbol{r}_0$. For the moment we do not worry about how this current is generated. We apply the time-averaged form of Poynting's theorem to consider the flux of energy through an arbitrary surface ∂V enclosing only our dipolar current and no lossy material. Poynting's theorem relates the time-averaged flux of electromagnetic energy described by the Poynting vector $\langle \boldsymbol{S} \rangle = \frac{1}{2} \operatorname{Re} \left\{ \boldsymbol{E} \times \boldsymbol{H}^* \right\}$ through the chosen surface to the fields and currents within the enclosed volume via [2]

$$\int_{\partial V} \langle \boldsymbol{S} \rangle \, \mathrm{d}\boldsymbol{A} = -\frac{1}{2} \int_V \operatorname{Re} \left\{ \boldsymbol{j}^\dagger \boldsymbol{E} \right\} \mathrm{d}V, \tag{4.21}$$

where $(\cdot)^\dagger$ denotes the Hermitian conjugate and we imply usual matrix multiplication. Expressing the fields generated by our dipole $\boldsymbol{p}$ via the Green function of the embedding system we arrive at the power emitted by our source into the (possibly lossy)

environment

$$P_{\mathrm{em}} = \frac{1}{2}\omega \boldsymbol{p}^{\dagger} \mathrm{Im}\left[\boldsymbol{G}(\boldsymbol{r}_0, \boldsymbol{r}_0)\right] \boldsymbol{p}. \tag{4.22}$$

In the special case of a homogeneous lossless medium of refractive index n, Eq. (4.22) turns into the familiar form of Larmor's formula $P = \frac{\omega^4 n}{12\pi\epsilon_0 c^3} |\boldsymbol{p}|^2$ for the radiated power of a dipole in a homogeneous medium upon inserting $\mathrm{Im}\,\boldsymbol{G}^0$ from Eq. (4.19). Note that in the case of an environment including lossy constituents Eq. (4.22) describes the sum of the power radiated into the continuum and the power absorbed by the environment, provided you can draw a closed surface around the source *without* enclosing any lossy material.

So far, we have not specified what creates the dipole moment $\boldsymbol{p}$. While Eq. (4.22) holds for *any* environment, in order to derive the scattering and absorption cross-section of a single particle we now consider the case of a single isotropic scatterer with polarizability α in a homogeneous lossless medium driven by a plane wave $\boldsymbol{E}_{\mathrm{in}}$. We insert $\boldsymbol{p} = \alpha \boldsymbol{E}$ into Eq. (4.22) to calculate the power scattered by the particle and remember that the time-averaged Poynting vector along the propagation direction $\langle S \rangle = \frac{1}{2}\sqrt{\frac{\epsilon_0}{\mu_0}} n |\boldsymbol{E}|^2$ gives the incoming power. By dividing the scattered power by the incoming power flux density we obtain the scattering cross-section

$$\sigma_{\mathrm{scat}} = \frac{\omega^4}{6\pi\epsilon_0^2 c^4} |\alpha|^2 . \tag{4.23}$$

For a weak scatterer, i.e. far away from any resonance in α, the wavelength dependence shows the famous λ^{-4} behavior of Rayleigh scattering, which is one main reason why the sky appears blue. This dependence can be obtained from a simple dimensional analysis [25]. Importantly, we have arrived at the scattered power by considering the work that is done on the dipole moment by its *own* field. In contrast, the energy removed by the scatterer from the incoming beam must equal the work that is done on the dipole moment by the *incoming* field. The cycle averaged extinction is therefore [10]

$$P_{\mathrm{ext}} = \langle \mathrm{Re}\, \boldsymbol{E}_{\mathrm{in}} \cdot \mathrm{Re}\, \boldsymbol{j} \rangle = \frac{1}{2}\omega \mathrm{Im}\,(\boldsymbol{E}_{\mathrm{in}}^{\dagger} \boldsymbol{p}), \tag{4.24}$$

which leads to the extinction cross-section of a dipolar scatterer in a homogeneous medium

$$\sigma_{\mathrm{ext}} = \frac{\omega}{\epsilon_0 c n} \mathrm{Im}\,\alpha. \tag{4.25}$$

We note after comparing Eqs. (4.23) and (4.25) that since $\alpha \propto V$ the ratio of scattered to extinct power, commonly referred to as the albedo [19], vanishes for small volumes, such that small particles practically only absorb.

Importantly, in any environment described by $\boldsymbol{G}$, energy conservation requires that the scattered power Eq. (4.22) can never exceed the extinct power Eq. (4.24), such that

$$\boldsymbol{\alpha}^{\dagger} \mathrm{Im}\, \boldsymbol{G} \boldsymbol{\alpha} \leq \frac{1}{2\mathrm{i}} \left(\boldsymbol{\alpha} - \boldsymbol{\alpha}^{\dagger} \right). \tag{4.26}$$

The relation Eq. (4.26) is a general form of the optical theorem that restricts the polarizability $\boldsymbol{\alpha}$ to conserve energy [26]. In the special case of a lossless and homogeneous medium with refractive index n and an isotropic scatterer with polarizability α Eq. (4.26) reduces to [27]

$$\frac{n\omega^3}{6\pi\epsilon_0 c^3}|\alpha|^2 \leq \operatorname{Im}\alpha. \tag{4.27}$$

The correction of the polarizability given in Eq. (4.20) makes sure that the optical theorem Eq. (4.27) is obeyed and energy is conserved. The equality sign in Eqs. (4.26) and (4.27) holds for the case of any hypothetical scatterer without material loss, i.e. $\gamma = 0$, on resonance. More importantly for practical cases, the radiation damping term entering the denominator of the expression for the polarizability according to Eq. (4.17) scales with the particle volume, such that for large scatterers the radiation damping will exceed the material damping. The line-width of the polarizability of plasmonic particles larger than about 40 nm in diameter is typically dominated by radiation losses [28].

Importantly, the electromagnetic environment entering Eq. (4.26) via the Green function $\boldsymbol{G}$ bounds the scattering strength of any dipole to the *unitary limit*. Let us consider an isotropic scatterer in vacuum, where we can combine Eqs. (4.25) and (4.27) to obtain the maximally possible extinction cross-section of *any* dipolar scatterer $\sigma_{\text{ext}}^{\text{UL}} = \frac{3}{2\pi}\lambda^2$. We will reencounter the unitary limit in the context of assemblies of scatterers in Chapter 5 and its repercussions in a complex environment will be of paramount importance in Chapter 6.

We have just reminded ourself how to calculate the extinction and scattering cross-sections of single particles. The value and success of the coupled-dipole model relies on the fact that it allows to calculate extinction, scattering, and absorption cross-sections of clusters of particles, as well as eigen-modes and radiation patterns, also for clusters of particles [5, 10, 11, 18, 29]. As we will illustrate in the next section, also the LDOS is easily available in a coupled-dipole approach. The coupled-dipole formalism has recently been extended to magneto-electric scatterers [27]. The typical procedure to obtain any observable is to first specify the particle positions and their electrodynamic polarizabilities. At this point the coupling matrix $\boldsymbol{M}$, given in Eq. (4.12), is fully defined and has to be inverted. To find the dipole moments for any driving field remains a simple matrix multiplication according to Eq. (4.11). With the knowledge of the dipole moments resulting from a specific driving field all desired observables can be derived. For example, the extinction cross-section of a particle cluster is obtained from choosing a plane wave as a driving field and summing the power dissipated by that driving field by acting on the resulting individual dipole moments according to Eq. (4.24). To obtain the scattering cross-section of a particle cluster we calculate the Poynting vector of the fields generated by the individual dipole moments through a hypothetical sphere. This procedure can be carried out with limited computational effort by choosing the sphere sufficiently large and applying a far-field approximation for the dipole radiation. With the same recipe we can naturally also calculate differential scattering cross-sections and thereby radiation patterns of particle clusters.

Regarding the driving field, we are of course not limited to plane waves. Most interesting for the purpose of this thesis is certainly to choose a dipolar point source to

drive an ensemble of scatterers to model the field emitted by a dipolar source in the vicinity of a cluster of scatterers. The dipole field generated by that point source, given in Eq. (4.6), then enters Eq. (4.11) as the driving field and the total radiated field is the superposition of the driving field and the fields generated by the induced dipole moments of the scatterers calculated according to Eq. (4.11).

4.6 Spontaneous-emission rate enhancement

Most interesting for the purpose of this thesis is to calculate the LDOS at a particular position with respect to an ensemble of point scatterers. Xu, Lee, and Yariv [30] have shown that the spontaneous-emission rate of a quantum-mechanical two-level system with transition frequency ω is proportional to the power dissipated by a constant-current source of the same frequency [2]. We can therefore calculate the spontaneous-emission rate *enhancement* via the enhancement in power dissipated by a classical constant-current source in the complex photonic environment as compared to a reference system. To this end, we revert to the expression for the power dissipated by an oscillating dipole in Eq. (4.24), under the assumption that $\mathrm{Im}\,\boldsymbol{G}$ does not significantly change across the natural line-width of the quantum emitter [30, 31]. Upon splitting the Green function into its free and scattered parts the decay-rate enhancement with respect to vacuum is given by

$$A = 1 + \frac{\boldsymbol{p}^\dagger \mathrm{Im}\,\boldsymbol{G}^{\mathrm{s}}(\boldsymbol{r}_0, \boldsymbol{r}_0)\boldsymbol{p}}{\boldsymbol{p}^\dagger \mathrm{Im}\,\boldsymbol{G}^{\mathrm{vac}}(\boldsymbol{r}_0, \boldsymbol{r}_0)\boldsymbol{p}}. \tag{4.28}$$

From Eq. (4.28) we can immediately appreciate that the rate enhancement (or suppression) of a spontaneous emitter in a complex photonic system is a result of the radiation reaction of the emitter's own field scattered by the environment and returning with a phase shift to perform work on the source, thereby increasing (or decreasing) the resistance of the vacuum. This picture merits the interpretation of the LDOS as an impedance experienced by a quantum emitter [32, 33]. Importantly, Eq. (4.28) allows to calculate the decay-rate enhancement, and therefore the LDOS, in any photonic environment whose Green function is known, despite that system possibly exhibiting material losses, which renders literal counting of the states impossible [34, 35]. The strength of Eq. (4.28) is that it allows to determine the LDOS by evaluating $\mathrm{Im}\,\boldsymbol{G}$ only at a single point, namely the origin. It however hides the different contributions to the LDOS since the dissipated power calculated according to Eq. (4.28) contains all contributions to the LDOS, both radiative and non-radiative, due to the environment. If we desire to separate the rate enhancement due to radiative decay enhancement we will have to integrate the radiated power in the far field.

Finally, we would like to point out that the community of spontaneous-emission control, including ourself, handles the term LDOS rather sloppily. LDOS is used to refer to the energy and volume density of states, but also to the imaginary part of the Green function $\mathrm{Im}\,\boldsymbol{G}(\boldsymbol{r}, \boldsymbol{r})$, its component projected on a certain dipole orientation $\hat{\boldsymbol{p}}^\dagger \mathrm{Im}\,\boldsymbol{G}^{\mathrm{vac}}(\boldsymbol{r}_0, \boldsymbol{r}_0)\hat{\boldsymbol{p}}$, its trace $\mathrm{tr}\{\mathrm{Im}\,\boldsymbol{G}\}$ or any of these quantities normalized to the corresponding value in vacuum. Typically, no confusion arises from the context.

References

[1] J. D. Jackson, *Classical Electrodynamics*, Wiley, New York, 1999.

[2] L. Novotny and B. Hecht, *Principles of Nano-Optics*, Cambridge University Press, Cambridge, 2006.

[3] P. Horowitz and W. Hill, *The Art of Electronics*, Cambridge University Press, Cambridge, 1989.

[4] C. A. Balanis, *Antenna Theory: Analysis and Design, 3rd Edition*, John Wiley and Sons, New Jersey, 2005.

[5] F. J. García de Abajo, *Colloquium : Light scattering by particle and hole arrays*, Rev. Mod. Phys. **79**, 1267 (2007).

[6] N. Engheta, A. Salandrino, and A. Alù, *Circuit elements at optical frequencies: Nanoinductors, nanocapacitors, and nanoresistors*, Phys. Rev. Lett. **95**, 095504 (2005).

[7] N. Engheta, *Circuits with light at nanoscales: Optical nanocircuits inspired by metamaterials*, Science **317**, 1698 (2007).

[8] A. Alù and N. Engheta, *Input impedance, nanocircuit loading, and radiation tuning of optical nanoantennas*, Phys. Rev. Lett. **101**, 043901 (2008).

[9] C. F. Bohren and D. R. Huffman, *Absorption and Scattering of Light by Small Particles*, John Wiley and Sons, New York, 1983.

[10] L. Zhao, K. L. Kelly, and G. C. Schatz, *The extinction spectra of silver nanoparticle arrays: Influence of array structure on plasmon resonance wavelength and width*, J. Phys. Chem. B **107**, 7343 (2003).

[11] W. H. Weber and G. W. Ford, *Propagation of optical excitations by dipolar interactions in metal nanoparticle chains*, Phys. Rev. B **70**, 125429 (2004).

[12] C.-T. Tai, *Dyadic Green Functions in Electromagnetic Theory*, IEEE Press, 1994.

[13] M. Paulus, P. Gay-Balmaz, and O. J. F. Martin, *Accurate and efficient computation of the Green's tensor for stratified media*, Phys. Rev. E **62**, 5797 (2000).

[14] L.-W. Li, P.-S. Kooi, M.-S. Leong, and T.-S. Yee, *Electromagnetic dyadic Green's function in spherically multilayered media*, IEEE Trans. Microw. Theory Tech. **42**, 2302 (1994).

[15] A. P. Moneda and D. P. Chrissoulidis, *Dyadic Green's function of a sphere with an eccentric spherical inclusion*, J. Opt. Soc. Am. A **24**, 1695 (2007).

[16] A. P. Moneda and D. P. Chrissoulidis, *Dyadic Green's function of a cluster of spheres*, J. Opt. Soc. Am. A **24**, 3437 (2007).

[17] Z. Xiang and Y. Lu, *Electromagnetic dyadic Green's function in cylindrically multilayered media*, IEEE Trans. Microw. Theory Tech. **44**, 614 (1996).

[18] V. A. Markel, *Antisymmetrical optical states*, J. Opt. Soc. Am. B **12**, 1783 (1995).

[19] A. Lagendijk and B. A. van Tiggelen, *Resonant multiple scattering of light*, Phys. Rep. **270**, 143 (1996).
[20] C. Kittel, *Introduction to Solid State Physics*, Wiley, 2005.
[21] L. Allen and J. H. Eberly, *Optical Resonance and Two-Level Atoms*, Dover Books on Physics, 1987.
[22] M. B. van der Mark, M. P. van Albada, and A. Lagendijk, *Light scattering in strongly scattering media: Multiple scattering and weak localization*, Phys. Rev. B **37**, 3575 (1988).
[23] K. L. Kelly, E. Coronado, L. L. Zhao, and G. C. Schatz, *The optical properties of metal nanoparticles: The influence of size, shape, and dielectric environment*, J. Phys. Chem. B **107**, 668 (2003).
[24] A. Wokaun, J. P. Gordon, and P. F. Liao, *Radiation damping in surface-enhanced Raman scattering*, Phys. Rev. Lett. **48**, 957 (1982).
[25] S. John, *Strong localization of photons in certain disordered dielectric superlattices*, Phys. Rev. Lett. **58**, 2486 (1987).
[26] R. G. Newton, *Scattering Theory of Waves and Particles*, Dover Publications, New York, 2002.
[27] I. Sersic, C. Tuambilangana, T. Kampfrath, and A. F. Koenderink, *Magnetoelectric point scattering theory for metamaterial scatterers*, Phys. Rev. B **83**, 245102 (2011).
[28] H. Mertens, A. F. Koenderink, and A. Polman, *Plasmon-enhanced luminescence near noble-metal nanospheres: Comparison of exact theory and an improved Gersten and Nitzan model*, Phys. Rev. B **76**, 115123 (2007).
[29] A. F. Koenderink and A. Polman, *Complex response and polariton-like dispersion splitting in periodic metal nanoparticle chains*, Phys. Rev. B **74**, 033402 (2006).
[30] Y. Xu, R. K. Lee, and A. Yariv, *Quantum analysis and the classical analysis of spontaneous emission in a microcavity*, Phys. Rev. A **61**, 033807 (2000).
[31] P. Kristensen, A. F. Koenderink, P. Lodahl, B. Tromborg, and J. Mørk, *Fractional decay of quantum dots in real photonic crystals*, Opt. Lett. **33**, 1557 (2008).
[32] J.-J. Greffet, M. Laroche, and F. Marquier, *Impedance of a nanoantenna and a single quantum emitter*, Phys. Rev. Lett. **105**, 117701 (2010).
[33] R. G. S. El-Dardiry, S. Faez, and A. Lagendijk, *Classification of light sources and their interaction with active and passive environments*, Phys. Rev. A **83**, 031801 (2011).
[34] R. Sprik, B. A. van Tiggelen, and A. Lagendijk, *Optical emission in periodic dielectrics*, Europhys. Lett. **35**, 265 (1996).
[35] H. P. Urbach and G. L. J. A. Rikken, *Spontaneous emission from a dielectric slab*, Phys. Rev. A **57**, 3913 (1998).

5

Signature of a Fano Resonance in the LDOS of a Plasmonic Heptamer

We present measurements on plasmonic meta-molecules under local excitation using cathodoluminescence which show a spatial redistribution of the local density of optical states at the same frequency where a sharp spectral Fano feature in the extinction cross-section has been observed. Our analytical model shows that both near-field and far-field effects arise due to interference of the same two eigen-modes of the system. We present quantitative insights both in a bare-state, and in a dressed-state picture that describe plasmonic Fano interference either as near-field amplitude transfer between three coupled bare states, or as interference of two uncoupled eigen-modes in the far field. We identify the same eigen-mode causing a dip in extinction to strongly enhance the radiative local density of optical states, making it a promising candidate for spontaneous-emission control.

5.1 Introduction

Interference is ubiquitous in physics. Significant recent advances in optics as well as quantum physics hinge on interference, inherent in the wave nature of light and matter, and the superposition principle. In quantum optics, the Fano effect and its occurrence in electromagnetically induced transparency (EIT) have in particular triggered tremendous interest as phenomena relying on quantum interference [1] in light-matter coupling. In

EIT, a strongly absorbing atomic vapor coupled to an intense pump field acquires a narrow transparency window with unusual features, such as ultralow group velocities and huge nonlinearities. These extraordinary properties have attracted the interest of the field of nanophotonics, the science of engineering the generation, the propagation and the absorption of light on a subwavelength scale [2]. The aspiration of nano-optical circuitry with powerful functionality led to the development of optical metamaterials. These artificial materials are composed of meta-atoms, designed building blocks giving rise to peculiar properties not found in natural materials [3]. Inspired by quantum optics, scientists have identified plasmonic meta-molecules whose optical properties mimic EIT-lineshapes in atomic vapors, an effect termed 'plasmon-induced transparency' (PIT) [4], based on the Fano interference of a super- and a sub-radiant mode. Even without the benefit of a full electrodynamic model reaching beyond brute-force numerical simulations, remarkable intuition and simple electrostatic arguments have led to the development of several structures exhibiting PIT [4–13]. While in PIT plasmonic meta-molecules control the propagation of light by creating narrow dark resonances useful for slow light or sensing, another class of nanostructures termed 'optical antennas' is currently being developed to tailor light-matter interaction [14–16]. Antennas exploit bright resonances to enhance the emission of light. Practically all aspects of spontaneous-emission control by optical antennas rely on designed enhancement of the local density of optical states (LDOS), arguably the most fundamental quantity in nano-optics [2]. An outstanding question is what the LDOS of PIT structures is, and if one can use the narrow dark lines of PIT to improve optical antennas. To answer this question it is essential to unravel which modes are involved in PIT, how they project on localized driving, and how they give rise to our observable, i.e. far-field radiation. To date, the community has relied on the interpretation of symmetry inspired dipole patterns as 'modes' [12] or abstracted 'modes of constituents' [17, 18]. In both pictures, the 'modes' were assumed to be mutually-coupled harmonic oscillators [19], and were used to fit lineshapes of a variety of observables encountered in experiments and numerical simulations [6]. A sensible definition of the uncoupled 'eigen-modes' of a PIT structure as they arise due to the electrodynamic interaction of the constituents has remained elusive.

In this Chapter, we map the LDOS of a plasmonic molecule known to exhibit PIT. Under near-field driving using cathodoluminescence (CL) we observe a marked spatial redistribution of the LDOS occurring at wavelengths coincident with the PIT-dip in extinction, thereby relating far-field data to the near-field LDOS. We present a model that identifies the diagonal 'dressed states' of the meta-molecule and proves the LDOS feature to be due to interference of the same eigen-states that are responsible for PIT in plane-wave extinction. We draw three remarkable conclusions beyond the analogy with atomic EIT. Firstly, we find a 'screening' state that significantly renormalizes the interaction. Secondly, we conclude that all observations can be viewed purely as far-field interference of two eigen-modes of the system. Thirdly and surprisingly, we identify the sub-radiant mode to be a promising candidate to enhance brightness and rate of spontaneous emission into the far field.

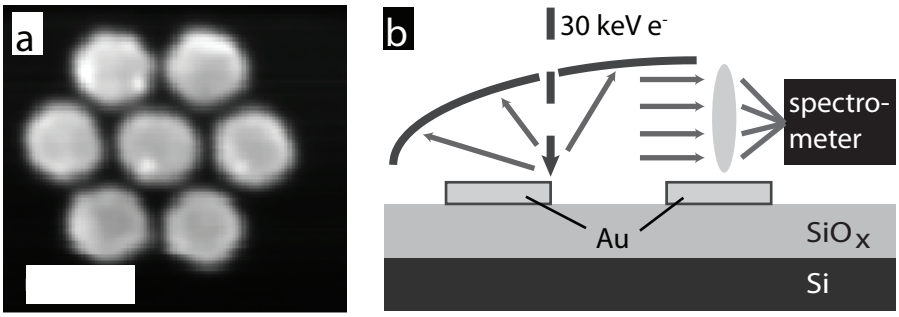

Figure 5.1: (a) SEM micrograph of plasmonic heptamer. Scalebar is 200 nm. (b) Sketch of experimental setup showing sample, impinging electron beam, parabolic mirror and optics guiding cathodoluminescence to a spectrometer.

5.2 Experimental

We fabricated plasmonic Au heptamers by electron-beam lithography, thermal evaporation and lift off [20] on a $1 \times 1\,\mathrm{cm}^2$ Si wafer covered with 1 µm thermal oxide. The bare substrates were cleaned by ultrasonication in water and subsequent immersion in base piranha (H_2O, 30% NH_4OH, 30% H_2O_2, in 5:1:1 ratio) at 75°C for 30 minutes. We pretreat the cleaned samples with HMDS primer prior to spinning ZEP-520a resist (diluted 5:2 in anisole) for 45 s at 3 krpm, which results in a 120 nm resist layer. Substrates are baked for 5 minutes at 180°C and covered with a layer of conductive polymer (Espacer 300Z). The electron-beam lithography is done in a Raith e-line system at an acceleration voltage of 20 keV and with an area dose of $50\,\mu\mathrm{C/cm}^2$. The exposed pattern is developed in N-amyl acetate for 60 s and rinsed in methyl-isobutyl-ketone and iso-propanol. In the following step 35 nm of gold are deposited by physical vapor deposition at 8×10^{-7} mbar at a rate of 0.5 Å/s. Lift-off is performed by immersion of the sample in N-methyl-2-pyrrolidone at 65°C for 4 hours and subsequent rinsing in acetone and iso-propanol.

Each heptamer consists of nominally identical particles arranged on the corners and center of a hexagon. A SEM image of a typical heptamer with particle diameter 150 nm, and gap width 25 nm is shown in Fig. 5.1(a). The CL measurements were performed in a scanning-electron microscope, sketched in Fig. 5.1(b). CL maps are acquired by raster scanning the focused electron beam (30 keV, waist < 5 nm, step-size 10 nm) across the sample. No alteration of samples due to electron-beam irradiation with regards to appearance under SEM or CL imaging was observed. Emitted light collected with a parabolic mirror [acceptance angle 4.6 sr, paraboloid parameter $(10\,\mathrm{mm})^{-1}$] is focused onto a 600 µm-diameter-core multimode fiber using an achromatic lens. The fiber is connected to a spectrometer (PI Acton SP2300i) with a liquid-nitrogen-cooled silicon CCD array (Princeton Instruments, Spec-10 100F/LN). The measured signal hence represents 'CL excitability' as a function of detection wavelength and spatial excitation coordinate. In Fig. 5.2(a) we show CL collected from the heptamer

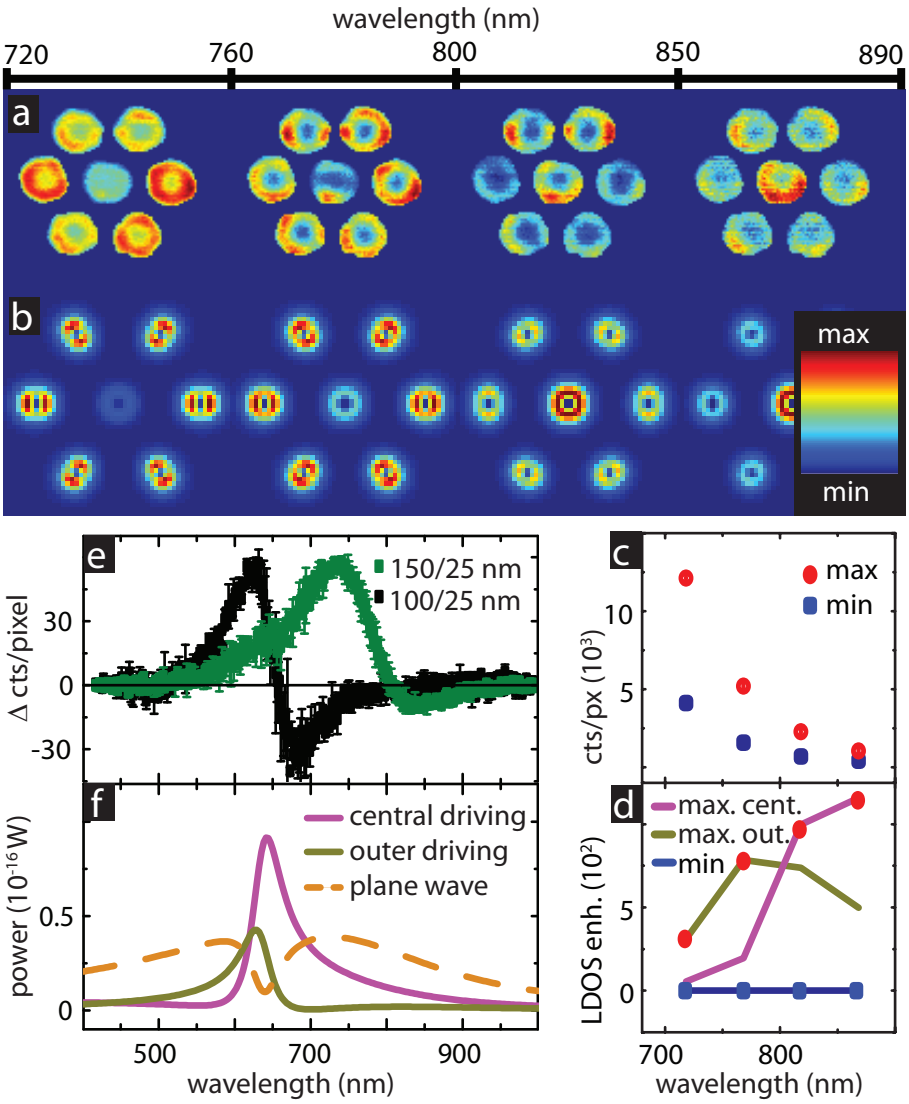

Figure 5.2: (a) Measured CL excitability maps of plasmonic heptamer. (b) Calculated maps of radiative LDOS. Inset: colorbar for (a) and (b). (c) Limits of colorscale for (a). Background around 700 nm stems from oxide substrate. (d) Calculated radiative LDOS enhancement on central (purple) and outer (olive) particles of heptamer with particle diameter/gapwidth 150/25 nm. Blue and red symbols denote colorscale limits of frames in (b). (e) Measured differential-excitability spectra showing intensity difference between outer and central particles. Green (black): Particle diameter/gapwidth 150/25 nm (100/25 nm). Errorbars denote standard deviation of 4 (2) structures. (f) Calculated power radiated by super- and sub-radiant eigen-modes of heptamer upon driving central (purple)/outer (olive)/all (orange dashed) particles with vertical electric field corresponding to black curve in (e) (100/25 nm).

in Fig. 5.1(a) as a series of spatial excitation maps by binning the data into 50 nm wavelength slices. We identified pixels on substrate vs. on Au particles by thresholding the SEM data collected in parallel with the CL. We clamp the color value for all substrate pixels to the smallest value obtained on any Au particle to maximize color contrast for the regions of interest we analyze, i.e. the particles. The minimum and maximum values of the colormaps in Fig. 5.2(a) [colorbar in inset in Fig. 5.2(b)] are plotted in Fig. 5.2(c). While at wavelengths shorter than 800 nm in Fig. 5.2(a) the outer particles appear brighter, i.e., their excitability is higher, the situation is reversed at wavelengths longer than 800 nm, where the inner particle is more excitable. Local hot-spots are due to surface roughness inherent to the fabrication. To quantify the observed swap in local excitability we discriminate pixels belonging to individual particles by thresholding the secondary-electron image taken in parallel with the CL data. We then spatially average the spectra of all pixels belonging to outer particles and do the same for pixels belonging to the inner particle. Subsequently, we subtract the averaged spectra of outer and inner particles from each other. The resulting 'differential excitability' is therefore positive if the outer particles are more excitable than the inner one. This procedure eliminates the broad background fluorescence of the oxide layer around 650 nm, which causes the overall increase in absolute signal towards the blue in Fig. 5.2(c). Figure 5.2(e) shows differential-excitability spectra for heptamers with particle diameter/gap size 150/25(±5) nm averaged over four structures [green squares] and 100/25(±5) nm, averaged over two [black squares]. The wavelength where the differential excitability changes sign, i.e., where excitability swaps from outer to inner particles, appears around 800 nm for the large heptamers, as reported in Fig. 5.2(a), and blue-shifts to 650 nm for smaller particles.

5.3 Electrodynamic model

We model the plasmonic heptamers with the fully electrodynamic coupled-dipole model described in Chapter 4. First, we show that this model captures both the far-field Fano interference, and the excitability swap in our experiment. Subsequently, we derive new insights by identifying the bare and dressed states in analogy to the atomic system. As a reminder, in our model the response of each particle to an electric field, i.e. its dipole moment $\boldsymbol{p} = \boldsymbol{\alpha}\boldsymbol{E}$, is proportional to its Lorentzian polarizability tensor $\boldsymbol{\alpha}$.* The resulting set of coupled linear equations can be written in the form $\mathscr{P} = \boldsymbol{M}^{-1} \cdot \mathscr{E}_{\text{ext}}$, where $\mathscr{E}_{\text{ext}}$ is the incident field driving each particle. Both $\mathscr{E}_{\text{ext}}$ and $\mathscr{P}$ have $3N = 21$ elements for $N = 7$ particles. The interaction matrix $\boldsymbol{M}$ has the inverse of $\boldsymbol{\alpha}$ on the diagonal, while the off-diagonal elements describe the interaction between dipoles as set by the electrodynamic Green function. For any dipole assembly $\boldsymbol{M}$ can be inverted to find the polarization state $\mathscr{P}$ induced by any driving $\mathscr{E}_{\text{ext}}$. Since this linear problem contains full electrodynamic interactions, its solution allows to

*We model the particles as oblate spheroids with short axis 15 nm and long axis 50 nm [75 nm for LDOS maps in Fig. 5.2(b)] in air [21] and extend the static polarizability by a radiation damping term [22]. For ϵ we assume a Drude model ($\omega_0 = 4.76 \cdot 10^{15}$ rad s^{-1}, $\gamma = 8.5 \cdot 10^{13}$ s^{-1}).

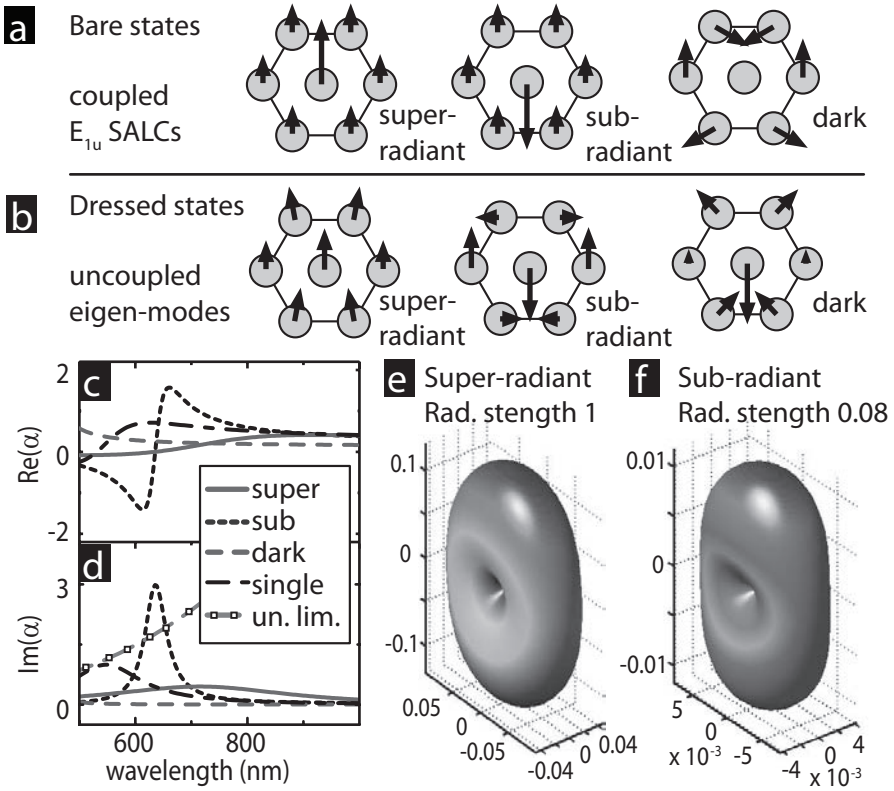

Figure 5.3: (a) Bare-state nondiagonal polarization basis, consisting of a super-radiant, sub-radiant and dark symmetry-adapted linear combination (SALC) of E_{1u} derived from group theory. (b) Dressed-state basis of decoupled super-radiant, sub-radiant and dark eigen-modes (small out-of-phase components not visualized). (c) Real and (d) imaginary parts of polarizabilities of the eigen-modes and a single constituent particle in $10^{-31}\,\mathrm{Cm}^2/\mathrm{V}$. For comparison, in (d) we also plot the unitary limit. (e) and (f) are radiation patterns of super-radiant and sub-radiant eigen-modes in W/sr. Radiative strength indicates total radiated power relative to super-radiant eigen-mode.

calculate any near- and far-field observable. Specifically, the intensity of generated CL, i.e. local excitability, is proportional to the component of the radiative LDOS along the impinging electron beam [23, 24]. In a nutshell, in order to satisfy the boundary conditions when an electron traverses the sample-vacuum interface an electromagnetic field has to be generated [25]. One can therefore think of the electron beam as a broad-band constant-current source in close proximity and perpendicularly oriented to the interface, radiating in proportion to the radiative LDOS at the specific location.

Figure 5.2(b) shows calculated maps of the radiative LDOS for driving perpendicular to and located 40 nm above the plane of the meta-molecule. The limits of the colorbar are indicated in Fig. 5.2(d). As in the experimental data, the ring-shaped

profiles per particle imply that we detect in-plane induced particle polarizations, despite the out-of-plane incident electron beam [26]. The calculations in Fig. 5.2(b) reproduce the measured swapping of LDOS from outer to inner particles experimentally observed in Fig. 5.2(a). Note that the apparent discrepancy of the absolute scaling of experiment and theory in Figs. 5.2(c) and (d) is a result of the substrate-fluorescence background together with the vanishing detector efficiency towards the infrared. Calculated maps similar to those in Fig. 5.2(b) (not shown) for smaller particles confirm the shift of spectral features to shorter wavelengths with decreasing size as experimentally observed in Fig. 5.2(e). As we show below in Fig. 5.5 the Fano dip in extinction [11] calculated using the same model coincides with the spectral position of the excitability swap in CL, pointing at a direct relation between LDOS and Fano interference.

5.4 Symmetry of the heptamer and eigen-modes

While the calculation itself so far provides little insight, the gratifying quantitative confirmation of the Fano extinction dip and the concomitant CL signature suggest to search for deeper insight into the physical mechanisms within our model. As noted in Chapter 4 already, Eq. (4.11) is a generalized form of Eq. (4.9). Diagonalization of the inverse of the coupling matrix $\boldsymbol{M}^{-1}$ will yield its eigen-vectors, which correspond to the polarization eigen-states of the plasmonic heptamer, while the associated eigen-values can be regarded as the eigen-polarizabilities of the structure. Three essential steps simplify the task of diagonalization.

First, the diagonalization of a matrix is the search for a suitable coordinate system, which is determined by the symmetry of the problem. The plasmonic heptamer studied here is a highly symmetric structure and we can apply the group theoretical formalism developed to describe the vibrational excitations of molecules [27]. Mirin *et al.* [28], have already exploited the D_{6h} symmetry of the heptamer in an electrostatic treatment. The correct reducible representation of the heptamer reads [28]

$$\begin{aligned}\Gamma_{\text{heptamer}} = {} & 1A_{1g} + 1A_{2g} + 1B_{2g} + 2E_{2g} + 1E_{1g} \\ & + 2A_{2u} + 1B_{1u} + 1B_{2u} + 1E_{2u} + 3E_{1u}.\end{aligned} \tag{5.1}$$

Therefore, Symmetry-Adapted Linear Combinations (SALCs) of dipole moments [27, 29] cast the electrodynamic coupling matrix $\boldsymbol{M}$ into block diagonal form since group theory naturally extends beyond electrostatic hybridization [30], allowing a symmetry-based decoupling also for calculations of scattering.

Second, since we rely on far-field detection, we focus our attention on the infrared-active E_{1u} irreducible representations, which have finite net-dipole moment. These excitations are dubbed 'IR-active' in spectroscopy terminology and are easily identified in the character table since they transform as the coordinates.[†] Due to the degeneracy of horizontal and vertical polarization in the sixfold symmetry we are left with a

[†]The other IR-active irreducible representation is A_{2u} and belongs to out-of-plane dipole moments, which we disregard, since their resonances are shifted far to the blue due to the oblate particle shape, and furthermore radiation from vertical dipoles is not collected very efficiently by the parabolic mirror.

three-dimensional subspace. While symmetry dictates the subspaces spanned by the respective irreducible representations, it does not favor any particular choice of coordinates within these subspaces. We therefore pick the basis that spans the E_{1u} subspace that prevails in the discussion of PIT [12, 28]. That choice of SALCs (vertical polarization only) is shown in Fig. 5.3(a). Two SALCs are the in-phase and out-of-phase superpositions of one hexamer and the single particle E_{1u} modes pointed out in Reference [28]. In addition to the super-radiant SALC (large net dipole moment) and sub-radiant SALC (threefold smaller dipole moment), symmetry requires a third dark SALC with zero net dipole moment. One obtains the corresponding degenerate SALC basis for the horizontal polarization by simply rotating all dipole moments by 90°.

It is important to realize that the SALC basis is chosen based purely on intuition since no coupling parameters have been considered thus far. Fano resonances in plasmonic heptamers are commonly explained as an interference effect of the super-radiant and sub-radiant SALC in Fig. 5.3 [11, 12, 28] in a mechanical mass-spring model of two coupled harmonic oscillators, of which one is strongly and one is weakly damped [19]. The strongly damped mechanical oscillator is then identified with the super-radiant SALC and the weakly damped oscillator with the sub-radiant SALC. Furthermore, the driving field is assumed to only act on the super-radiant SALC. Indeed, the work done by the driving on the strongly damped oscillator exhibits lineshapes quite similar to extinction lineshapes observed in PIT structures [19]. However, in order to reach beyond a qualitative phenomenological description and unravel the true eigen-modes of the system, the electrodynamic coupling constants governing the interaction between the SALCs need to be taken into account.

The knowledge of the symmetry has allowed us to separate the three dimensional E_{1u} subspace from the 18 other degrees of freedom. Up to this point, however, our treatment is entirely based on symmetry arguments and does not contain any knowledge about either the nature or the strength of the mutual interaction between the dipole moments of the individual particles. Therefore, as a third essential step, we take the coupling constants into account by diagonalizing the E_{1u} sub-matrix of $\boldsymbol{M}$ to find the true decoupled eigen-modes. Remarkably, the three eigen-vectors of E_{1u}, sketched in Fig. 5.3(b), are almost unchanged across the frequency range from 400 to 1000 nm.[‡] The complex eigen-values, in contrast, show strong dispersion, as shown in Fig. 5.3(c,d). These eigen-values are the 'eigen-polarizabilities' of the eigen-modes under which the E_{1u} sub-matrix of $\boldsymbol{M}$ is diagonal and which therefore are by definition decoupled. Considering the dipole distributions in Fig. 5.3(b) we can classify the first eigen-mode as super-radiant, therefore featuring a broad eigen-polarizability [Fig. 5.3(c,d), solid line], reminiscent of the super-radiant SALC in that all dipole moments are approximately aligned [compare Fig. 5.3(a,b)]. The second eigen-mode is sub-radiant with a narrow resonant eigen-polarizability around 630 nm, i.e., at the observed Fano dip and LDOS feature [Fig. 5.3(c,d), dotted line]. Due to the coupling set by $\boldsymbol{M}$, this sub-radiant mode is remarkably different from the sub-radiant SALC. The third eigen-mode, dubbed 'dark', has a narrow resonance at significantly shorter wavelengths, beyond our range of

[‡]The fact that the eigen-vectors are practically constant for all frequencies is not a given. Remember that the coupling matrix $\boldsymbol{M}(\omega)$ is frequency dependent.

interest [long dashed line in Fig. 5.3(c,d)]. Since the dark mode's eigen-polarizability is negligible around 630 nm, the Fano interference is explained in terms of just the super- and sub-radiant modes [solid and dotted lines in Fig. 5.3(c,d)]. In Fig. 5.3(e,f) we plot the radiation patterns of the super- and sub-radiant eigen-modes, which were calculated by evaluating the Poynting vector in the far field with the amplitude of the mode set to unity. The super- and sub-radiant eigen-modes have largely overlapping radiation patterns, although with a twelvefold ratio in integrated radiated intensity at identical amplitude. While the eigen-modes are by definition decoupled, the excellent radiation-pattern overlap implies that nearly completely destructive or constructive interference can occur in the far field.

5.5 Two eigen-modes explain all observations

To demonstrate that two eigen-modes capture all the physics observed both under local and plane-wave driving, we perform calculations using just the super-radiant and sub-radiant eigen-modes. The purple curve in Fig. 5.2(f) shows the power radiated by the heptamer when only the central particle is driven. The total radiated power (proportional to CL intensity generated on the central particle) shows an asymmetric peak at 650 nm with a steep slope on its blue side, and a strongly broadened wing on its red side. The localized driving mainly projects on the resonant sub-radiant mode. The super-radiant mode provides a weak contribution that interferes destructively on the blue, and constructively on the red side of the resonance, leading to the typical asymmetric Fano lineshape. Importantly, when driving the outer particle [olive curve in Fig. 5.2(f)], the peak asymmetry is reversed, as the relative phase between excitation of the broad super-radiant and narrow sub-radiant mode is swapped. This asymmetric broadening in opposite directions underlies the measured dispersive differential excitability in Fig. 5.2(e), and signifies interference of the two decoupled eigen-modes on the detector. When driving the heptamer by a plane wave [Fig. 5.2(f), orange dashed line], we find that the same two modes cause the Fano dip reported in literature [11]. The dark Fano feature in extinction coincides spectrally with the asymmetric CL peaks, i.e. the asymmetric radiative LDOS enhancement, evident in local excitation. In contrast to local excitation, plane-wave driving strongly drives the super-radiant mode, causing the weakly excited sub-radiant eigen-mode to appear as a narrow dip on a high background. We conclude that the measured redistribution of the LDOS in the CL data signifies the same interference mechanism as the Fano dip in extinction, though with very different super-radiant and sub-radiant mode amplitudes.

Most notably, the purple curve in Fig. 5.2(f) illustrates that upon locally driving the central particle the heptamer is a very efficient and bright optical antenna. This enhancement of the radiative LDOS surprisingly results from the efficient excitation of the sub-radiant mode. To quantify the potential of the plasmonic heptamer as an optical antenna we also plot the polarizability of a single constituent particle of the heptamer in Fig. 5.3(c,d) as the dash-dotted line. Clearly, the eigen-polarizability of the sub-radiant eigen-mode exceeds that of the single particle and is narrower in width.

We also plot the unitary limit in Fig. 5.3(d) as the dashed line with squares, which gives the theoretical limit for a single dipolar scatterer's polarizability, as outlined in Section 4.5. Importantly, the eigen-polarizability of the sub-radiant eigen-mode on resonance exceeds the unitary limit by about a factor of two. We therefore draw the counterintuitive conclusion that introducing sub-radiant modes that are usually associated with dark PIT phenomena can actually enhance the capability of optical antennas to create bright and efficient emitters with a large radiative LDOS. The theoretical analysis tool that we have applied to the specific case of a heptamer will be of great value to explore the application of PIT to spontaneous-emission enhancement. Our approach goes beyond both brute-force numerical techniques and electrostatic hybridization and provides a generic, analytical framework that for the first time reveals the true eigen-modes of a structure exhibiting PIT, their polarizability, brightness, and response to any near-field or far-field driving.

5.6 Symmetry breaking and quantum efficiency

Having identified the potential of plasmonic heptamers for radiative LDOS engineering we investigated both experimentally and theoretically the robustness of the observed LDOS features against symmetry breaking. In extinction, Hentschel *et al.* have found a remarkable persistence of the Fano feature in heptamers with broken symmetry [10]. Figure 5.4(a) shows a series of CL excitability maps at different wavelengths around the Fano resonance for a symmetry-broken heptamer. The rightmost panel of Fig. 5.4(a) shows a SEM image of the symmetry broken structure, showing that the central particle is horizontally displaced to the left by 20 nm, yet without particles touching. The measurements on the asymmetric heptamer in Fig. 5.4(a) share the same prominent features observed for the symmetric heptamer in Fig. 5.2(a), namely, a reduced CL excitability, i.e. radiative LDOS, on the central particle on the blue side of the Fano resonance [left panel of Fig. 5.4(a)] and a swap of the radiative LDOS to the central particle on the red side of the Fano resonance [third panel of Fig. 5.4(a)]. This overall robustness of the Fano resonance in the LDOS is consistent with the robustness against symmetry breaking of the Fano resonance in plane-wave extinction reported by Hentschel *et al.* [10]. In addition we note that symmetry breaking redistributes the LDOS over the outer ring. On the blue side of the Fano resonance the reduced LDOS on the central particle is extended to the closest particle on the outer ring. Symmetry breaking is hence a tool to redistribute LDOS without losing the overall Fano resonance. Figure 5.4(b) shows calculated maps of the radiative LDOS for a plasmonic heptamer with the central particle displaced to the left. The calculations fully corroborate the experimental observations on the plasmonic heptamer with broken symmetry.

Since the potential of the Fano resonance for bright antennas requires a high quantum yield for emission, we calculated the quantum yield of a dipolar emitter coupled to a symmetric plasmonic heptamer with particle diameters of 100 nm and gap width 25 nm, which has its Fano resonance around 600 nm [see Fig. 5.2]. The blue/green curve in Fig. 5.4(c) shows the quantum efficiency of a dipolar emitter in the vicinity

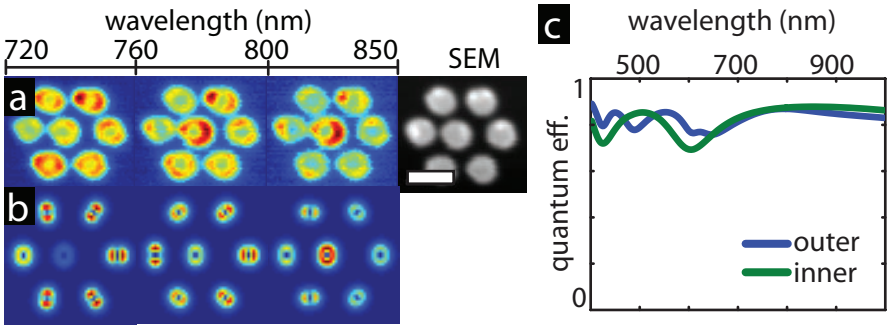

Figure 5.4: (a) CL excitability maps for increasing wavelength from left to right for plasmonic heptamer with symmetry broken by displacing central particle along horizontal symmetry axis. Right-most panel shows SEM image of structure (scalebar 200 nm). (b) Calculated radiative LDOS of heptamer with central particle off-center. (c) Quantum efficiency of spontaneous emitter coupled to outer/inner particle of plasmonic heptamer (blue/green curve).

of and therefore mostly driving the outer/inner particle of the heptamer. Notably, throughout the spectral range of the Fano resonance around 600 nm the quantum efficiency remains above 70%, illustrating the fact that the plasmonic heptamer acts as both a bright and efficient optical antenna, even at the sub-radiant resonance.

5.7 Far-field interference in eigen-basis

To gain further insight in the response of the individual modes, we focus on plane-wave driving and Fano interference in the extinction cross-section σ_{ext} of the symmetric heptamer plotted as the dash-dotted line in Fig. 5.5(a). In Fig. 5.5(b,c) we plot the induced (complex) polarization $\mathscr{P}$ of the eigen-modes. Extinction [work done by the driving $\text{Im}(\mathscr{E}_{\text{ext}} \cdot \mathscr{P})$, normalized to incident intensity] can readily be split into contributions from different modes [Fig. 5.5(a)]. The total extinction cross-section is in excellent quantitative agreement with reported brute-force numerical results [11], underlining the suitability of a dipole model. The super-radiant mode provides a broad positive extinction [solid line in Fig. 5.5(a)]. The Fano dip in the sum is created by the sub-radiant mode [long-dashed line]. Its surprising negative contribution to σ_{ext} indicates that the mode feeds energy back into the driving field, equivalent to destructive far-field interference. This energy cannot result from direct driving of the super-radiant mode and subsequent amplitude transfer [19], since the eigen-modes are strictly decoupled. Since the projection of plane-wave driving on the eigen-modes has no frequency dependence, the excitation amplitudes in Fig. 5.5(b) simply follow the eigen-polarizabilities in Fig. 5.3(c,d). On the Fano dip, the sub-radiant mode's net dipole moment compensates that of the super-radiant mode such that their superposition barely radiates. Importantly, the sub-radiant eigen-mode must possess nonzero dipole

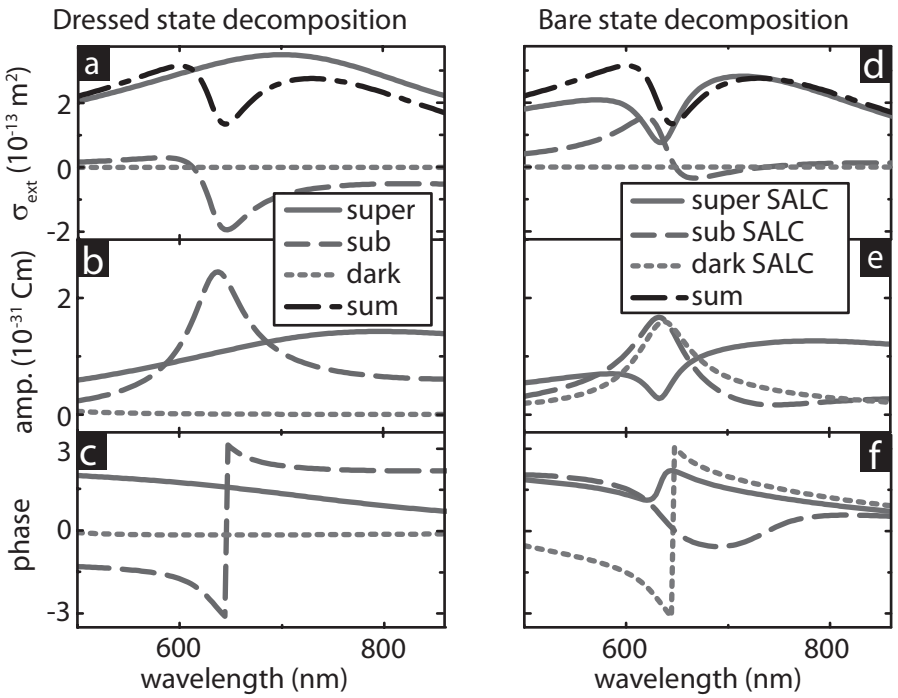

Figure 5.5: (a) Calculated contribution of eigen-modes [Fig. 5.3(b)] to extinction cross-section of plasmonic heptamers. (b) Eigen-mode amplitude and (c) phase relative to driving field. (d,e,f) Corresponding graphs in the nondiagonal bare-state basis [Fig. 5.3(a)].

moment (and excellent radiation pattern overlap with the super-radiant mode) to lead to a PIT dip in extinction. It is this nonzero dipole moment together with a very strong, narrow eigen-polarizability [dotted lines in Fig. 5.3(c,d)] that also ensures that the sub-radiant mode can give rise to an enhanced radiative LDOS at the central particle, as seen from Fig. 5.2(f).

5.8 Identification of bare and dressed states

Fano interference is inextricably linked to coherent transfer of amplitude to states that are not directly driven [19]. Indeed, this is the picture in which the discussion of PIT has been led thus far [4–13]. Necessarily, the eigen-mode basis of any linear system never involves amplitude transfer, as eigen-modes are decoupled. Figure 5.5(a-c) confirms this viewpoint, which is analogous to analyzing atomic EIT in terms of dressed states [1] that decay to the same continuum with opposite phase. The alternative view on EIT, in which amplitude transfer *does* occur, is as an interference of different pathways of coherently coupled bare states [1]. The basis of SALCs [Fig. 5.3(a)]

provides the analog of such bare states in EIT for the PIT system. The contributions of the three SALCs to σ_{ext} plotted in Fig. 5.5(d) reveal a dip in the broad band of the super-radiant SALC [solid line]. However, also the sub-radiant SALC [long-dashed line] contributes significantly. Even though the contribution of the dark SALC [dotted] to σ_{ext} is strictly zero it is crucial for the Fano dip. Figure 5.5(e) shows that the dark SALC acquires an amplitude at the Fano dip as large as that of the sub-radiant SALC. However, around the Fano dip the polarization $\mathscr{P}$ of the dark SALC is locked in amplitude and phase to the sub-radiant SALC [Fig. 5.5(e,f)]. One can hence view the dark SALC as a screening effect that allows to describe the three-state interaction as the interaction between just two oscillators [19] with renormalized resonance frequencies and strengths. In conclusion, in the SALC basis in which $\boldsymbol{M}$ is not diagonal, amplitude transfer occurs to a linear combination of the sub-radiant and dark SALC [Fig. 5.5(e)]. The link between the complementary interpretations of PIT in scattering systems via either amplitude transfer in a nondiagonal basis or far-field interference in an eigen-basis is ultimately provided by the optical theorem which constrains $\boldsymbol{M}$ and thereby inextricably links radiated power and induced complex dipole moments to satisfy energy conservation. Generally, in *any* nondiagonal basis an apparent amplitude transfer between nondiagonal basis vectors will occur. In particular, the SALC basis commonly chosen by the community and depicted in Fig. 5.3(a) is *not* distinguished from any other orthonormal linear combination of dipole moments, except for *one* basis set, which is the eigen-basis depicted in Fig. 5.3(b). This one special eigen-basis is determined by the strength of the coupling between the constituents and can therefore never be retrieved from symmetry considerations alone. Likewise, attempts to retrieve eigen-modes from numerically obtained field snapshots must fail [11, 12, 31]. Such field maps are necessarily always obtained as a brute-force solution under certain driving conditions and therefore represent a superposition of eigen-modes with individual amplitudes according to the overlap between the driving field and the respective eigen-mode. However, the eigen-modes are by their very nature independent of the driving conditions since they purely arise from the coupling constants mediating the interaction between the individual constituents of the PIT structure. The very same coupling constants would have to enter a coupled mechanical oscillator model [19] in order to provide a quantitative description of the physical reality. Since the coupling and damping constants in the PIT scattering problem are electrodynamic in nature and are strictly constrained by the unitary limit they can never be obtained from a coupled-mechanical-oscillator simile. Therefore, all such an oscillator model can provide is (for the special case of constituents with Lorentzian response) a set of formulas to fit from hindsight the damping rates and coupling constants after the solution to the problem is already known thanks to a numerical or real-world experiment [6, 18].

5.9 Conclusions

In conclusion, we measured a spatial redistribution of the LDOS of plasmonic heptamers using CL at the spectral position that coincides with the reported Fano extinction

dip. Both LDOS redistribution and Fano dip result from interference in the far field of the same two eigen-modes, excited in different coherent superpositions. Our findings bear a plethora of exciting prospects to harness the near field of plasmonic molecules, especially in the context of spontaneous emission, or control of any process in sensing, spectroscopy and nonlinear optics that benefits from an enhanced LDOS. Strikingly, optimizing a Fano dip in extinction requires engineering of radiation-pattern overlap between two involved modes that ensures an enhanced LDOS by constructive interference. Also, completely dark SALCs may be utilized to optimize resonances and interaction strengths, similar to the screening dark SALC in the heptamer. For fluorescence applications, one typically requires simultaneous optimization of pump field generated from a far-field beam, and optimization of the LDOS at the red-shifted emission frequency. Our generic quantitative solution approach may yield universal bounds on how to optimize the solution to such a problem using optical antennas with a Fano resonance.

References

[1] M. Fleischhauer, A. Imamoglu, and J. P. Marangos, *Electromagnetically induced transparency: Optics in coherent media*, Rev. Mod. Phys. **77**, 633 (2005).

[2] L. Novotny and B. Hecht, *Principles of Nano-Optics*, Cambridge University Press, Cambridge, 2006.

[3] C. M. Soukoulis and M. Wegener, *Past achievements and future challenges in the development of three-dimensional photonic metamaterials*, Nature Photon. (2011).

[4] S. Zhang, D. A. Genov, Y. Wang, M. Liu, and X. Zhang, *Plasmon-induced transparency in metamaterials*, Phys. Rev. Lett. **101**, 047401 (2008).

[5] B. Luk'yanchuk, N. I. Zheludev, S. A. Maier, N. J. Halas, P. Nordlander, H. Giessen, and C. T. Chong, *The Fano resonance in plasmonic nanostructures and metamaterials*, Nature Mater. **9**, 707 (2010).

[6] N. Liu, L. Langguth, T. Weiss, J. Kästel, M. Fleischhauer, T. Pfau, and H. Giessen, *Plasmonic analogue of electromagnetically induced transparency at the Drude damping limit*, Nature Mater. **8**, 758 (2009).

[7] N. Verellen, Y. Sonnefraud, H. Sobhani, F. Hao, V. V. Moshchalkov, P. V. Dorpe, P. Nordlander, and S. A. Maier, *Fano resonances in individual coherent plasmonic nanocavities*, Nano Lett. **9**, 1663 (2009).

[8] J. A. Fan, K. Bao, C. Wu, J. Bao, R. Bardhan, N. J. Halas, V. N. Manoharan, G. Shvets, P. Nordlander, and F. Capasso, *Fano-like interference in self-assembled plasmonic quadrumer clusters*, Nano Lett. **10**, 4680 (2010).

[9] F. Hao, P. Nordlander, Y. Sonnefraud, P. V. Dorpe, and S. A. Maier, *Tunability of subradiant dipolar and Fano-type plasmon resonances in metallic ring/disk cavities: Implications for nanoscale optical sensing*, ACS Nano **3**, 643 (2009).

[10] M. Hentschel, D. Dregely, R. Vogelgesang, H. Giessen, and N. Liu, *Plasmonic oligomers: The role of individual particles in collective behavior*, ACS Nano **5**, 2042 (2011).

[11] M. Hentschel, M. Saliba, R. Vogelgesang, H. Giessen, A. P. Alivisatos, and N. Liu, *Transition from isolated to collective modes in plasmonic oligomers*, Nano Lett. **10**, 2721 (2010).

[12] J. B. Lassiter, H. Sobhani, J. A. Fan, J. Kundu, F. Capasso, P. Nordlander, and N. J. Halas, *Fano resonances in plasmonic nanoclusters: Geometrical and chemical tunability*, Nano Lett. **10**, 3184 (2010).

[13] P. Alonso-Gonzalez, M. Schnell, P. Sarriugarte, H. Sobhani, C. Wu, N. Arju, A. Khanikaev, F. Golmar, P. Albella, L. Arzubiaga, F. Casanova, L. E. Hueso, P. Nordlander, G. Shvets,

and R. Hillenbrand, *Real-space mapping of Fano interference in plasmonic metamolecules*, Nano Lett. **11**, 3922 (2011).

[14] S. Kühn, U. Håkanson, L. Rogobete, and V. Sandoghdar, *Enhancement of single-molecule fluorescence using a gold nanoparticle as an optical nanoantenna*, Phys. Rev. Lett. **97**, 017402 (2006).

[15] P. Anger, P. Bharadwaj, and L. Novotny, *Enhancement and quenching of single-molecule fluorescence*, Phys. Rev. Lett. **96**, 113002 (2006).

[16] A. Kinkhabwala, Z. Yu, S. Fan, Y. Avlasevich, K. Müllen, and W. E. Moerner, *Large single-molecule fluorescence enhancements produced by a bowtie nanoantenna*, Nature Photon. **3**, 654 (2009).

[17] B. Gallinet and O. J. F. Martin, *Ab initio theory of Fano resonances in plasmonic nanostructures and metamaterials*, Phys. Rev. B **83**, 235427 (2011).

[18] B. Gallinet and O. J. F. Martin, *Influence of electromagnetic interactions on the line shape of plasmonic Fano resonances*, ACS Nano **5**, 8999 (2011).

[19] C. L. G. Alzar, M. A. G. Martinez, and P. Nussenzveig, *Classical analog of electromagnetically induced transparency*, Am. J. Phys. **70**, 37 (2002).

[20] A. de Hoogh, B. Hommersom, and A. F. Koenderink, *Wavelength-selective addressing of visible and near-infrared plasmon resonances for SU8 nanolithography*, Opt. Express **19**, 11405 (2011).

[21] C. F. Bohren and D. R. Huffman, *Absorption and Scattering of Light by Small Particles*, John Wiley and Sons, New York, 1983.

[22] A. F. Koenderink and A. Polman, *Complex response and polariton-like dispersion splitting in periodic metal nanoparticle chains*, Phys. Rev. B **74**, 033402 (2006).

[23] F. J. García de Abajo, *Optical excitations in electron microscopy*, Rev. Mod. Phys. **82**, 209 (2010).

[24] M. Kuttge, E. J. R. Vesseur, A. F. Koenderink, H. J. Lezec, H. A. Atwater, F. J. García de Abajo, and A. Polman, *Local density of states, spectrum, and far-field interference of surface plasmon polaritons probed by cathodoluminescence*, Phys. Rev. B **79**, 113405 (2009).

[25] J. Prangsma, *Local and dynamic properties of light interacting with subwavelength holes*, PhD thesis, University of Twente, 2009.

[26] N. Yamamoto, S. Ohtani, and F. J. García de Abajo, *Gap and Mie plasmons in individual silver nanospheres near a silver surface*, Nano Lett. **11**, 91 (2011).

[27] J. E. Rosenthal and G. M. Murphy, *Group theory and the vibrations of polyatomic molecules*, Rev. Mod. Phys. **8**, 317 (1936).

[28] N. A. Mirin, K. Bao, and P. Nordlander, *Fano resonances in plasmonic nanoparticle aggregates*, J. Phys. Chem. A **113**, 4028 (2009).

[29] E. B. Wilson, *The normal modes and frequencies of vibration of the regular plane hexagon model of the benzene molecule*, Phys. Rev. **45**, 706 (1934).

[30] E. Prodan, C. Radloff, N. J. Halas, and P. Nordlander, *A hybridization model for the plasmon response of complex nanostructures*, Science **302**, 419 (2003).

[31] J. A. Fan, C. Wu, K. Bao, J. Bao, R. Bardhan, N. J. Halas, V. N. Manoharan, P. Nordlander, G. Shvets, and F. Capasso, *Self-assembled plasmonic nanoparticle clusters*, Science **328**, 1135 (2010).

6

Theory of a Superemitter in a Hybrid Photonic System

We theoretically investigate how the enhancement of the radiative decay rate of a spontaneous emitter provided by coupling to an optical antenna is modified when this 'superemitter' is introduced into a complex photonic environment that provides an enhanced local density of optical states (LDOS) itself, such as a microcavity or stratified medium. We show that photonic environments with increased LDOS further boost the performance of antennas that scatter weakly, for which a simple multiplicative LDOS lumping rule holds. In contrast, enhancements provided by antennas close to the unitary limit, i.e. close to the limit of maximally possible scattering strength, are strongly reduced by an enhanced LDOS of the environment. Thus, we identify multiple scattering in hybrid photonic systems as a powerful mechanism for LDOS engineering. A didactic section discusses a hybrid photonic system in both a coupled-oscillator and a lumped-circuit picture.

6.1 Introduction

Optics encompasses the most fascinating part of the electromagnetic spectrum, due to its energetic overlap with electronic transitions in matter. Nanophotonics aims at controlling such transitions by molding light at sub-wavelength scales. Purcell first predicted that resonators modify the radiative lifetime of spontaneous emitters [1].

Modern literature discusses the Purcell effect in terms of the local density of optical states (LDOS), a fundamental quantity governing spontaneous emission, thermal radiation, and vacuum forces [2]. Two tools have emerged to shape the LDOS: On the one hand, interfaces [3, 4], photonic crystals [5, 6] and dielectric microcavities [7] modulate the LDOS on length scales of order $\lambda/2$ via interference. On the other hand, optical antennas [8–11] employ intrinsic plasmonic resonances to enhance the LDOS on $\lambda/20$ length scales. Optical antennas are so small compared to the wavelength λ that a source-antenna ensemble essentially radiates as a dipole. The term 'superemitter' [12] captures this similarity to a bare molecule, but with much higher radiative rate. The availability of photonic building blocks on such different length scales raises the exciting idea of integrating deep-subwavelength superemitters in much larger dielectric structures to obtain a combined advantage, for example by placing a nano-antenna inside a microresonator [13] or onto a planar dielectric antenna [14]. These developments trigger the question how the LDOS of such hybrid systems emerges from the separate entities. Nano-optic devices can be interpreted as lumped optical elements [15–19], where the LDOS acts as an impedance for a spontaneous emitter, due to the fact that it radiates energy into its environment. Based on this analogy, some circuit rule might be hoped for, which lumps the LDOS provided by each photonic building block. Surprisingly, however, even the paradigmatic case of a deep-subwavelength optical antenna embedded in an environment with an LDOS modulation on a length scale comparable to the wavelength has remained unaddressed thus far.

This Chapter investigates how the decay-rate enhancement provided by a superemitter varies when it is placed within a larger photonic system, i.e., how the LDOS lumps. We illustrate our theory, which is valid for any background LDOS, by two archetypical examples: First, we investigate a superemitter coupled to high-Q resonances. Second, we consider a superemitter in front of a perfect mirror without any resonances. Our analytic, yet fully electrodynamic model yields a simple multiplicative LDOS lumping rule for moderate antenna factors. For antennas close to the unitary limit, this simple lumping rule breaks down and the total enhancement becomes proportional to the *inverse* LDOS of the background system. This insight paves the way for engineering the LDOS by exploiting multiple scattering in hybrid photonic systems. For didactic purposes we discuss the case of a nano-antenna coupled to a single cavity mode in a coupled-oscillator picture. Finally, we offer a lumped-circuit analogon to model the superemitter-cavity system and outline how mechanical-oscillator and lumped-circuit pictures fall short of quantitatively describing strongly scattering systems.

6.2 A spontaneous emitter as a constant-current source

The radiative decay-rate enhancement of a quantum emitter can be calculated via the power required to sustain a monochromatic classical point current $\boldsymbol{j} = \dot{\boldsymbol{p}}_0$ that loses energy by radiation [2]. This power equals the cycle-averaged work per unit time done

by the source's electric field on its own dipole moment $\boldsymbol{p}_0$. The electric field generated at position $\boldsymbol{r}$ due to a source $\boldsymbol{p}_0$ at $\boldsymbol{r}_0$ is calculated via the electric Green function $\boldsymbol{G}(\boldsymbol{r},\boldsymbol{r}_0)$ of the respective system. This approach yields the power required to drive the source $P = \frac{1}{2}\omega \boldsymbol{p}_0^T \mathrm{Im}\boldsymbol{G}(\boldsymbol{r}_0,\boldsymbol{r}_0)\boldsymbol{p}_0$. For lossy environments, this expression describes the total decay rate, i.e., radiation plus quenching induced by the environment. We use the term LDOS to refer to $\mathrm{Im}\boldsymbol{G}$ projected on a unit vector along $\boldsymbol{p}_0$, i.e. to the decay-rate modification of a molecular dipole $\boldsymbol{p}_0$ at position $\boldsymbol{r}_0$. Every strategy to boost decay rates via a photonic structure, be it large and dielectric, or a nano-antenna, represents a modification of $\mathrm{Im}\boldsymbol{G}$. The small size and dipolar nature of a nano-antenna however suggest to interpret its rate enhancement rather as an enhancement of the dipole moment $\boldsymbol{p}_0$ instead of a change in $\mathrm{Im}\boldsymbol{G}$ [12]. The simplest optical antenna is just a particle with polarizability tensor $\boldsymbol{\alpha}(\omega)$ [8, 9]. At distance d in the near-field of an emitter, the particle acquires a large dipole moment $\propto \boldsymbol{\alpha}/d^3$. The total dipole moment of the emitter-particle assembly $\boldsymbol{p} = [1+\boldsymbol{\alpha}/d^3]\boldsymbol{p}_0$ can exceed by far the source's dipole moment $\boldsymbol{p}_0$, rationalizing the term 'superemitter'. If $d \ll \lambda$, the power radiated by a superemitter comprised of an isotropic particle of polarizability α with the dipole moment $\boldsymbol{p}$ of the source radially aligned reads [12, 14]

$$P = \frac{1}{2}\omega |\boldsymbol{p}_0|^2 \,\mathrm{LDOS_B}(\boldsymbol{r}_0) \times A \tag{6.1}$$

and exceeds the power radiated by the bare source by the antenna factor $A = \left|1+\alpha/d^3\right|^2 \approx |\alpha|^2/d^6$. The rate enhancement provided by the embedding background is described by $\mathrm{LDOS_B}$. Mie calculations show that A accurately describes antenna particles up to 60 nm in diameter in vacuum [20]. This reasoning suggests that a superemitter can simply replace a bare molecule as a probe of larger photonic systems, since a simple product rule lumps the enhancements provided by antenna and photonic environment as $A \cdot \mathrm{LDOS_B}$.

6.3 Analytic point-scattering model

We analyze the hypothesis of a simple lumping rule in an analytic electrodynamic point-scattering theory, which is exact to all multiple scattering orders, with the sole assumption that the scatterers that constitute the antenna are well approximated as point dipoles. The N scatterers acquire dipole moments $\boldsymbol{p}_1,\ldots,\boldsymbol{p}_N$ in proportion to their polarizabilities $\boldsymbol{\alpha}_1,\ldots,\boldsymbol{\alpha}_N$, and the incoming electric fields $\boldsymbol{E}_{\mathrm{in}}(\boldsymbol{r}_1),\ldots,\boldsymbol{E}(\boldsymbol{r}_N)$ at their locations $\boldsymbol{r}_n$ through [21, 22]

$$\boldsymbol{p}_n = \boldsymbol{\alpha}_n \left[\boldsymbol{E}_{\mathrm{in}}(\boldsymbol{r}_n) + \sum_{m\neq n} \boldsymbol{G}_{\mathrm{B}}(\boldsymbol{r}_n,\boldsymbol{r}_m)\cdot\boldsymbol{p}_m \right]. \tag{6.2}$$

By construction, the antenna described by the $\boldsymbol{\alpha}_n$ is explicitly separated from the background that it probes, which is quantified by its Green function $\boldsymbol{G}_{\mathrm{B}} = \boldsymbol{G}_{\mathrm{vac}} + \boldsymbol{G}_{\mathrm{s}}$ that is commonly split in a free space contribution $\boldsymbol{G}_{\mathrm{vac}}$ and a scattered part $\boldsymbol{G}_{\mathrm{s}}$. For a

consistent theory, three facts need to be accounted for. First, the particle polarizability directly depends on the background via [19]

$$\boldsymbol{\alpha}_n^{-1} = \boldsymbol{\alpha}_{n,0}^{-1} - \boldsymbol{G}_{\mathrm{B}}(\boldsymbol{r}_n, \boldsymbol{r}_n), \tag{6.3}$$

where $\boldsymbol{\alpha}_{n,0}$ is the electrostatic polarizability. Since $\mathrm{Re}\boldsymbol{G}_{\mathrm{vac}}$ diverges at the source, and one is only interested in relative frequency shifts, it is commonly included in $\boldsymbol{\alpha}_0$ to yield a finite resonance frequency ω_0. Note that isotropic particles can *acquire* anisotropy due to anisotropy in radiation damping given by $\mathrm{Im}\boldsymbol{G}_{\mathrm{B}}$ and resonance shift due to $\mathrm{Re}\boldsymbol{G}_{\mathrm{B}}$ in complex photonic systems. Second, the source in our model is a single (unpolarizable) dipole $\boldsymbol{p}_0$ at $\boldsymbol{r}_0$ so $\boldsymbol{E}_{\mathrm{in}}(\boldsymbol{r}_n) = \boldsymbol{G}_{\mathrm{B}}(\boldsymbol{r}_n, \boldsymbol{r}_0)\boldsymbol{p}_0$. Third, the total decay rate of the source is found via the cycle-averaged work done by the *total* electric field on the source $\boldsymbol{p}_0$ [2]. Therefore, the total $\mathrm{LDOS}_{\mathrm{A+B}}$ experienced by the source due to the simultaneous presence of an antenna and a complex background system can be expressed as

$$\mathrm{LDOS}_{\mathrm{A+B}} = \boldsymbol{p}_0^T \cdot \mathrm{Im}\boldsymbol{G}_{\mathrm{B}}(\boldsymbol{r}_0, \boldsymbol{r}_0) \cdot \boldsymbol{p}_0 + \mathrm{Im} \sum_{n \geq 1} \boldsymbol{p}_0^T \cdot \boldsymbol{G}_{\mathrm{B}}(\boldsymbol{r}_0, \boldsymbol{r}_n) \cdot \boldsymbol{p}_n. \tag{6.4}$$

The first term is the $\mathrm{LDOS}_{\mathrm{B}}$ provided by the background without antenna, while the second term arises from the antenna. We calculate the LDOS of the hybrid system from Eq. (6.4) after solving Eq. (6.2) for the $3N$ dipole moments $\boldsymbol{p}_1, \ldots, \boldsymbol{p}_N$. We use the exact Green function for a sphere [23] and a planar interface [2, 24] to evaluate how a superemitter probes the two canonical cases of microcavity resonances and non-resonant interfaces [3].

6.4 A superemitter coupled to a microcavity

As a superemitter we consider a source $\boldsymbol{p}_0$ in the gap of a dimer antenna with $\boldsymbol{p}_0$ along the symmetry axis [see Fig.6.1(a)]. The 40 nm diameter Ag spheres forming the dimer have a center-center distance of 60 nm.* The dashed line in Fig. 6.1(b) shows $\mathrm{Im}\boldsymbol{\alpha}$ of a single antenna particle in vacuum. The decay-rate enhancement of the source in the antenna gap [solid line] reaches about 1200, in good agreement with full-multipole calculations [25]. The dimer resonance is red-shifted and broadened by super-radiant damping compared to the single particle due to longitudinal symmetric dipolar plasmon hybridization [26].

As a first test of LDOS lumping we consider as a background a glass sphere ($n = 1.5$, radius 1.2 µm) supporting whispering-gallery modes, illustrated in Fig. 6.1(a). Characteristic resonances are clearly visible as sharp peaks with $Q \approx 7 \times 10^2$ in the sphere's extinction efficiency [27] [Fig. 6.1(c), dashed line]. The Purcell factor for a radially oriented source 50 nm from the sphere surface [solid line in Fig. 6.1(c)] reaches moderate values around 10. Only every second peak in extinction yields

*For spherical particles of volume V and dielectric constant $\epsilon(\omega)$, the electrostatic polarizability is simply $3V(\epsilon - 1)/(\epsilon + 2)$. A Drude model for ϵ yields a Lorentzian. We choose $\omega_0 = 4.76 \times 10^{15}\,\mathrm{s}^{-1}$ and $\gamma = 8.3 \times 10^{12}\,\mathrm{s}^{-1}$.

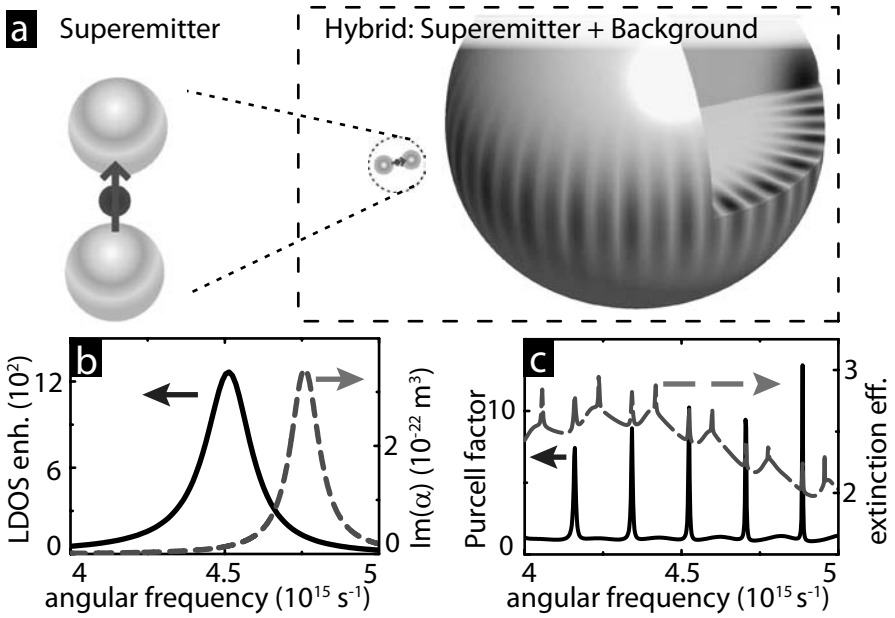

Figure 6.1: (a) Left: Sketch of superemitter formed by two silver spheres. The fluorescent source is located between the two particles with its dipole moment along the symmetry axis. Right: Hybrid photonic system comprised of superemitter embedded in background system formed by dielectric sphere supporting a whispering-gallery mode. (b) Dashed line: polarizability of a single antenna particle in vacuum. Solid line: antenna enhancement factor for superemitter sketched in (a) in vacuum. (c) Dashed line: Extinction efficiency of dielectric sphere showing narrow Mie resonances. Solid line: Purcell factor of the Mie sphere 50 nm from its surface for a radially aligned source.

Purcell enhancement, which reflects the field orientation according to the common TE/TM type classification [28]. We now place the superemitter with the center of the closest antenna particle 50 nm from the sphere's surface and the symmetry axis pointing radially outwards [see Fig. 6.1(a)]. We stress that throughout the entire spectrum the coupling between antenna and cavity is weak. The antenna does not significantly shift or spoil the microsphere resonances, as predicted by Waldron's formula $\Delta\omega/\omega = -\alpha/V|E|^2$, due to their large mode volumes Vcompared to $\boldsymbol{\alpha}$, their low Q-factors [28, 29], and placement of the antenna far from the normalized mode function $|E|^2$ maxima. The solid line in Fig. 6.2(a) is the decay-rate enhancement for the emitter embedded in the antenna, in turn located next to the Mie sphere, i.e. the rate in the hybrid system normalized to the rate of the bare source in vacuum. While the overall shape of the enhancement provided by the antenna in vacuum [Fig. 6.2(a), dashed] is still visible, sharp features appear at five spectral positions coinciding with the sphere's whispering-gallery modes [cf. Fig. 6.1(c)]. To illustrate the effect of the background

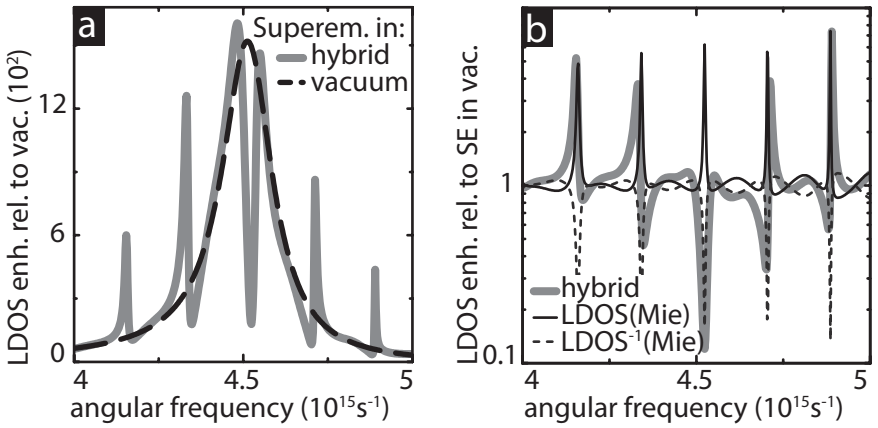

Figure 6.2: (a) Solid line (hybrid system): Decay rate of source in the gap of the superemitter next to the Mie sphere normalized to rate of source in vacuum. Dashed line (superemitter in vacuum): Decay rate of source in the gap of the superemitter in vacuum normalized to rate of source in vacuum. At the Mie resonances, the hybrid LDOS is drastically modified compared to that of the antenna in vacuum. (b) Thick solid line (hybrid system): Decay-rate enhancement in hybrid system [solid line in (a)] normalized to the rate enhancement in the superemitter in vacuum [dashed line in (a)]. Off antenna resonance, the superemitter benefits from the LDOS enhancement offered by the sphere (thin solid line), while on antenna resonance the enhancement is suppressed by the *inverse* of the sphere's LDOS (dashed line).

system on the superemitter we normalize the decay-rate enhancement in the hybrid system [solid line in Fig. 6.2(a)] to the enhancement provided by the bare antenna in vacuum [dashed line in Fig. 6.2(a)] and plot it as the thick solid line in Fig. 6.2(b). The sharp enhancements in the wings of the antenna resonance follow the LDOS of the sphere, denoted by the thin solid line in Fig. 6.2(b). Therefore, off antenna resonance, at still significant antenna factors, we find the anticipated behavior of a superemitter that the already antenna-enhanced decay rate is further boosted by a high $\mathrm{LDOS_B}$ of the background. Furthermore, we note the dispersive features in the enhancement which swap orientation upon crossing the antenna resonance. Surprisingly, however, on antenna resonance, the LDOS enhancement is strongly suppressed by the Mie sphere and actually follows the *inverse* LDOS of the sphere, plotted as the dashed line in Fig. 6.2(b). This LDOS suppression close to antenna resonance cannot be explained by a spoiling or detuning of the cavity by the antenna, since this would only result in a shift or absence of a sharp line of extra enhancement on top of the bare antenna factor. Since Waldron's formula excludes that the LDOS suppression results from a spoiling of the Mie resonances by the antenna, Fig. 6.2(a) hence implies a spoiling of the antenna by the cavity resonance.

6.5 Radiation reaction of an optical antenna

In order to explain the surprising spoiling of the antenna enhancement by a large background $\mathrm{LDOS_B}$ one needs to interpret Eq. (6.1) correctly, by taking radiation damping according to Eq. (6.3) properly into account. For simplicity we now discuss an antenna significantly smaller than the wavelength and described as a single scatterer with polarizability $\boldsymbol{\alpha}$. It is easy to show that a small dimer antenna is described as a single scatterer with $\boldsymbol{\alpha}_{\mathrm{eff}} = 2\left[\boldsymbol{\alpha}_{\mathrm{B}}^{-1} - \boldsymbol{G}_{\mathrm{B}}(\boldsymbol{r}_1, \boldsymbol{r}_2)\right]^{-1}$. Equation (6.3) ensures that the optical theorem $\mathrm{Im}\alpha \geq \mathrm{LDOS_B}\,|\alpha|^2$ is fulfilled, where equality holds for the case of no material loss. The optical theorem is a fundamental relation in any scattering theory [30] and a full vectorial expression was given in Eq. (4.26). To grasp how the optical theorem bounds the imaginary part of the polarizability it is most instructive to consider an isotropic particle with $\mathrm{Im}\,\boldsymbol{\alpha} = \mathrm{Im}\,\alpha\mathbb{1}$ in a homogeneous and isotropic background system described by $\mathrm{Im}\,\boldsymbol{G}_{\mathrm{B}} = \mathrm{Im}\,G_{\mathrm{B}}\mathbb{1}$. The optical theorem then requires

$$\mathrm{Im}\alpha \leq \frac{1}{\mathrm{Im}G_{\mathrm{B}}}, \tag{6.5}$$

which is a general form of the unitary limit. In vacuum, this limit is well-known for extinction cross-section as $\sigma_{\mathrm{ext}} = 4\pi k\mathrm{Im}\alpha \leq \frac{3}{2\pi}\lambda^2$, a limit reached by an ideal scatterer on resonance, and closely approached by any plasmon particle above 20 nm in size [20]. The unitary limit, Eq. (6.5), states that $\boldsymbol{\alpha}$ of a strong scatterer, and hence the dipole moment it acquires, is proportional to the *inverse* LDOS. Since a strong scatterer is predominantly damped by radiation, increasing the background LDOS increases its loss due to radiation and therefore suppresses the scatterer's response [31].

To quantitatively verify that the unitary limit indeed governs the hybrid system's LDOS we evaluate Eq. (6.4) for a physically small superemitter described by a single scatterer $\boldsymbol{\alpha}_1$ at $\boldsymbol{r}_1$. As a consequence, the sum describing the contribution of the antenna to the total LDOS in Eq. (6.4) reduces to the single term $\mathrm{Im}\,(\boldsymbol{p}_0^{\mathrm{T}}\boldsymbol{G}_{\mathrm{B}}\boldsymbol{\alpha}_1\boldsymbol{G}_{\mathrm{B}}\boldsymbol{p}_0)$. Ordering the resulting terms in powers of $\frac{1}{d}$ (with $d = |\boldsymbol{r}_1 - \boldsymbol{r}_0|$) shows that the enhancement of a physically small superemitter is described by the leading term

$$\mathrm{LDOS_A} = \boldsymbol{p}_0^T\mathrm{Re}\boldsymbol{G}_{\mathrm{vac}}(\boldsymbol{r}_0, \boldsymbol{r}_1)\mathrm{Im}\boldsymbol{\alpha}_1\mathrm{Re}\boldsymbol{G}_{\mathrm{vac}}(\boldsymbol{r}_1, \boldsymbol{r}_0)\boldsymbol{p}_0, \tag{6.6}$$

which is of order $1/d^6$ and precisely yields Eq. (6.1).[†] We return to our example of an optical antenna coupled to a Mie sphere to illustrate the effect of the background system on $\mathrm{Im}\boldsymbol{\alpha}_{\mathrm{Mie}}$. In Fig. 6.3(a) we plot the radial component of the sphere's Green function $\boldsymbol{G}_{\mathrm{Mie}}$ at the superemitter (50 nm from the sphere surface). Real and imaginary part of $\boldsymbol{G}_{\mathrm{Mie}}$ show the typical line-shape of a resonance, where $\mathrm{Im}\boldsymbol{G}_{\mathrm{Mie}}$ equals the microcavity Purcell factor at the source [cf. Fig. 6.1(c)]. In Fig. 6.3(b) we plot as the thick solid line the radial component of $\mathrm{Im}\boldsymbol{\alpha}_{\mathrm{Mie}}$ of an antenna located 50 nm from the sphere surface. The values of $\boldsymbol{G}_{\mathrm{Mie}}$ in Fig. 6.3(a) are the correction terms entering Eq. (6.3) that modify $\boldsymbol{\alpha}_{\mathrm{Mie}}$ close to the sphere [thick solid line in Fig. 6.3(b)] with respect to $\boldsymbol{\alpha}_{\mathrm{vac}}$ in vacuum [dash-dotted line in Fig. 6.3(b)]. Close to antenna resonance

[†]Note that $\boldsymbol{G}_{\mathrm{vac}} \propto 1/d^3$ while $\boldsymbol{G}_{\mathrm{B}}$ is of order k^3.

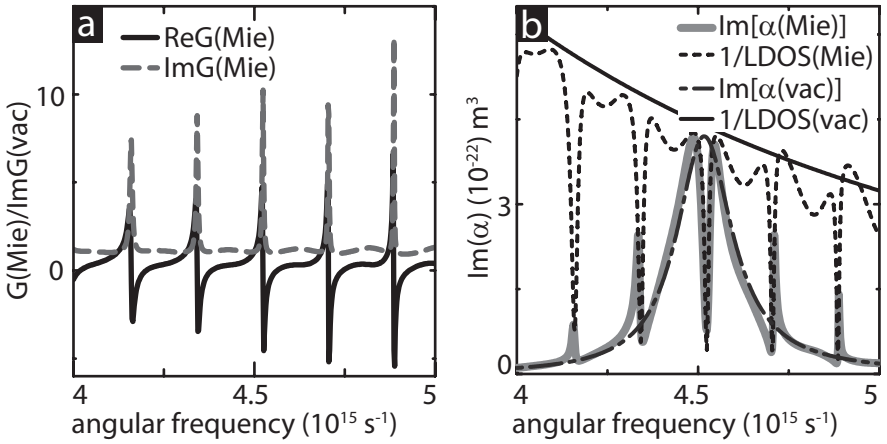

Figure 6.3: (a) Real (solid) and imaginary (dashed) parts of the radial component of the Green function of the Mie sphere 50 nm from sphere's surface. These terms enter the radiation correction to $\boldsymbol{\alpha}_{\mathrm{Mie}}$. (b) Thick solid line: Radial component of the antenna polarizability $\boldsymbol{\alpha}_{\mathrm{Mie}}$ when located 50 nm from the Mie sphere. Dash-dotted line: $\boldsymbol{\alpha}_{\mathrm{vac}}$ for same antenna in vacuum. While $\boldsymbol{\alpha}_{\mathrm{vac}}$ is limited by the inverse vacuum LDOS (thin solid line), $\boldsymbol{\alpha}_{\mathrm{Mie}}$ is bounded by the inverse of the sphere's LDOS (dotted line), which leads to the suppression of $\boldsymbol{\alpha}_{\mathrm{Mie}}$ close to the antenna resonance.

$\mathrm{Im}\boldsymbol{\alpha}_{\mathrm{Mie}}$ is indeed limited by the inverse of the sphere's LDOS [Fig. 6.3(b), dotted line]. Off antenna resonance, the correction to the broad $\boldsymbol{\alpha}_{\mathrm{Mie}}$ by the narrow $\boldsymbol{G}_{\mathrm{Mie}}$ creates characteristic Fano resonances due to the dispersive shift of the antenna resonance frequency by the real part $\mathrm{Re}\,\boldsymbol{G}_{\mathrm{Mie}}$. The transition from enhancement to inhibition in the lumped LDOS going from weak to strong scattering is captured by amending the antenna factor A in Eq. (6.1) with Eq. (6.3), such that when neglecting the real frequency shift the radiated power reads

$$P \propto \left|\boldsymbol{\alpha}_0^{-1} - \mathrm{i}\,\mathrm{LDOS}_{\mathrm{B}}\right|^{-2} \mathrm{LDOS}_{\mathrm{B}}. \tag{6.7}$$

For small $\boldsymbol{\alpha}_0$, i.e. in the limit of weak scattering, $P \propto |\boldsymbol{\alpha}_0|^2 \mathrm{LDOS}_{\mathrm{B}}$. In this limit of weak scattering a high background LDOS indeed increases the power radiated by the scatterer. This increase of radiated power arises since weak Rayleigh scatterers *are* constant-current sources unaffected by the unitary limit [32]. Therefore, for weak scatterers a simple multiplicative lumping rule holds. In the limit of strong scattering $P \propto \mathrm{LDOS}_{\mathrm{B}}^{-1}$, since a scatterer at the unitary limit is *not* a constant-current source [33, 34], since its dipole moment $\boldsymbol{p} = \boldsymbol{\alpha}\boldsymbol{E}$ depends on the polarizability, which is in turn inversely proportional to the LDOS according to Eq. (6.5). Therefore, close to antenna resonance, the enhancement of the hybrid system [solid line in Fig. 6.2(b)] follows the *inverse* of the Mie sphere's LDOS. We point out that Eq. (6.7) is generally valid for any antenna in any background system and therefore carries over to environments with highly non-Lorentzian LDOS such as hyperbolic and polaritonic media, epsilon-near-zero materials and the van-Hove singularities at the bandedge of photonic crystals.

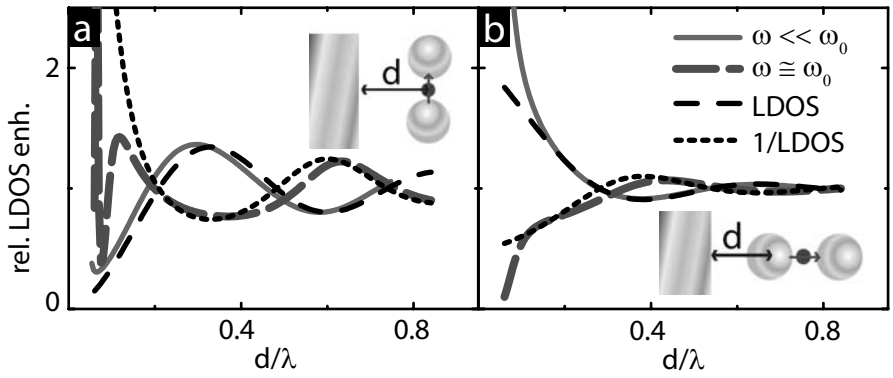

Figure 6.4: Relative LDOS enhancement for superemitter as a function of distance to a near-perfect mirror. (a) Superemitter oriented parallel to mirror surface [see inset]. Solid line: Superemitter with source far below antenna rensonance [$\omega = 4.0 \times 10^{15}\,\mathrm{s}^{-1}$, cf. Fig. 6.1(b)] traces the LDOS of the mirror [dashed line], except at small superemitter-mirror separations. A source close to antenna resonance [long-dashed line, $\omega = 4.5 \times 10^{15}\,\mathrm{s}^{-1}$] traces the inverse of the mirror LDOS [dotted line], except at small separations. (b) Same as (a) for superemitter perpendicular to mirror [see inset].

6.6 A superemitter in front of a mirror

As one example of the general validity of Eq. (6.7) beyond microcavity resonances, we examine a near-perfect mirror ($\epsilon = -200$) as a background that modifies the LDOS without any resonances [3]. In Fig. 6.4(a), we plot the decay rate of the superemitter in front of the mirror normalized to the superemitter in vacuum as a function of distance to the mirror. The antenna axis is parallel to the mirror [see sketch in inset]. Far below antenna resonance, the enhancement [Fig. 6.4(a), solid line] follows the mirror LDOS [dashed line] as expected from the multiplicative LDOS lumping rule. Close to antenna resonance [long-dashed line in Fig. 6.4(a)] the antenna is close to the unitary limit and therefore the total rate enhancement follows the inverse of the mirror LDOS [dotted line]. At intermediate frequencies we observe a smooth transition between the two cases illustrated in Fig. 6.4 (data not shown). For the superemitter oriented perpendicularly to the mirror [Fig. 6.4(b)] we observe the analogous behavior as for the parallel case. The product lumping rule and its cross-over to *inverse* proportionality are hence generic, and only break down for very small separations between superemitter and mirror. When the superemitter size is comparable to its distance to its own mirror image, superemitters also sense gradients in $\boldsymbol{G}$. While outside the simple lumping rule Eq. (6.7), this exciting regime, fully contained in our general formalism Eq. (6.2), is of great interest as a tailorable analogon to recent experiments on probing multipolar LDOS [35].

6.7 A superemitter in a cavity as coupled harmonic oscillators

The line-shapes found for the LDOS enhancement provided by a superemitter in a microcavity in Fig. 6.2(a) bear the finger-print features of Fano resonances and plasmon-induced transparency in nanophotonic systems [36, 37]. With the surge of plasmonic Fano resonances [36] a coupled-oscillator simile has emerged as the prime model in order to fit and discuss line-shapes of various observables that arise due to the interaction of several photonic constituents. The model used to this end has been given by Alzar *et al.* in a didactic paper in which 'electromagnetically induced transparency' is phenomenologically reproduced with classical mechanical oscillators and electrostatic RLC-circuits [38]. It is an open question in nanophotonics under which circumstances a mechanical-oscillator model can be applied to describe strongly scattering systems and how it relates to a fully electrodynamic model like our coupled-dipole formalism. Most importantly, in Section 6.5 we have found the scattering strength of the antenna and therefore the unitary limit to govern the behavior of an optical antenna in a hybrid photonic system. The question how the unitary limit would enter a mechanical-oscillator model has however remained unaddressed thus far. This section therefore treats the optical antenna coupled to a single cavity mode explicitly as coupled oscillators to identify the similarities and differences with a coupled-mechanical-oscillator model.

We start by briefly reviewing the model of Alzar *et al.* who consider two coupled harmonic oscillators, whose positions are described by spatial coordinates $x_{1,2}$, characteristic frequencies $\omega_{1,2}$, and dissipative damping rates $\gamma_{1,2}$. Furthermore, the two oscillators are coupled at a rate κ and the driving forces (normalized by the respective masses) are $F_{1,2}$, such that the equations of motion read

$$\ddot{x}_{1,2} + \gamma_{1,2}\dot{x}_{1,2} + \omega_{1,2}^2 x_{1,2} + \kappa^2 x_{2,1} = F_{1,2}. \tag{6.8}$$

Assuming a harmonic time dependence of the form $\exp[-\mathrm{i}\omega t]$ and $F_2 = 0$ the response of the first oscillator to a driving force F_1 is

$$x_1 = \chi_1 F_1 = \frac{1}{\omega_1^2 - \omega^2 - i\omega\gamma_1 + \frac{\kappa^4}{\omega_2^2 - \omega^2 - i\omega\gamma_2}} F_1, \tag{6.9}$$

where we have defined the mechanical response function χ_1. To quantitatively relate to the coupled-dipole model we need to define an observable in the mechanical model that represents the LDOS. Associating the driven oscillator with the antenna dipole moment a natural choice is to consider the work done by the driving force F_1 on oscillator x_1

$$W_1 = \langle \mathrm{Re}\, F_1 \cdot \mathrm{Re}\, x_1 \rangle = F_1^\dagger \mathrm{Im}\, \chi_1(\omega) F_1. \tag{6.10}$$

The mechanical driving force F_1 then corresponds to the electric field driving the antenna $\mathrm{Re}\, \boldsymbol{G}\boldsymbol{p}_0$ and we obtain one-to-one correspondence between the antenna factor Eq. (6.6) and the mechanical-oscillator model Eq. (6.10) if two conditions are satisfied.

First, the multiple scattering problem of an antenna in a complex background system can only be described in a coupled-oscillator framework if the antenna is small enough such that Eq. (6.4) simplifies to Eq. (6.6). Second, we still need to quantitatively map the corrected polarizability α onto the mechanical response function χ_1.

Having reviewed the mechanical-oscillator model we now relate it to our optical problem and seek the correct mapping between α and χ. To this end we consider a scatterer coupled to a single mode of a cavity. Our Ansatz follows the equations of motion for an atom in a cavity given by Haroche [39]. The 'atom' in this formalism is just a classical polarizable object with total charge q and mass m, such that in our case the antenna takes the role of Haroche's atom. The coordinate E describes the electric field of the single mode under consideration at the position of the scatterer. We denote the resonance frequency of the mode by ω_μ. The scatterer experiences a restoring force proportional to a and has a characteristic frequency ω_0 and dipole moment $p = aq$. The equations of motion of the cavity field and the scatterer read [‡]

$$\ddot{E} + \Gamma\dot{E} + \omega_\mu^2 E + \frac{4\pi q}{\mathcal{V}}\ddot{a} = 0 \tag{6.11}$$

$$\ddot{a} + \omega_0^2 a - \frac{q^2}{6\pi\epsilon_0 c^3 m}\dddot{a} - \frac{q}{4\pi\epsilon_0 m}E = \frac{q}{4\pi\epsilon_0 m}E_{\text{driv}}. \tag{6.12}$$

The driving field E_{driv} acting on the scatterer is the field generated by the source which itself has zero polarizability [40] and therefore does not provide a third equation of motion. We already set the driving of the cavity to zero in Eq. (6.11) in the assumption that the source is so close to the scatterer that it essentially only drives the scatterer. The assumption that the direct driving of the cavity by the source is negligible corresponds to neglecting the higher order terms in the derivation of Eq. (6.6) in the coupled-dipole model. In the equation of motion for the scatterer Eq. (6.12) we have introduced the Abraham-Lorentz force $F = \frac{q^2}{6\pi\epsilon_0 c^3}\dddot{a}$ which describes the radiation damping due to the coupling to the continuum of modes provided by the vacuum [2]. Alternatively, we would have had to include a sum of coupling terms to all continuum modes in Eq. (6.12). The term coupling the cavity field to the scatterer contains a volume $\mathcal{V}$. It can be thought of as a 'polarizability' of the cavity and depends on the location of the scatterer within the mode [39]. If the scatterer is positioned at the mode maximum, $\mathcal{V}$ is the mode volume of the cavity mode. The response of the scatterer to a driving field E_{driv} when coupled to the cavity is

$$p = \frac{\omega_0^2 V_{\text{scatt}}}{\left(\omega_0^2 - \omega^2 - \mathrm{i}\omega_0^2 V_{\text{scatt}}\text{LDOS}_{\text{vac}} - \omega_0^2 \frac{V_{\text{scatt}}}{\mathcal{V}} \frac{4\pi\omega^2}{\omega_\mu^2 - \omega^2 - \mathrm{i}\Gamma\omega}\right)} E_{\text{driv}}. \tag{6.13}$$

[‡] As throughout the entire Chapter we use a unit system where $E = 4\pi\epsilon_0 E_{\text{SI}}$ with E_{SI} the usual field in SI-units $[E_{\text{SI}}] = \text{V/m}$. Thereby, the LDOS and the polarizability conveniently have units $[G] = \text{m}^{-3}$ and $[\alpha] = \text{m}^3$, respectively, while the dipole moment is of units $[p] = \text{Cm}$.

Indeed, Eq. (6.13) takes the form $\frac{1}{\frac{1}{\alpha}-G^s}$ in Eq. (6.3) if

$$\frac{1}{\alpha} = \frac{1}{\alpha_0} - \mathrm{i}\,\mathrm{LDOS}_{\mathrm{vac}} \qquad \text{and} \qquad G^s = \mathscr{F}_P \mathrm{LDOS}_{\mathrm{vac}} \frac{\Gamma\omega}{\omega_\mu^2 - \omega^2 - \mathrm{i}\Gamma\omega}, \tag{6.14}$$

with the Purcell factor $\mathscr{F}_{\mathrm{P}} = \frac{3}{4\pi^2}\lambda^3 \frac{Q}{V}$. Therefore, the case of a small superemitter with a Lorentzian polarizability coupled to a single Lorentzian cavity mode can be *exactly* described as the interaction of two coupled harmonic oscillators. While this correspondence is hardly a surprise, comparison of Eq. (6.13) to Eq. (6.9) clearly shows the constraint that the unitary limit puts on the parameters that enter a coupled-mechanical-oscillator model to correctly describe the scattering problem. Importantly, the damping term γ_1 of the mechanical oscillator associated with the antenna in Eq. (6.8) must contain the scatterer's volume V_{scatt} measured against the vacuum $\mathrm{LDOS}_{\mathrm{vac}}$. The magnitude of this radiative damping is set via the inclusion of the Abraham-Lorentz force in Eq. (6.12). Furthermore, the coupling constant κ in Eq. (6.8) is strictly constrained in an electrodynamical treatment and is essentially given by the scatterer volume measured against the cavity mode volume $\frac{V_{\mathrm{scatt}}}{V}$. Therefore, while naturally included in a consistent electrodynamic model, radiation effects have to enter a mechanical-oscillator model as a *deus ex machina* to contain the unitary limit by constraining both the coupling constant κ and the damping rate γ in Eq. (6.8). That the unitary limit is not by itself a consequence of classical-oscillator models reflects the essential fact that unlike usual oscillators, optical resonances are super-radiant or sub-radiant depending on interference in the radiative continuum.

6.8 Conclusions and outlook

In conclusion, we have examined how the LDOS inside a superemitter probes the LDOS of a complex photonic environment. As a result we have provided a general lumping rule that describes the enhancement provided by an optical antenna based on its scattering strength and the LDOS of the embedding system. Generally, for any superemitter with a moderate antenna factor the LDOS enhancements of antenna and background multiply and a small superemitter will serve as an LDOS probe for a large background system, exactly as the term suggests [12]. In surprising contrast, a superemitter with an antenna at the unitary limit probes the *inverse* background LDOS, since increasing radiation damping reduces the polarizability of strong scatterers [30]. Our insights bear a plethora of exciting prospects for LDOS engineering in many background systems beyond cavity resonances including plasmonics, indefinite media and metamaterials, and van Hove singularities at photonic bandedges [41]. One might consider nano-manipulative switching of superemitters by moving them with respect to high-Q resonators [42]. Furthermore, our work could lead the quest for ultra-strong optical antennas towards counterintuitive hybrids of nano-antennas embedded in photonic bandgap devices. As a further implication, our findings shed new light on attempts to use a scatterer as a broadband probe of thermally populated modes, since

the scatterer *acquires* spectral features thanks to the environment that it probes [43–46]. Notably, hybrid photonic systems might benefit from large field enhancements inside the antenna that occur with convenient moderate-Q cavities, an exciting prospect for single-molecule detection [47].

Our findings imply that if a general lumped-circuit analogon for optical source impedances [19], i.e. LDOS, can be found, it must take into account not just the bare superemitter LDOS, but also how close the antenna is to the unitary limit. As an outlook, we therefore hint at the difficulties involved with identifying such a lumped-circuit analogon. Assuming a single scatterer in close proximity to the source, the associations provided by Greffet *et al.* [19] turn our Eq. (6.4) into the circuit equation for the dissipated power[§]

$$P = \frac{1}{2}\mathrm{Re}\, Z_{\mathrm{BG}}\, |I|^2 + \frac{1}{2}\mathrm{Re}\, \frac{1}{Z_\alpha}\, |U|^2 . \tag{6.15}$$

Here, the voltage U is associated with the field experienced by the scatterer $\mathrm{Re}\, G p_0$. Importantly, we find that the optical antenna appears here as an impedance Z_α driven by a constant-voltage source. The impedance of the background Z_{BG} is essentially the LDOS and for Z_α we find the impedance of an RLC-series circuit. In order to now lump the background and the antenna LDOS together we need to bring Eq. (6.15) into the form

$$P = \frac{1}{2}\mathrm{Re}\, Z_{\mathrm{tot}}\, |I|^2 , \tag{6.16}$$

since the LDOS has to be calculated classically as the power dissipated by a constant-current source according to Xu, Lee, and Yariv [40]. The question is therefore how the constant voltage U in Eq. (6.15) arises from the constant-current source I without requiring a 'transimpedance amplifier'. Mathematically, this problem can be simply resolved by writing $U = Z_{\mathrm{trans}} I$, where Z_{trans} corresponds to $\mathrm{Re}\, G$. Then, however, one encounters the unsatisfying situation that the background LDOS enters the circuit equivalent of an optical antenna, which then is represented by an RLC-parallel circuit, as an *inverse* resistance [19]. While this fact does corroborate our findings from multiple scattering theory, it clearly illustrates the problem of finding a consistent interpretation of the background LDOS in a lumped-circuit picture. It therefore remains an open question if a consistent lumped-circuit analogon for a multiple-scattering problem can be given at all.

[§] We use the associations $I \leftrightarrow -\mathrm{i}\omega p$, $U \leftrightarrow -E$, and $Z \leftrightarrow \frac{G}{\mathrm{i}\omega}$ [19]. We furthermore add $Z_\alpha \leftrightarrow \frac{1}{\mathrm{i}\omega\alpha}$ based on $p = \alpha E$.

References

[1] E. M. Purcell, *Spontaneous emission probabilities at radio frequencies*, Phys. Rev. **69**, 681 (1946).

[2] L. Novotny and B. Hecht, *Principles of Nano-Optics*, Cambridge University Press, Cambridge, 2006.

[3] K. H. Drexhage, *Influence of a dielectric interface on fluorescence decay time*, J. Lumin. **1-2**, 693 (1970).

[4] E. Snoeks, A. Lagendijk, and A. Polman, *Measuring and modifying the spontaneous emission rate of erbium near an interface*, Phys. Rev. Lett. **74**, 2459 (1995).

[5] P. Lodahl, A. F. van Driel, I. S. Nikolaev, A. Irman, K. Overgaag, D. Vanmaekelbergh, and W. L. Vos, *Controlling the dynamics of spontaneous emission from quantum dots by photonic crystals*, Nature **430**, 654 (2004).

[6] M. Barth, N. Nüsse, B. Löchel, and O. Benson, *Controlled coupling of a single-diamond nanocrystal to a photonic crystal cavity*, Opt. Lett. **34**, 1108 (2009).

[7] K. Vahala, editor, *Optical Microcavities (Advanced Series in Applied Physics, Vol. 5)*, World Scientific, Singapore, 2005.

[8] P. Anger, P. Bharadwaj, and L. Novotny, *Enhancement and quenching of single-molecule fluorescence*, Phys. Rev. Lett. **96**, 113002 (2006).

[9] S. Kühn, U. Håkanson, L. Rogobete, and V. Sandoghdar, *Enhancement of single-molecule fluorescence using a gold nanoparticle as an optical nanoantenna*, Phys. Rev. Lett. **97**, 017402 (2006).

[10] S. Schietinger, M. Barth, T. Aichele, and O. Benson, *Plasmon-enhanced single photon emission from a nanoassembled metal-diamond hybrid structure at room temperature*, Nano Lett. **9**, 1694 (2009).

[11] A. Kinkhabwala, Z. Yu, S. Fan, Y. Avlasevich, K. Müllen, and W. E. Moerner, *Large single-molecule fluorescence enhancements produced by a bowtie nanoantenna*, Nature Photon. **3**, 654 (2009).

[12] J. N. Farahani, D. W. Pohl, H.-J. Eisler, and B. Hecht, *Single quantum dot coupled to a scanning optical antenna: A tunable superemitter*, Phys. Rev. Lett. **95**, 017402 (2005).

[13] O. Benson, *Assembly of hybrid photonic architectures from nanophotonic constituents*, Nature **480**, 193 (2011).

[14] X.-W. Chen, M. Agio, and V. Sandoghdar, *Metallodielectric hybrid antennas for ultrastrong enhancement of spontaneous emission*, Phys. Rev. Lett. **108**, 233001 (2012).

[15] N. Engheta, A. Salandrino, and A. Alù, *Circuit elements at optical frequencies: Nanoinductors, nanocapacitors, and nanoresistors*, Phys. Rev. Lett. **95**, 095504 (2005).

[16] N. Engheta, *Circuits with light at nanoscales: Optical nanocircuits inspired by metamaterials*, Science **317**, 1698 (2007).

[17] A. Alù and N. Engheta, *Hertzian plasmonic nanodimer as an efficient optical nanoantenna*, Phys. Rev. B **78**, 195111 (2008).

[18] A. Alù and N. Engheta, *Input impedance, nanocircuit loading, and radiation tuning of optical nanoantennas*, Phys. Rev. Lett. **101**, 043901 (2008).

[19] J.-J. Greffet, M. Laroche, and F. Marquier, *Impedance of a nanoantenna and a single quantum emitter*, Phys. Rev. Lett. **105**, 117701 (2010).

[20] H. Mertens, A. F. Koenderink, and A. Polman, *Plasmon-enhanced luminescence near noble-metal nanospheres: Comparison of exact theory and an improved Gersten and Nitzan model*, Phys. Rev. B **76**, 115123 (2007).

[21] W. H. Weber and G. W. Ford, *Propagation of optical excitations by dipolar interactions in metal nanoparticle chains*, Phys. Rev. B **70**, 125429 (2004).

[22] F. J. García de Abajo, *Colloquium : Light scattering by particle and hole arrays*, Rev. Mod. Phys. **79**, 1267 (2007).

[23] C.-T. Tai, *Dyadic Green Functions in Electromagnetic Theory*, IEEE Press, 1994.

[24] M. Paulus, P. Gay-Balmaz, and O. J. F. Martin, *Accurate and efficient computation of the Green's tensor for stratified media*, Phys. Rev. E **62**, 5797 (2000).

[25] A. F. Koenderink, *On the use of Purcell factors for plasmon antennas*, Opt. Lett. **35**, 4208 (2010).

[26] E. Prodan, C. Radloff, N. J. Halas, and P. Nordlander, *A hybridization model for the plasmon response of complex nanostructures*, Science **302**, 419 (2003).

[27] C. F. Bohren and D. R. Huffman, *Absorption and Scattering of Light by Small Particles*, John Wiley and Sons, New York, 1983.

[28] I. Agha, J. Sharping, M. Foster, and A. Gaeta, *Optimal sizes of silica microspheres for linear and nonlinear optical interactions*, Appl. Phys. B **83**, 303 (2006).

[29] A. F. Koenderink, M. Kafesaki, B. C. Buchler, and V. Sandoghdar, *Controlling the resonance of a photonic crystal microcavity by a near-field probe*, Phys. Rev. Lett. **95**, 153904 (2005).

[30] R. G. Newton, *Scattering Theory of Waves and Particles*, Dover Publications, New York, 2002.

[31] B. C. Buchler, T. Kalkbrenner, C. Hettich, and V. Sandoghdar, *Measuring the quantum efficiency of the optical emission of single radiating dipoles using a scanning mirror*, Phys. Rev. Lett. **95**, 063003 (2005).

[32] M. Motsch, M. Zeppenfeld, P. W. H. Pinkse, and G. Rempe, *Cavity-enhanced Rayleigh scattering*, New J. Phys. **12**, 063022 (2010).

[33] T. Kalkbrenner, U. Håkanson, A. Schädle, S. Burger, C. Henkel, and V. Sandoghdar, *Optical microscopy via spectral modifications of a nanoantenna*, Phys. Rev. Lett. **95**, 200801 (2005).

[34] E. Castanié, R. Vincent, R. Pierrat, and R. Carminati, *Absorption by an optical dipole antenna in a structured environment*, Intern. J. of Opt. **2012**, 452047 (2012).

[35] M. L. Andersen, S. Stobbe, A. S. Sørensen, and P. Lodahl, *Strongly modified plasmon-matter interaction with mesoscopic quantum emitters*, Nature Phys. **7**, 215 (2011).

[36] B. Luk'yanchuk, N. I. Zheludev, S. A. Maier, N. J. Halas, P. Nordlander, H. Giessen, and C. T. Chong, *The Fano resonance in plasmonic nanostructures and metamaterials*, Nature Mater. **9**, 707 (2010).

[37] M. Frimmer, T. Coenen, and A. F. Koenderink, *Signature of a Fano resonance in a plasmonic metamolecule's local density of optical states*, Phys. Rev. Lett. **108**, 077404

(2012).

[38] C. L. G. Alzar, M. A. G. Martinez, and P. Nussenzveig, *Classical analog of electromagnetically induced transparency*, Am. J. Phys. **70**, 37 (2002).

[39] S. Haroche, *Cavity quantum electrodynamics*, in *Fundamental Systems in Quantum Optics: Proceedings of the Les Houches Summer School, Session LIII*, edited by J. Dalibard, J.-M. Raimond, and J. Zinn-Justin, Elsevier Science Publishers, 1992.

[40] Y. Xu, R. K. Lee, and A. Yariv, *Quantum analysis and the classical analysis of spontaneous emission in a microcavity*, Phys. Rev. A **61**, 033807 (2000).

[41] L. Verslegers, Z. Yu, Z. Ruan, P. B. Catrysse, and S. Fan, *From electromagnetically induced transparency to superscattering with a single structure: A coupled-mode theory for doubly resonant structures*, Phys. Rev. Lett. **108**, 083902 (2012).

[42] A. Mazzei, S. Götzinger, L. de S. Menezes, G. Zumofen, O. Benson, and V. Sandoghdar, *Controlled coupling of counterpropagating whispering-gallery modes by a single Rayleigh scatterer: A classical problem in a quantum optical light*, Phys. Rev. Lett. **99**, 173603 (2007).

[43] Y. D. Wilde, F. Formanek, R. Carminati, B. Gralak, P.-A. Lemoine, K. Joulain, J.-P. Mule, Y. Chen, and J.-J. Greffet, *Thermal radiation scanning tunnelling microscopy*, Nature **444**, 740 (2006).

[44] X. Liu, T. Tyler, T. Starr, A. F. Starr, N. M. Jokerst, and W. J. Padilla, *Taming the blackbody with infrared metamaterials as selective thermal emitters*, Phys. Rev. Lett. **107**, 045901 (2011).

[45] S.-Y. Lin, J. G. Fleming, and I. El-Kady, *Three-dimensional photonic-crystal emission through thermal excitation*, Opt. Lett. **28**, 1909 (2003).

[46] S. E. Han and D. J. Norris, *Control of thermal emission by selective heating of periodic structures*, Phys. Rev. Lett. **104**, 043901 (2010).

[47] F. Vollmer and S. Arnold, *Whispering-gallery-mode biosensing: label-free detection down to single molecules*, Nat. Methods **5**, 591 (2008).

7

Experimental Investigation of a Superemitter in Front of a Mirror

We experimentally investigate a superemitter in a photonic environment with dynamically tunable local density of optical states (LDOS). Our superemitter consists of a subwavelength-sized source of spontaneous emission whose decay rate is enhanced by coupling to a strongly scattering plasmonic nano-antenna. We controllably tune the LDOS experienced by the source-antenna ensemble by nano-mechanically approaching a micro-mirror to the superemitter. The decay rate of the source in the superemitter varies in proportion to the inverse of the LDOS in front of the mirror in agreement with our analytical theory. Our experimental results unambiguously confirm that the decay-rate enhancement provided by a strongly scattering optical antenna is enhanced by a reduced background LDOS and vice versa. Our results prepare the ground for designing the spectral properties of optical antennas in hybrid photonic systems via shaping the LDOS of the embedding background system.

7.1 Introduction

The study of light-matter interaction is a cornerstone of contemporary physics, mainly for two reasons. On the one hand, light is an ideal probe for a wide variety of excitations in matter thanks to their energetic overlap with optical frequencies. On the other hand, light is an equally ideal carrier of information, a virtue most impressively demonstrated

by the globe-spanning optical fiber network. There are three intimately related fundamental processes of light-matter interaction to be controlled: light emission, propagation, and absorption [1]. The latter two processes are intuitively associated with light-matter interaction. At the end of the 1960s, Drexhage demonstrated that also the process of spontaneous emission critically depends on the photonic environment of the source [2]. In a landmark experiment, Drexhage measured a modulation of the lifetime of fluorophores emitting in the visible as a function of their distance to a mirror. Arguably, being in a completely different field, Drexhage was unaware of the work of Purcell, who had suggested already in 1946 to boost the decay rate of a radio-frequency emitter by coupling it to a resonant cavity [3]. Purcell's idea was experimentally only realized four decades later to give rise to the flourishing field of cavity quantum electrodynamics (cQED) [4, 5]. Both Drexhage's and Purcell's work are nowadays well embedded in the formalism of cQED in its weak-coupling limit [6] and discussed in the terms of the local density of optical states (LDOS) [1, 7].

Decades of intensive research have generated a toolbox of mature photonic systems to control various aspects of spontaneous emission. Cavities [8], mirrors [9–11] and photonic crystals [12] are photonic building blocks that rely on interference of traveling waves, shaping the LDOS on a wavelength scale. The trend to miniaturization and the prospect of tightly integrated optical circuits have fueled the field of nanophotonics, which aims at controlling light on length scales smaller than the wavelength [1]. The prototypical nanophotonic building block for spontaneous-emission control is the optical antenna, which exploits plasmonic resonances of metal nanoparticles [13]. When a source of spontaneous emission is coupled to such a nano-antenna, the resulting 'superemitter' [14] retains the dipolar nature of the source while exhibiting a boosted spontaneous-emission rate [15, 16].

With its set of versatile, powerful and well characterized building blocks, which differ vastly in physical size and operating bandwidth, nanophotonics is at the dawn of a period of combination and integration of these functional units into 'hybrid photonic systems' [17]. We have shown in the previous Chapter 6 how photonic hybrids can both exploit the merits of the separate entities but more importantly offer additional opportunities for controlling light-matter interaction due to their mutual interaction. Most notably, we have predicted that the enhancement offered by a strongly scattering optical antenna is *inversely* proportional to the LDOS of the background system as a direct consequence of the unitary limit bounding the scattering strength of the antenna.

In this Chapter, we experimentally demonstrate the control of the enhancement provided by a plasmonic antenna by modulating the background LDOS. We couple spontaneous emitters to an optical antenna to then actively and reversibly vary the LDOS experienced by this superemitter in a controlled fashion by nano-mechanically approaching a metallic mirror to the source-antenna ensemble. In this variation of the classical 'Drexhage experiment', with the superemitter as the source, we indeed find the counter-intuitive behavior that the decay-rate enhancement follows the *inverse* LDOS in front of the mirror.

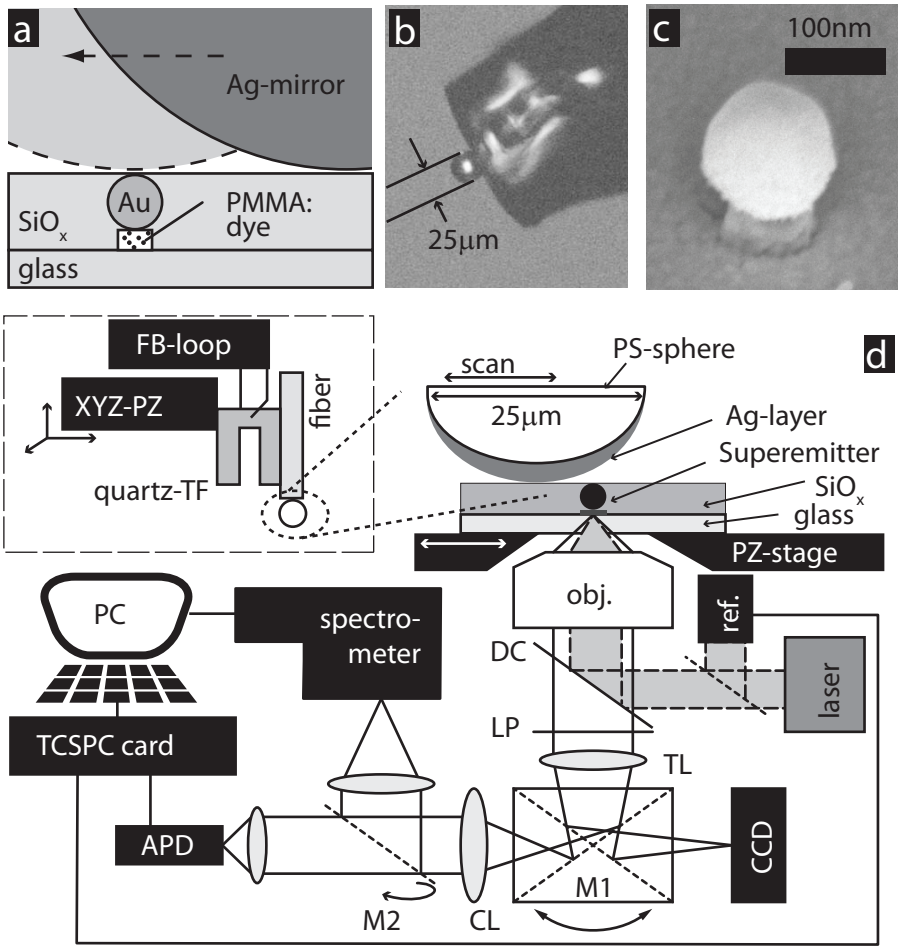

Figure 7.1: (a) Experimental principle of Drexhage experiment on a superemitter. The superemitter is composed of a Au nanoparticle residing on a dye-doped PMMA pedestal. The mirror is a large Ag-coated sphere. Scanning the mirror laterally across the sample results in different superemitter-mirror distances as shown for two positions. (b) Photograph of micro-mirror attached to end of cleaved optical fiber. (c) SEM micrograph of fabricated superemitter, composed of a Au nanoparticle residing on a dye-doped PMMA pedestal on a glass substrate. A 5 nm Au layer was sputtered on the sample for SEM imaging. (d) Sketch of experimental setup. The sample is located on a piezo scanning stage with the micro-mirror on the optical fiber located above. The optical fiber is in turn attached to a quartz tuning fork, which can be positioned with an xyz-piezo scanner [see inset]. Below the sample is a microscope objective which focuses the pump laser reflected by a dichroic mirror (DIC) on the sample. By rotating the mirror M1 the fluorescent signal filtered by a long-pass filter (LP) can be either imaged onto the CCD camera by the tube-lens (TL) or guided to either the APD or the spectrometer by mirror M2.

7.2 Controlling LDOS with a scanning mirror

Our nano-mechanical version of the Drexhage experiment is inspired by the method developed by Buchler *et al.* and relies on moving a micron-sized mirror attached to a scanning probe [10]. Our scheme of changing the distance between a fluorophore and a mirror is illustrated in Fig. 7.1(a). The fluorescing source is fixed in a substrate while a large spherical mirror is laterally moved across the sample surface. In Fig. 7.1(a) two positions of the mirror with respect to a superemitter are shown to illustrate the principle of changing the emitter-mirror distance by laterally displacing the mirror with respect to the sample. To fabricate the micro-mirror we glue polystyrene beads (diameter 25 µm, Polysciences Europe) to the cleaved end of an optical fiber with a small amount of super-glue. We subsequently evaporate a layer of 400 nm of Ag onto the sphere to obtain a spherical micro-mirror. A photograph of the fiberend with the attached sphere is shown in Fig. 7.1(b). The optical fiber is then super-glued to a quartz tuning fork, as sketched in Fig. 7.1(d, inset), which is used as a shear-force probe [1], as described in Chapter 2. With an xyz-piezo scanning head we can approach the micro-mirror to a sample surface and engage an electronic feedback loop to keep the mirror-sample distance constant [18], exploiting the shear-force interaction between the probe and the sample [1], while scanning the mirror laterally across the sample.

To demonstrate our nano-mechanical technique of changing the LDOS we prepare a sample of dye-doped polystyrene beads (diameter 100 nm, F8801, Invitrogen) dispersed at low concentration on a glass coverslip, such that individual beads are separated well beyond the diffraction limit. We furthermore evaporate about 60 nm of SiO_2 on top of the sample for mechanical protection. We put this sample of fluorescing sources onto the piezo scanning stage of our inverted confocal fluorescence-lifetime imaging (FLIM) microscope, sketched in Fig. 7.1(d). We subsequently locate a single fluorescing bead in the focus of the pump laser (532 nm, 10 MHz) generated by the objective (100×, NA 1.4), which is imaged onto an avalanche photodiode (APD). The 20 µm active area of the APD corresponds to 1 µm on the sample, leading to a confocal arrangement. The APD is connected to a timing card which records the arrival time of every detected photon with respect to the pump pulses. This way we can record the fluorescence lifetime of the dye molecules inside the polystyrene beads on the sample. With the fluorescing bead continuously in focus, we now use the scanning head of the setup to approach the micro-mirror to the sample surface, bring it into shear-force contact and raster-scan it laterally across the sample. In Fig. 7.2(a) we show a fluorescence-intensity map obtained while scanning the mirror, where each pixel corresponds to a certain horizontal position of the mirror with respect to the dye-doped bead, which leads to a certain vertical distance due to the curvature of the mirror, as seen in Fig. 7.1(a). We interpret the pronounced brightness variations observed in Fig. 7.2(a) as a result of the varying pump field experienced by the dye-doped bead when the mirror is scanned. The pump field variation is due to the interference of the incoming field and its reflections at both the mirror surface and the substrate-air interface. Using the fluorescence-lifetime imaging (FLIM) capability of our setup we analyze the arrival times of the fluorescent photons collected for every mirror position, which yields the FLIM map shown in

Fig. 7.2(b), exhibiting circularly symmetric variations in the detected lifetime. The circular symmetry of both Figs. 7.2(a) and (b) is the expected result of the symmetry of the curvature of our micro-mirror with respect to its touching point with the sample. We exploit this symmetry by determining the center of the patterns in Figs. 7.2(a,b) and averaging the signal of pixels with equal distance to the center of the distribution. When we furthermore use the diameter of the micro-mirror to convert the horizontal distances of the maps in Figs. 7.2(b) into a distance between the emitting bead and the mirror, we obtain a measurement of the decay rate of the emitters in the bead as a function of their distance to the mirror surface, shown as the full diamonds in Fig. 7.2(c). We clearly observe characteristic decay-rate oscillations in front of the mirror [2].

To theoretically model our experiments, throughout this Chapter we consider an air layer sandwiched between two semi-infinite half-spaces, the upper one being Ag ($\epsilon = -15.5 + 0.52\mathrm{i}$ at 620 nm, measured by ellipsometry on an Ag film on a Si substrate), the lower one being glass ($\epsilon = 2.25$) and a quantum yield of the emitters of 1. We thereby approximate the spherical mirror as a plane, an assumption that holds whenever the distance between the emitter and the sphere is much smaller than the sphere's radius of curvature. We calculate the LDOS in a range of depths into the glass substrate corresponding to the extent of the volume filled with emitters for a source radiating a vacuum wavelength of 620 nm, which is the emission maximum of the fluorescing beads. Subsequently, we average the obtained enhancement factors assuming a homogeneously distributed ensemble of emitter orientations [19], since approximately 10^3 dye molecules are incorporated in a bead [18]. The case of the dye-doped bead covered with an evaporated SiO_2 layer is hard to model, since it breaks the planar geometry of stratified media, which is the closest case accessible analytically [1, 20]. We still calculate the situation of stratified media but shift the obtained curve of decay rates versus mirror-sample distance by 60 nm in Fig. 7.2(c) which is the approximate height of the SiO_2 layer. The obtained correspondence of the measured data [full diamonds in Fig. 7.2(c)] with the analytical calculation (dashed curve) is fully satisfying.

While using a dye-doped bead for a reference measurement has the virtue of the source being confined to a sub-wavelength volume the protective capping layer limits how close the mirror can get to the emitters. We therefore employed an alternative geometry, where we spin coated a dye-doped layer of about 70 nm thickness of PMMA onto a glass coverslip and repeated the experiment shown in Figs. 7.2(a,b). To this end we diluted 5 mg dye (Bodipy TR, D-6116, Invitrogen) in 1 ml anisole to further dilute that mixture 30-fold in a 2% mixture of PMMA with molecular weight 950K in anisole. The PMMA mixture was then spun on base-Piranha cleaned coverslips and baked for 5 minutes at 180°C. We note that the manufacturer does not disclose the precise type of dye incorporated in the fluorescing beads used for the measurement of the full purple diamonds in Fig. 7.2(c). Comparison of spectrum and lifetime strongly suggest that the dye incorporated in the beads is Bodipy TR, which we use throughout this Chapter to prepare dye-doped PMMA layers. Using a continuous dye-doped layer the spatial selection in the sample plane is solely done through the size of the pump spot, which is about 500 nm in our case. The resulting curve of measured decay rate as

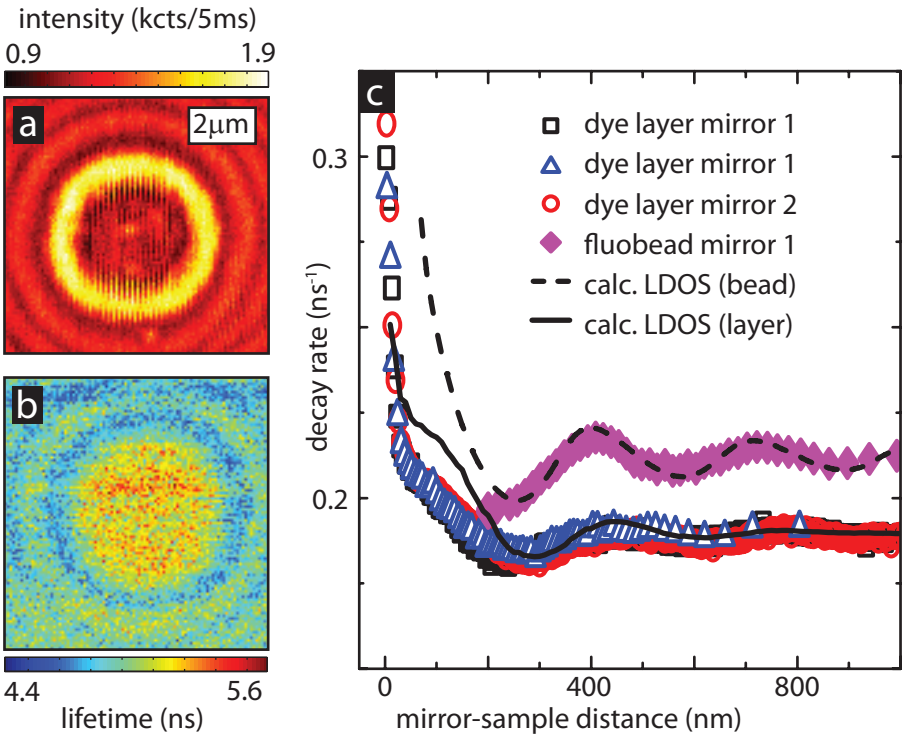

Figure 7.2: (a) Fluorescence-intensity map of dye-doped bead in laser focus as micro-mirror is scanned across it, showing ring-shaped intensity variations. A position in the map denotes the lateral position of the mirror. (b) Fluorescence-lifetime map of same measurement that yielded (a). (c) Decay rate as function of emitter-sample distance, as obtained from lifetime map shown in (b) by averaging over the pixels with identical distance to the center of the circular pattern. Full diamonds are data obtained from map in (b), measured on 100 nm fluorescing bead, while open symbols show results on continuous dye layers at different positions and with different micro-mirrors.

a function of mirror-sample distance is shown as the black squares in Fig. 7.2(c). A distance of zero on the horizontal axis corresponds to the position of the mirror being exactly above the interrogated point on the sample in the experiment and the size of the air-gap being zero in the calculation. We have repeated the experiment of probing the lifetime in a dye layer [open squares in Fig. 7.2(c)] both with the same micro-mirror at a different location on the same sample [open triangles] and with a different micro-mirror [open circles]. The resulting lifetime curves as a function of mirror-sample distance agree excellently, showing that our technique of modifying LDOS by nano-mechanical control of a micro-mirror is both fully reversible and repeatable, even with different micro-mirrors. All measurements presented in this Chapter are performed with either one of the two micro-mirrors characterized in Fig. 7.2(c). When comparing the data measured on the dye-doped bead [full diamonds in Fig. 7.2(c)] with the data obtained

on the continuous dye-doped layer [open symbols], one immediately notes the larger decay rate of the emitters in the fluorescing bead compared to the dye layer. Assuming that the molecular dye is indeed identical in the two cases, the rate of the bead is expected to be enhanced since it is entirely surrounded by high-index SiO_x while the dye layer is in immediate proximity to the air half-space. Furthermore, we note the reduced contrast in the decay-rate variations of the continuous layer as compared to the bead. This reduced contrast is a result of the larger lateral extent of the probed volume which is given by the focal size of the pump spot, which is about 500 nm, resulting in a broader distribution of distances of probed emitters from the mirror, an effect becoming increasingly severe at larger emitter-mirror separations due to the mirror's curvature, as can be appreciated from the sketch in Fig. 7.1(a). We model the experiment on the dye layer by averaging the decay-rate enhancements experienced by emitters located in a volume given by the dye-layer thickness and the focal spot-size. While the obtained analytical result, plotted as the solid line in Fig. 7.2(c), is fully satisfactory at larger sample-mirror distances, the correspondence between theory and experiment is only qualitatively correct for mirror-sample separations smaller than about 200 nm. There are several possible reasons for the observed discrepancy. First, effects like mirror-surface roughness or local surface features could have an effect at these small distances. Furthermore, the fact that we are probing an ensemble complicates things tremendously, since varying detection efficiencies for differently oriented or positioned emitters within the dye layer makes a selection of a sub-ensemble of emitters that varies with mirror distance [21, 22]. As a check, we have performed Drexhage measurements on a dye layer with annular illumination, where the pump-field component is preferentially perpendicular to the sample surface [10]. Since we found no significant effect of the illumination conditions on the lifetime measurements we exclude a selection of a sub-ensemble by the pump field. Furthermore, Mohtashami *et al.* in our group have performed Drexhage-type measurements using the technique presented in this Chapter on single NV-centers in diamond nano-crystals where effects due to sub-ensembles can be excluded. Mohtashami *et al.* have found excellent agreement between measurement and experimental data at all separations [23]. Therefore, the difference between theory and experiment in Fig. 7.2(c) can with great certainty be attributed to ensemble effects in the detection volume of finite size.

7.3 Assembly and characterization of a superemitter

Having characterized our technique of controlling the LDOS with a micro-mirror, we now turn to the fabrication and characterization of our superemitters. Schematically, our superemitters are depicted in Fig. 7.1(a). We assembled superemitters by co-localizing fluorescing dye molecules with Au colloids (diameter 100 nm, EM GC100, BBInternational). A dye-doped PMMA layer of 60 nm thickness was fabricated as described in the previous section. In a second step the Au-colloid solution was diluted 1:100 in ethanol and spin coated onto the PMMA layer. The sample was subsequently exposed to a mild oxygen descum plasma. This etching step removes PMMA and

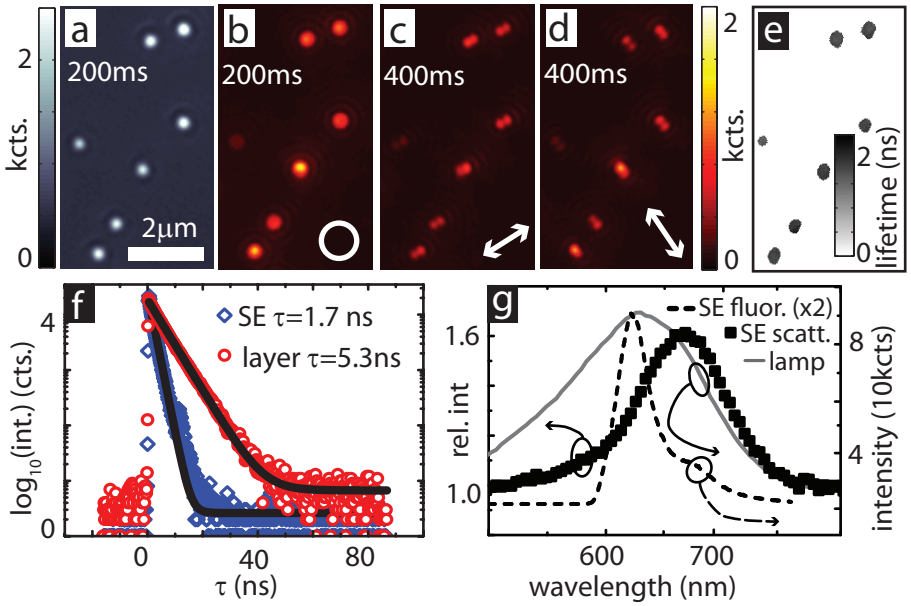

Figure 7.3: (a) CCD camera image of superemitter sample under white-light illumination, showing antenna particles as bright scatterers. (b) Unpolarized fluorescence-intensity CCD image of area in (a) under circularly polarized epi-illumination. Each superemitter appears as a bright source of fluorescence. Acquisition time 200 ms. (c) Same as (a) but with linear polarizer in detection path along direction indicated by white arrow. Acquisition time 400 ms. (d) Same as (c) but with polarizer rotated by 90°. (e) FLIM image of sample area in (a-d), showing fluorescence lifetime of superemitters between 1.5 and 2 ns. (f) Decay traces of bare dye layer (circles) and fabricated superemitter (diamonds), both fit with a single-exponential decay (solid lines), yielding a lifetime of 5.3 ns for the layer and 1.7 ns for the superemitter. (g) Scattering spectrum of an antenna particle (black squares) obtained from illuminating with a white-light source, whose spectrum is shown as the solid line. Dashed line is superemitter fluorescence emission spectrum.

embedded dye molecules from the sample surface, except under the Au colloids, where the metal particle acts as an etch mask [24]. As a result we obtain isolated Au particles residing on a dye-doped PMMA pedestal, as seen in the SEM micrograph in Fig. 7.1(c). We estimate the pedestal to contain several hundred dye molecules. Finally, we cover the sample in a thin layer of about 120 nm spin-on glass (FOX-14, Dow Corning) for mechanical protection. When illuminated with a white-light lamp and imaged on the CCD camera, the Au particles appear as bright scatterers, as shown in Fig. 7.3(a). When using the circularly polarized pump laser in epi-illumination mode the fluorescence image of the same part of the sample shown in Fig. 7.3(a) appears as shown in Fig. 7.3(b). Clearly, the positions of the scatterers strongly fluoresce. Since the molecules are located under the Au particle we expect that the dipole moment induced in the optical antenna, which dominates the emission of the superemitter, is

oriented along the optical axis [25]. Accordingly, after a linear polarization analyzer we expect the image of a superemitter to consist of a double-lobed pattern along the polarizer axis [26]. Indeed, after filtering the signal that led to Fig. 7.3(b) with a linear polarizer in the detection path we obtain Fig. 7.3(c), which shows the expected double-lobed pattern, which is furthermore practically unchanged in intensity and follows the polarization axis when the polarization analyzer is rotated, as done in Fig. 7.3(d).

To characterize the decay rate of our superemitters Fig. 7.3(e) shows a FLIM measurement of the area investigated in Figs. 7.3(a-d), where we have clamped the lifetime value of pixels holding less than 1000 events to zero. The distribution of lifetimes exhibited by the superemitters ranges from about 1.5 to about 2 ns. An example for the decay behavior of a typical superemitter is shown in Fig. 7.3(f). The decay trace of the superemitter (blue diamonds) is fitted well with a single exponential with time constant 1.7 ns. To judge the enhancement factor provided by the Au particle acting as an optical antenna the lifetime of the superemitter has to be compared to the lifetime of the dye molecules in absence of the antenna particle. To this end we also collect a decay trace in a reference section of the sample where no Au particles are present and the dye layer has been protected from the plasma etch. The decay behavior of the bare dye molecules, shown as the open circles in Fig. 7.3(f), is fitted excellently by a single-exponential decay with time constant 5.3 ns. We therefore conclude that the Au nano-antenna provides a decay-rate enhancement factor of about three.

The observed enhancement is a result of the plasmonic resonance of the Au nanoparticle [15]. To characterize the spectral matching of emitter and antenna we analyze the emission spectrum of the superemitters, shown as the dashed line in Fig. 7.3(g). The emission of the superemitter peaks around 620 nm and is broadened by a shoulder to span up to about 700 nm. The fluorescence spectrum of the superemitter closely resembles the spectrum of the incorporated dye Bodipy TR which was measured separately for a reference (data not shown, see Reference [27]). The second photonic building block of the superemitter besides the quantum emitters is the scattering antenna. To characterize the spectral properties of the antenna particle we measure the scattering spectrum of a superemitter. To this end, we illuminate the sample from above under grazing incidence with a fiber-coupled white-light lamp. We first use the spectrometer in imaging mode to position the superemitter in the center of the entrance slit of the spectrometer, which is then closed as far as possible without losing the signal. Subsequently, the grating is rotated from specular reflection to the first grating order to obtain the scattering spectrum of the antenna particle. Conveniently, the rows of the spectrometer CCD which are not overlapping the particle position yield the in-situ reference of the lamp used to illuminate the sample, shown as the solid line in Fig. 7.3(g). The black squares are the scattering spectrum of the particle obtained after dividing the spectrum collected on the CCD rows overlapping the particle position by the reference spectrum. The particle's scattering spectrum shows a resonant line-shape, peaking at about 665 nm and spanning a width of about 70 nm, while well overlapping the dye emission spectrum.

7.4 A 'Drexhage experiment' with a superemitter

We now combine the two introduced methods to modify the decay rate of a spontaneous emitter. To this end, we raster-scan our scanning micro-mirror over a superemitter while continuously measuring its lifetime. As a result we obtain the decay rate of the superemitter as a function of the distance between the sample and the micro-mirror, shown as the black squares in Fig. 7.4. The grey error-bars represent one standard deviation as obtained from the averaging procedure performed on the lifetime maps. There is a clear variation visible in the decay rate as a function of mirror-sample separation. To our knowledge, the measurement in Fig. 7.4 constitutes the first observation of the decay-rate enhancement in a hybrid photonic system with a dynamically and reversibly tunable background LDOS. To model our experimental system we exploit that our superemitters are strongly polarized along the optical axis as established from Figs. 7.3(b-d). We therefore calculate the simple case of an emitter oriented perpendicularly to the interface and located at a fixed depth of 123 nm in the glass substrate as sketched in the inset of Fig. 7.4. The optical antenna is modeled in a dipole model as a polarizable sphere of 100 nm diameter whose center is located 53 nm into the glass substrate. The polarizability of the antenna particle is described in a Drude model with characteristic frequency $\omega_0 = 3.4 \times 10^{15}\,\mathrm{s}^{-1}$ and damping rate $\gamma = 8.5 \times 10^{12}\,\mathrm{s}^{-1}$ to match it to the scattering spectrum in Fig. 7.3(g). Our model is fully

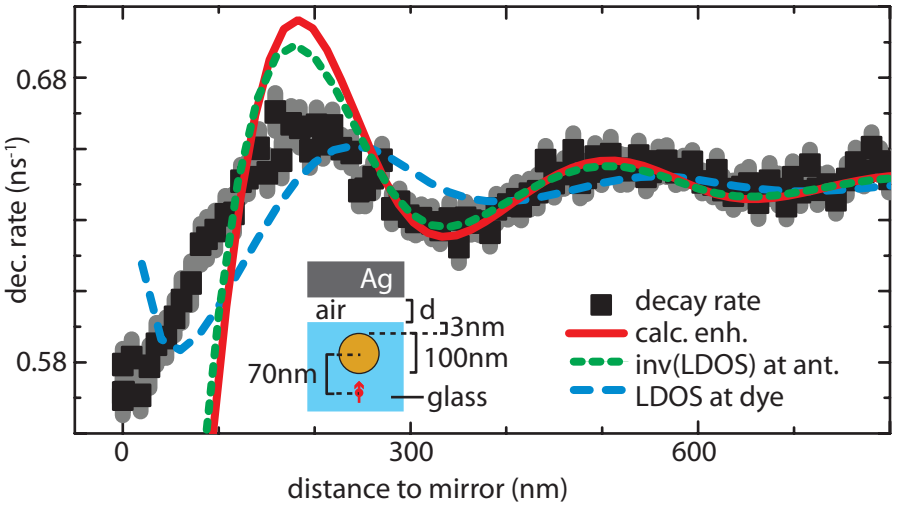

Figure 7.4: Decay rate of superemitter as function of separation to micro-mirror (black squares), where error-bars denote one standard deviation. Red line is calculated enhancement for vertically oriented source coupled to antenna (see inset for geometry) as a function of air-gap thickness. Calculated enhancement follows inverse of mirror LDOS at antenna position (green dotted line). Blue dashed line shows calculated LDOS of mirror at source position in absence of antenna particle.

analytical, yet fully electrodynamic, taking into account the full multiple-scattering process between the antenna and the double interface as detailed in Chapter 6.

The red solid line in Fig. 7.4 is the calculated decay-rate enhancement experienced by the source coupled to the polarizable particle as a function of air-gap thickness. The calculated enhancement is in excellent quantitative agreement with the measured data for mirror-sample distances larger than ca. 280 nm. At distances smaller than 280 nm there is good qualitative agreement between measurement and calculation while the measured decay-rate modifications are smaller than those theoretically predicted. We also plot the *inverse* LDOS of the mirror at the position of the antenna particle as a function of mirror-sample separation as the green dotted line in Fig. 7.4. Clearly, the enhancement calculated for the superemitter [red solid line in Fig. 7.4] closely follows the inverse LDOS in front of the mirror [green dotted line in Fig. 7.4]. This *inverse* proportionality of the superemitter enhancement factor with the background LDOS is a result of the antenna particle being a strong scatterer practically *at* the unitary limit [10, 28] as discussed in Chapter 6. Finally, to exclude that the measured variation of decay rate is the result of the dye molecules themselves experiencing the LDOS of the approaching mirror we also plot the background (i.e. mirror) LDOS at the position of the source as the blue dashed line in Fig. 7.4. Clearly, the LDOS at the source itself is incommensurable with the measured data. Figure 7.4 therefore represents the experimental confirmation that an increased background LDOS indeed *reduces* the enhancement experienced by a source coupled to a strongly scattering antenna. Regarding the discrepancy between the calculation and the measurement for very small mirror-sample distances in Fig. 7.4 we speculate that the finite size of our antenna particle starts to play a role on such small length scales.

As a final demonstration of the generality of the presented technique to assemble and probe nanophotonic systems in conjunction with a dynamically variable, much larger photonic background system, we present measurements of superemitters composed of fluorescing dye molecules coupled to nanowires, structures that have received tremendous interest as sub-wavelength LDOS modifiers [18, 29–32]. We use the same technique outlined above to co-localize fluorescing dye molecules with both Ag and GaP nanowires. Beyond plasmonic nano-structures, high-index dielectric structures are highly promising building blocks for nano-optical devices [24, 33]. We mechanically removed CVD-grown GaP nanowires with nominal diameter of 100 nm from the growth substrate and deposited them on one of our dye layers to create a superemitter with a dielectric optical antenna. A confocal fluorescence-intensity image of such a superemitter prepared from a GaP nanowire is shown in Fig. 7.5(a). While the width of the wire in this image is set by the diffraction limited imaging resolution of our setup its length is given by the physical wire length which is nominally 1 µm. The spectrum of the emitter in Fig. 7.5(a) is shown in Fig. 7.5(b) and corresponds to the emission spectrum of the used dye [cf. Fig. 7.3(g)]. The first moment of the decay trace of the detected fluorescence [inset of Fig. 7.5(b)] yields a fluorescence lifetime of 2.8 ns. In other words, the GaP wire changes the LDOS experienced by the emitters by about a factor of two. We measured the fluorescence lifetime of the superemitter assembled with the GaP nanowire while varying its distance to our micro-mirror. The

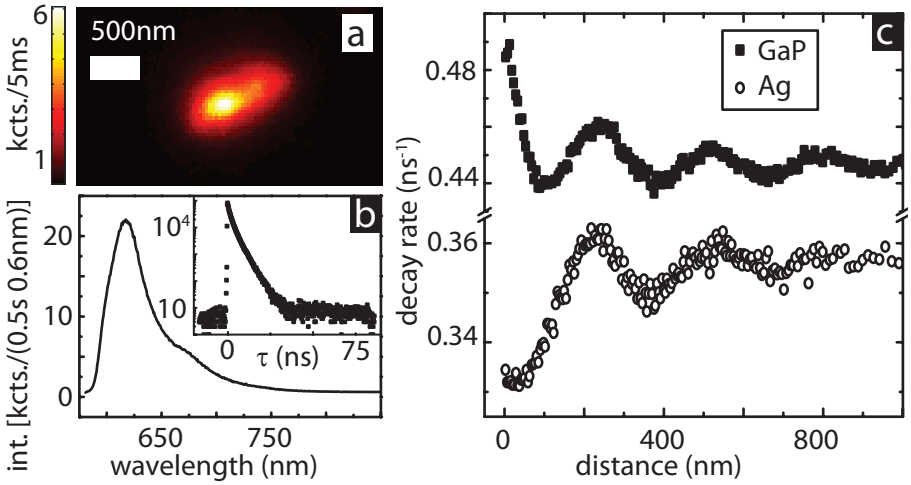

Figure 7.5: (a) Confocal fluorescence-intensity image of a superemitter manufactured from a GaP NW of nominally 100 nm in diameter and 1 µm in length. (b) Fluorescence spectrum of superemitter shown in (a), resembling the spectrum of the used dye. Inset shows fluorescence decay trace of superemitter in (a), exhibiting a slightly non-single-exponential decay. (c) Black squares: Decay rate as a function of distance to scanning micro-mirror of superemitter fabricated from GaP nanowire characterized in (a) and (b). Open circles: Decay rate as function of distance to scanning mirror of superemitter fabricated from an Ag nanowire.

resulting data-set is plotted as the black squares in Fig. 7.5(c). We can well discriminate several oscillations of the decay rate as a function of mirror-sample distance. Most notably, in this case the decay rate increases when the mirror is extremely close to sample, in contrast to our finding on the Au particle superemitter in Fig. 7.4. In a final experiment we use an Ag nanowire as a polarizable sub-wavelength object (diameter 100 nm, BlueNano Inc.). One might expect that the Ag nanowire is oxidized during the oxygen plasma etching step required for the superemitter fabrication. While we cannot make any statement about the chemical composition of the entire volume or parts of the wire, we found that Ag nanowires do act as an etch stop and we consistently found decay-rate enhancements of about two for the superemitters composed of Ag wires. The decay rate of the emitters co-localized with the Ag wire as a function of distance to the mirror is shown as open circles in Fig. 7.5(c). It is most interesting to note that the qualitative behavior of the curves of the GaP and the Ag wire resemble each other at distances larger than 200 nm, however, they are drastically different at separations smaller than 200 nm, where the decay rate of the Ag superemitter is further suppressed by the approaching mirror, while the decay rate of the GaP superemitter is further boosted by the mirror getting closer. This observed complex and counter-intuitive behavior of the LDOS modification obtained by exposing a fluorescing source to both a sub-wavelength nano-antenna and a tunable super-wavelength LDOS modification acting both on the emitter and the antenna illustrates the potential of hybrid photonic

systems for LDOS engineering.

7.5 Conclusions

In conclusion, we have coupled spontaneous emitters confined to a sub-wavelength volume to an optical antenna of sub-wavelength size, thereby creating a superemitter exhibiting a decay-rate enhancement factor exceeding three. We have furthermore exposed this superemitter to a variation of the LDOS on a length scale comparable to the wavelength by dynamically changing the distance of a metallic micro-mirror to the superemitter. As a result, we resolved a variation of the decay rate of the superemitter as a function of distance to the mirror. Importantly, the decay-rate enhancement experienced by the source in the superemitter varies in proportion to the inverse of the LDOS of the background system, as a result of the unitary limit constraining the scattering strength of the optical antenna. Our work constitutes the first example of a hybrid system composed of LDOS-shaping elements operating at vastly different sizes which is continuously tunable. Furthermore, our experiment is the first demonstration of the highly counter-intuitive behavior expected from hybrid photonic systems including strongly scattering building blocks. The system we have been studying in this Chapter is inherently broadband, since the resonance of the optical antenna is broad and the mirror as an LDOS tuning device also has no characteristic resonance. It will be most interesting to extend our study to emitters coupled to both deep-subwavelength optical antennas and super-wavelength resonators, like microsphere or microtoroid resonators, which can be manipulated nano-mechanically as well [34]. Furthermore, our results shed new light on approaches to efficiently interface single emitters via optical antennas with microresonators [35] or waveguides [36].

References

[1] L. Novotny and B. Hecht, *Principles of Nano-Optics*, Cambridge University Press, Cambridge, 2006.

[2] K. H. Drexhage, *Influence of a dielectric interface on fluorescence decay time*, J. Lumin. **1-2**, 693 (1970).

[3] E. M. Purcell, *Spontaneous emission probabilities at radio frequencies*, Phys. Rev. **69**, 681 (1946).

[4] G. Gabrielse and H. Dehmelt, *Observation of inhibited spontaneous emission*, Phys. Rev. Lett. **55**, 67 (1985).

[5] R. G. Hulet, E. S. Hilfer, and D. Kleppner, *Inhibited spontaneous emission by a Rydberg atom*, Phys. Rev. Lett. **55**, 2137 (1985).

[6] S. Haroche, *Cavity quantum electrodynamics*, in *Fundamental Systems in Quantum Optics: Proceedings of the Les Houches Summer School, Session LIII*, edited by J. Dalibard, J.-M. Raimond, and J. Zinn-Justin, Elsevier Science Publishers, 1992.

[7] R. Sprik, B. A. van Tiggelen, and A. Lagendijk, *Optical emission in periodic dielectrics*, Europhys. Lett. **35**, 265 (1996).

[8] K. Vahala, editor, *Optical Microcavities (Advanced Series in Applied Physics, Vol. 5)*, World Scientific, Singapore, 2005.

[9] E. Snoeks, A. Lagendijk, and A. Polman, *Measuring and modifying the spontaneous emission rate of erbium near an interface*, Phys. Rev. Lett. **74**, 2459 (1995).

[10] B. C. Buchler, T. Kalkbrenner, C. Hettich, and V. Sandoghdar, *Measuring the quantum efficiency of the optical emission of single radiating dipoles using a scanning mirror*, Phys. Rev. Lett. **95**, 063003 (2005).

[11] A. I. Chizhik, A. M. Chizhik, D. Khoptyar, S. Bär, A. J. Meixner, and J. Enderlein, *Probing the radiative transition of single molecules with a tunable microresonator*, Nano Lett. **11**, 1700 (2011).

[12] S. Noda, M. Fujita, and T. Asano, *Spontaneous-emission control by photonic crystals and nanocavities*, Nature Photon. **1**, 449 (2007).

[13] L. Novotny and N. van Hulst, *Antennas for light*, Nature Photon. **5**, 83 (2011).

[14] J. N. Farahani, D. W. Pohl, H.-J. Eisler, and B. Hecht, *Single quantum dot coupled to a scanning optical antenna: A tunable superemitter*, Phys. Rev. Lett. **95**, 017402 (2005).

[15] S. Kühn, U. Håkanson, L. Rogobete, and V. Sandoghdar, *Enhancement of single-molecule fluorescence using a gold nanoparticle as an optical nanoantenna*, Phys. Rev. Lett. **97**, 017402 (2006).

[16] A. Kinkhabwala, Z. Yu, S. Fan, Y. Avlasevich, K. Müllen, and W. E. Moerner, *Large single-molecule fluorescence enhancements produced by a bowtie nanoantenna*, Nature Photon. **3**, 654 (2009).

[17] O. Benson, *Assembly of hybrid photonic architectures from nanophotonic constituents*, Nature **480**, 193 (2011).

[18] M. Frimmer, Y. Chen, and A. F. Koenderink, *Scanning emitter lifetime imaging microscopy for spontaneous emission control*, Phys. Rev. Lett. **107**, 123602 (2011).

[19] W. L. Vos, A. F. Koenderink, and I. S. Nikolaev, *Orientation-dependent spontaneous emission rates of a two-level quantum emitter in any nanophotonic environment*, Phys. Rev. A **80**, 053802 (2009).

[20] M. Paulus, P. Gay-Balmaz, and O. J. F. Martin, *Accurate and efficient computation of the Green's tensor for stratified media*, Phys. Rev. E **62**, 5797 (2000).

[21] W. Lukosz and R. E. Kunz, *Light emission by magnetic and electric dipoles close to a plane interface. I. Total radiated power*, J. Opt. Soc. Am. **67**, 1607 (1977).

[22] W. Lukosz and R. E. Kunz, *Light emission by magnetic and electric dipoles close to a plane dielectric interface. II. Radiation patterns of perpendicular oriented dipoles*, J. Opt. Soc. Am. **67**, 1615 (1977).

[23] A. Mohtashami and A. F. Koenderink, to be published.

[24] V. J. Sorger, N. Pholchai, E. Cubukcu, R. F. Oulton, P. Kolchin, C. Borschel, M. Gnauck, C. Ronning, and X. Zhang, *Strongly enhanced molecular fluorescence inside a nanoscale waveguide gap*, Nano Lett. **11**, 4907 (2011).

[25] T. H. Taminiau, F. D. Stefani, and N. F. van Hulst, *Single emitters coupled to plasmonic nano-antennas: angular emission and collection efficiency*, New J. Phys. **10**, 105005 (2008).

[26] M. A. Lieb, J. M. Zavislan, and L. Novotny, *Single-molecule orientations determined by direct emission pattern imaging*, J. Opt. Soc. Am. B **21**, 1210 (2004).

[27] I. Johnson and M. T. Spence, editors, *Molecular Probes Handbook, A Guide to Fluorescent Probes and Labeling Technologies, 11th Edition*, Invitrogen, 2010.

[28] H. Mertens, A. F. Koenderink, and A. Polman, *Plasmon-enhanced luminescence near noble-metal nanospheres: Comparison of exact theory and an improved Gersten and Nitzan model*, Phys. Rev. B **76**, 115123 (2007).

[29] D. E. Chang, A. S. Sørensen, P. R. Hemmer, and M. D. Lukin, *Strong coupling of single emitters to surface plasmons*, Phys. Rev. B **76**, 035420 (2007).

[30] A. V. Akimov, A. Mukherjee, C. L. Yu, D. E. Chang, A. S. Zibrov, P. R. Hemmer, H. Park, and M. D. Lukin, *Generation of single optical plasmons in metal nanowires coupled to quantum dots*, Nature **450**, 402 (2007).

[31] A. Huck, S. Kumar, A. Shakoor, and U. L. Andersen, *Controlled coupling of a single nitrogen-vacancy center to a silver nanowire*, Phys. Rev. Lett. **106**, 096801 (2011).

[32] R. Kolesov, B. Grotz, G. Balasubramanian, R. J. Stöhr, A. A. L. Nicolet, P. R. Hemmer, F. Jelezko, and J. Wrachtrup, *Wave-particle duality of single surface plasmon polaritons*, Nature Phys. **5**, 470 (2009).

[33] R. F. Oulton, V. J. Sorger, T. Zentgraf, R.-M. Ma, C. Gladden, L. Dai, G. Bartal, and X. Zhang, *Plasmon lasers at deep subwavelength scale*, Nature **461**, 629 (2009).

[34] A. Mazzei, S. Götzinger, L. de S. Menezes, G. Zumofen, O. Benson, and V. Sandoghdar, *Controlled coupling of counterpropagating whispering-gallery modes by a single Rayleigh scatterer: A classical problem in a quantum optical light*, Phys. Rev. Lett. **99**, 173603 (2007).

[35] Y.-F. Xiao, Y.-C. Liu, B.-B. Li, Y.-L. Chen, Y. Li, and Q. Gong, *Strongly enhanced light-*

matter interaction in a hybrid photonic-plasmonic resonator, Phys. Rev. A **85**, 031805 (2012).

[36] A. Laucht, S. Pütz, T. Günthner, N. Hauke, R. Saive, S. Frédérick, M. Bichler, M.-C. Amann, A. W. Holleitner, M. Kaniber, and J. J. Finley, *A waveguide-coupled on-chip single-photon source*, Phys. Rev. X **2**, 011014 (2012).

Summary

Light has been intriguing humans since time immemorial. Our visual sense is fascinated by optical effects in our environment, may it be a sun-rise, a rainbow, a gemstone or a painting. Interestingly, the rational explanation of light provided by modern science as an electromagnetic wave together with the notion that light is absorbed and emitted in small energy quanta called photons has not at all turned light into a boring triviality. On the contrary, with growing insight into the nature of light we still stand in awe when observing the behavior of light and its interaction with matter. It is most notable that optics, as the science of light, has both retained its aesthetic appeal, while at the same time growing to a key technology enabling modern societies in numerous regards. We mention optical data transfer and storage, digital image recording, and solar cells as illustrations of the ubiquity of optical technologies in today's modern world.

At the forefront of modern optics is the study of light-matter interaction on length scales much smaller than the wavelength of light. Nanotechnology and advances in material processing have enabled the controlled structuring of a variety of materials on length scales comparable to and even significantly smaller than the wavelength of visible light. This technological development gave rise to the field of nanophotonics which aims at controlling the generation, the propagation and the absorption of light on sub-wavelength scales. Spontaneous emission is a fundamental process of light generation where a quantum mechanical system, for example a fluorescing molecule, undergoes a transition from an excited state to an energetically lower lying state under emission of a photon. We introduce the concept and the physical processes underlying spontaneous emission control in Chapter 1 to provide sufficient background information to state the scientific questions addressed in this thesis. It is well known that the process of spontaneous emission is governed both by the properties intrinsic to the quantum mechanical system undergoing the transition and the electromagnetic environment of the source. Specifically, the local density of optical states is the quantity of an electromagnetic environment that governs arguably all local optical processes, reaching beyond spontaneous emission to scattering, absorption, thermal emission and vacuum mediated forces. This thesis targets the question how the spontaneous emission of a photon can be controlled by positioning the source within an electromagnetic environment that has been deliberately structured at a sub-wavelength

scale. In particular, we are interested in controlling *when* the source emits and *where* the generated photon is emitted to. To this end we have constructed a microscope that can image the local density of optical states.

In Chapter 2 we outline the technical aspects of our scanning emitter fluorescence lifetime imaging microscope. We review the achievements of the nanophotonics community towards imaging the local density of optical states on a sub-wavelength scale. Furthermore, we detail the technical requirements and the according choices regarding components and their assembly. In a nutshell, our lifetime imaging microscope is a combination of a scanning probe near field optical microscope and a fluorescence lifetime imaging microscope. The local density of optical states is imaged by scanning a sub-wavelength sized source of fluorescence attached to a scanning probe with sub-wavelength positioning accuracy across a planar sample while monitoring the fluorescence lifetime of the source. Besides outlining the working principle of our experimental setup, Chapter 2 also illustrates the applied techniques at hand of measurements that serve as benchmarks and references for the following Chapters. We establish that our setup is capable of detecting the fluorescence of single photon sources and the scanning probe provides a resolution of about a tenth of the wavelength.

The experimental setup discussed and characterized in Chapter 2 is put to work in Chapter 3 in order to map the local density of states around noble metal nanowires of sub-wavelength diameters. Chapter 3 is a very illustrative demonstration of the local property of the local density of states and its impact on the spontaneous decay of a source of spontaneous emission. By repeatedly scanning the same source of fluorescence attached to a scanning probe across a metal nanowire we can reproducibly enhance the rate of spontaneous emission of the source by a factor of two. Furthermore, we show that when the source is positioned in close proximity of the wire, a significant fraction of spontaneously emitted photons is funneled into a guided plasmonic mode of the wire which acts as a sub-wavelength waveguide.

Having experimentally illustrated the local character of the density of optical states in Chapter 3 the following Chapter 4 is a review of the classical electrodynamic theory of scattering and spontaneous emission by electric dipoles. We provide a synopsis of the theoretical tool-set applied to discuss scattering and spontaneous emission in nanophotonic environments well described by an electric dipole model. To this end, we review the coupled dipole model and put special emphasis on the repercussions of radiation reaction governing the behavior of strong scatterers. Chapter 4 is therefore intended to prepare the reader for the subsequent Chapters which all feature electrodynamic calculations in the point dipole model.

In Chapter 5 we investigate the local density of optical states in the vicinity of a plasmonic meta-molecule. This Chapter is special in this thesis in the sense that it employs a beam of high energy electrons as a means to probe the local density of states. The electron beam is focused to a sub-wavelength sized spot and the created cathodoluminescence is proportional to the radiative density of states. The structures we investigate are plasmonic heptamers, consisting of strongly scattering metallic nanoparticles arranged on the corners and the center of a hexagon. The constituent particles of the heptamers are strongly polarizable and their mutual coupling gives rise to some

peculiar optical properties. It is well known that the extinction spectrum of plasmonic heptamers features a narrow transparency window in an otherwise very broad extinction band. We find that around the spectral position of the transparency window the local density of optical states swaps from being high on the outer six particles and low on the central particle to being concentrated mainly on the central particle and low on the outer ring. Our theoretical treatment of the plasmonic heptamer in the framework of the coupled dipole model introduced in the previous Chapter 4 links the well-known far-field extinction dip to our observation of the swap of the spatial distribution of the local density of states. By exploiting the symmetry of the meta-molecule we identify well-defined eigen-modes of the heptamer. In particular, we find that two eigen-modes of the plasmonic heptamer give rise to both the near-field swap of the density of states and the far-field extinction dip. Most importantly, by interpreting the plasmonic heptamer as an optical antenna we establish that sub-radiant eigen-modes of nano-antennas, that is modes with small net-dipole moment, are promising candidates to enhance spontaneous emission of localized and well positioned sources.

While Chapter 5 was occupied with a rather complex optical antenna we turn our attention to a simple nano-antenna in a complex background system in Chapter 6. To this end we theoretically investigate a small but strongly polarizable optical antenna fed by a source of spontaneous emission whose decay rate is boosted by the antenna. We consider such a source-antenna ensemble, previously termed 'superemitter' by the literature, when it is embedded in a photonic background system that modifies the local density of optical states on a length scale comparable to the wavelength. In particular, we are interested in the effects arising due to the spontaneous emitter being exposed to both an optical nano-antenna, modifying the density of states on a length scale much smaller than the wavelength and the background system with its lifetime modification on length scales comparable to the wavelength. We identify the surprising effect that an effective and therefore necessarily strongly scattering optical antenna is spoilt by an increased local density of optical states offered by the background system. The reason for the observed spoiling is given by the unitary limit of scattering theory which strictly limits the polarizability and therefore the scattering strength of any dipolar scatterer to the inverse of the local density of optical states at the scatterer position. As a consequence, the decay rate enhancement offered by a strongly scattering optical antenna will be reduced by an increased density of states of the embedding system.

In the final Chapter 7 of this thesis we experimentally test the theoretical predictions of Chapter 6. To this end we fabricate superemitters by co-localizing fluorescing dye molecules with strongly scattering gold nano-particles acting as optical antennas, effectively increasing the decay rate of the dye molecules. As a much larger photonic background system we employ a metallic mirror, modifying the local density of states in its vicinity on a scale comparable to the wavelength. The metallic mirror is manufactured by evaporating a silver layer onto a spherical bead of several ten micrometers in diameter, which is in turn attached to the scanning probe of our near field microscope detailed in Chapter 2. Therefore, we are able to position the mirror with sub-wavelength precision with respect to the superemitter which is located on a substrate, while measuring the lifetime of the source coupled to the antenna. We

indeed find that the decay rate enhancement provided by the optical antenna is inversely proportional to the local density of optical states provided by the mirror. Therefore, Chapter 7 experimentally proves the theoretical predictions of the preceding Chapter 6. Besides the demonstration of a hybrid photonic system with dynamically tunable local density of optical states the final Chapter 7 also clearly illustrates the promises of hybrid photonic systems offering versatile and often counter-intuitive opportunities regarding the engineering of the local density of optical states.

Samenvatting

Licht heeft mensen sinds het begin der tijden geboeid. We zijn gefascineerd door optische effecten in onze omgeving, of het nu een zonsopgang, een regenboog, een diamant of een schilderij is. De rationele verklaring van licht door de moderne natuurwetenschap als een elektromagnetische golf, in combinatie met het inzicht dat licht in kleine energie quanta, ofwel fotonen, uitgezonden en geabsorbeerd wordt, heeft licht helemaal niet in een saaie trivialiteit veranderd. Juist het tegenoverstelde is het geval: ons groeiend inzicht in de eigenschappen van licht en haar interactie met materie leidt steeds tot nieuwe fascinerende inzichten. Het is verrassend dat de optica, de wetenschap van licht, zowel zijn esthetische aantrekkelijkheid heeft behouden, als dat het een technologie van vitale belang is geworden die de moderne maatschappij op verschillende manieren mogelijk maakt. Denk hierbij aan optische data transfer en opslag, digitale beeldvorming en zonnecellen als voorbeelden van de aanwezigheid van optische technologie overal in de moderne wereld.

Aan de frontlinie van de moderne optica staat de studie van interacties tussen licht en materie op lengteschalen veel kleiner dan de golflengte van licht. Nanotechnologie en ontwikkelingen in de materiaalwetenschappen hebben het mogelijk gemaakt om verschillende materialen op lengteschalen vergelijkbaar en zelfs veel kleiner dan de golflengte van zichtbaar licht te structureren, waardoor de discipline nano-optica is ontstaan. Deze discipline beoogt het uitstralen, de voortplanting, en het absorberen van licht door materie op subgolflengte schalen te controleren. Spontane emissie is een van de fundamentele processen waarbij licht ontstaat. Een quantum mechanisch systeem, bijvoorbeeld een fluorescerend molecuul, maakt een transitie van een aangeslagen, dus hoog energetische, toestand naar een energetisch lagere toestand door de emissie van een foton. We introduceren het concept en het natuurkundige proces die ten grondslag liggen aan spontane emissie in hoofdstuk 1, als achtergrondinformatie voor de wetenschappelijke vragen die in dit proefschrift besproken worden. Het is bekend dat het proces van spontane emissie bepaald wordt door zowel de eigenschappen van het quantummechanische systeem dat de transitie ondergaat, als door de elektromagnetische omgeving van de bron. Meer specifiek is de lokale dichtheid van optische toestanden de eigenschap van een elektromagnetisch omgeving die fundamenteel ten grondslag ligt aan tal van optische processen. Naast spontane emissie zijn dit

onder meer ook verstrooiing, absorptie, thermische emissie en vacuüm krachten. Dit proefschrift gaat over de vraag hoe de spontane emissie van een foton gecontroleerd kan worden door de bron in een elektromagnetische omgeving, die opzettelijk op een subgolflengte schaal gestructureerd is, te plaatsen. In het bijzonder zijn we erin geïnteresseerd te controleren wanneer de bron emitteert en waar het gegenereerde foton naartoe gaat. Daarvoor hebben we een microscoop gebouwd, die een afbeelding van de lokale dichtheid van optische toestanden kan vormen.

In hoofdstuk 2 geven we een overzicht van de technische aspecten van onze 'scanning emitter fluorescence lifetime imaging microscope'. We vatten samen wat al in het veld van nanofotonica bereikt was om de lokale toestandsdichtheid op een subgolflengte schaal af te beelden. Verder bediscussiëren we de technische voorwaarden, de keuzes die we hebben gemaakt en combinaties van apparatuur die zijn gebruikt. Kort gezegd is onze 'lifetime imaging microscope' een combinatie van een 'scanning probe near field optical microscope' en een 'fluorescence lifetime imaging microscope'. Een afbeelding van de lokale dichtheid van optische toestanden ontstaat door met een fluorescente bron, die kleiner is dan de golflengte en aan een scherpe glazen naald is geplakt, het oppervlak van een monster af te tasten met subgolflengte resolutie. Op hetzelfde moment wordt de levensduur van de bron gemeten. Naast het werkprincipe van onze microscoop, illustreert hoofdstuk 2 ook de gebruikte technieken met metingen die als referentie voor de volgende hoofdstukken dienen. We laten zien dat onze opstelling in staat is om de fluorescentie van bronnen van enkele fotonen te detecteren en dat de 'scanning probe' een subgolflengte resolutie tot ongeveer een tiende van de golflengte mogelijk maakt.

De experimentele opstelling die we in hoofdstuk 2 introduceren en karakteriseren, wordt in hoofdstuk 3 gebruikt om de lokale toestandsdichtheid rond edelmetalen nanodraden met subgolflengte diameters af te beelden. Hoofdstuk 3 is een illustratie van het lokale karakter van de dichtheid van toestanden en de invloed hiervan op een bron van spontane emissie. Door dezelfde, aan een scanning tip geplakte bron van fluorescentie herhaaldelijk over een metalen nanodraad te scannen, zijn we in staat om het proces van spontane emissie reproduceerbaar tot een factor twee te versnellen. Verder laten we zien, dat als de bron zich dicht bij het draadje bevindt, een significant deel van de spontaan geëmitteerde fotonen in een gebonden plasmonische toestand van de draad wordt geëmitteerd, omdat de draad als golfgeleider werkt. Nadat we het lokale karakter van de lokale toestandsdichtheid in hoofdstuk 3 hebben laten zien, is het volgende hoofdstuk 4 een overzicht van de klassieke elektrodynamische theorie van verstrooiing en spontane emissie door elektrische dipolen. We geven een synopsis van de theoretische hulpmiddelen die gebruikt worden bij het discussiëren van verstrooiing en spontane emissie in nanofotonische omgevingen, die door een dipool-benadering goed beschreven kunnen worden. Hiervoor geven we een samenvatting van het model van gekoppelde dipolen en leggen in het bijzonder nadruk op de gevolgen van stralingsdemping, die het gedrag van sterke verstrooiers domineert. Hoofdstuk 4 is dus bedoeld om de lezer voor te bereiden op de volgende hoofdstukken, die allemaal elektrodynamische berekeningen met het punt-dipool-model gebruiken.

In hoofdstuk 5 onderzoeken we de lokale dichtheid van toestanden in de omgeving

van een plasmonisch meta-molecuul. Dit hoofdstuk is bijzonder in dit proefschrift, omdat hier een bundel van hoogenergetische elektronen gebruikt wordt als manier om de lokale toestandsdichtheid te meten. De elektronenbundel is op een punt van subgolflengte grootte gefocust en de ontstane kathodoluminescentie is evenredig met de dichtheid van stralende toestanden. De structuren die we onderzoeken zijn plasmonische heptameren, die uit sterk verstrooiende metalen nano-deeltjes bestaan, die op de hoeken en in het centrum van een zeshoek geplaatst zijn. De deeltjes waar het heptameer van gemaakt is zijn zeer polariseerbaar en hun onderlinge koppeling leidt tot bepaalde verrassende eigenschappen. Het is welbekend dat het extinctiespectrum van plasmonische heptameren een smalle transparante band heeft binnen een verder brede extinctieband. We vinden dat rond de spectrale positie van de transparantie de ruimtelijke verdeling van de lokale toestandsdichtheid plotseling opvallend verschuift. Het maximum in de toestandsdichtheid springt namelijk ineens van de buitenring van deeltjes (golflengte aan de blauwe kant van de transparantie) naar het centrale deeltje (golflengte aan de rode kant van de transparantie). Onze theoretische discussie van het plasmonische heptameer in het gekoppelde dipool model uit het voorgaande hoofstuk 4, slaat de brug tussen de welbekende dip in de extinctie en onze observatie van de verplaatsing van de ruimtelijke verdeling van de lokale dichtheid van toestanden. Door de symmetrie van het meta-molecuul te gebruiken, identificeren we goed gedefinieërde eigentoestanden van het heptameer. In het bijzonder vinden we dat twee eigentoestanden van het plasmonische heptameer verantwoordelijk zijn voor zowel de verplaatsing van de toestandsdichtheid in het nabije veld, als de extinctie dip in het verre veld. Het belangrijkste is, dat door het plasmonische heptameer als een optische antenne te interpreteren, we kunnen laten zien dat de sub-radiante eigentoestanden van nano-antennes—dat zijn toestanden met kleine netto dipool momenten—veelbelovende kandidaten zijn om spontane emissie van gelokaliseerde en goed gepositioneerde bronnen te versnellen.

Terwijl hoofdstuk 5 over een relatief complexe antenne ging, richten we onze aandacht in hoofdstuk 6 op een eenvoudige antenne in een complexe achtergrond. We onderzoeken theoretisch een kleine, maar sterk polariseerbare, optische antenne die door een bron van spontane emissie wordt gedreven en waarvan de vervaltijd wordt versneld door de antenne. We bekijken zo'n bron-antenne ensemble, eerder in de literatuur 'superemitter' genoemd, wanneer hij zich in een fotonische achtergrond bevindt, die de lokale dichtheid van toestanden op een lengteschaal vergelijkbaar met de golflengte modificeert. In het bijzonder zijn we geïnteresseerd in de effecten die ontstaan doordat de spontane emitter zowel de antenne voelt, die de lokale toestandsdichtheid op een lengteschaal veel kleiner dan de golflengte verandert, als de achtergrond, die de levensduur op een schaal vergelijkbaar met de golflengte beïnvloedt. We identificeren het verrassende effect dat een effectieve en daarom noodzakelijk sterk verstrooiende optische antenne door een achtergrond met hogere dichtheid van toestanden minder effectief wordt. De reden voor deze verslechtering is de 'unitary limit' van verstrooiingstheorie, die de polariseerbaarheid en dus de sterkte van verstrooiing van elke dipool verstrooier bepaalt: de polariseerbaarheid kan nooit groter zijn dan de inverse van de lokale dichtheid van toestanden in de positie van de

verstrooier. Als gevolg gaat de versnelling van de vervaltijd van een bron die door een antenne is gegeven omlaag in een achtergrond met verhoogde toestandsdichtheid.

In het laatste hoofdstuk 7 testen we de theoretische voorspellingen van hoofdstuk 6 met een experiment. Hiervoor maken we superemitters door een fabricagemethode waarbij sterk verstrooiende gouden nano-deeltjes naast fluorescerende moleculen geplaatst worden. De gouddeeltjes werken als optische antennes, die de vervaltijd van de moleculen effectief versnellen. Als veel grotere fotonische achtergrond gebruiken we een metalen spiegel, die de lokale dichtheid van toestanden in zijn omgeving op een lengteschaal vergelijkbaar met de golflengte verandert. De metalen spiegel is gemaakt door een zilverfilm op een ronde bol met een diameter van enkele tientallen micrometers te dampen. De bol is vervolgens aan de 'scanning probe' van onze nabije veld microscoop vast gemaakt, die in hoofdstuk 2 beschreven is. Op deze manier zijn we in staat de spiegel met subgolflengte nauwkeurigheid ten opzichte van de superemitter te plaatsen, die zich op een substraat bevindt. Tegelijkertijd meten we de levensduur van de moleculen, die aan de antenne gekoppeld zijn. We vinden inderdaad dat de levensduurversnelling door de optische antenne omgekeerd evenredig is met de lokale toestandsdichtheid van de spiegel. Daarmee bewijst hoofdstuk 7 experimenteel de theoretische voorspellingen van hoofdstuk 6. Bovendien biedt de demonstratie van een hybride fotonisch systeem met dynamisch veranderende dichtheid van optische toestanden vele en vaak tegen-intuïtieve mogelijkheden om de lokale dichtheid van toestanden vorm te geven.

Acknowledgments

My career choice four years ago had been based on the question: Where do I learn most? My answer back then was: As a PhD student in the Resonant Nanophotonics Group at AMOLF. Here is my opportunity to now thank all the people who turned my presumption into a fact during four years.

I feel most thankful to have been taught by my supervisor Femius Koenderink who is an exceptionally dedicated teacher who has spent countless hours on my education in numerous regards. I can safely exclude that any other group leader spends equal amounts of time and effort to educate his/her students to become better scientists. I have been very lucky to have been one of the first two PhD students in the Resonant Nanophotonics Group together with Ivana, such that Femius was not only my promotor but also my daily supervisor who taught me everything from lab to writing skills, from mathematical to presentation techniques, and from programming to planning schemes.

The extraordinary educational merit of AMOLF lies in its structure with numerous relatively small groups which collaborate and interact most lively. I consider it a great gift to have received supervision and training during the colloquia and poster sessions of the Center for Nanophotonics at AMOLF. I especially thank Kobus Kuipers and Ad Lagendijk for their scientific teaching moments. I have furthermore benefited very much from the joint group meetings with the Photonic Materials group of Albert Polman and the Nano Optics group of Kobus Kuipers. My fellow students have spurred my development with their interest, input and feedback. I especially thank my fellow group members Ivana, Jeroen, Leon, Andrej, Christelle, Abbas, Felipe, Anouk, Freddy, Marianne, Marko, Per, Hinke, Bart, and Hugo. My daily life in the office could not have been more inspiring and entertaining thanks to the creative and humorous discussions with Lutz.

My scientific work would have been entirely impossible without the support of Marco S., who wrote an exceptionally great data acquisition software and Idsart and Henk, who put the electronics hardware together. I was time and again impressed by the creativity and service attitude of Iliya, who designed the custom made mechanical components, which were manufactured by my colleagues from the workshop Jan, Henk, Mark, Wouter, and Ricardo, who always had a solution available for me. Naturally, I have to acknowledge Hinco, whose talent to fix practically everything with practically

nothing keeps AMOLF running in the first place. I thank Wiebe and Rutger for their always quick and helpful IT service. Without the skill and enthusiasm of Henk-Jan the cover image of this thesis would not have been possible. I have received excellent administrative support by the staff of the UvA, especially from Joost van Mameren, Rita Vinig, and Kitty Jonker.

I have not only acquired scientific and professional skills during four years at AMOLF but I also got to know my European neighbors better. I am very thankful for the hospitality with which I have been welcomed at AMOLF. There are a couple of people at AMOLF who I want to especially mention, since they not only fulfil their professional position but also are the major carriers of the 'gezelligheid' at AMOLF. Furthermore, they have been patient victims to practise my Dutch on: I could always rely on Arnelli, who backed me up no matter what. Tatjana, the sunshine from the stock-room, made it such a pleasure to pick up single office items just for the chat. Willem, the good soul of AMOLF who so quietly does his job that one only notices when he is gone, helped me out more than once on the hardware side. Ed always had an open ear for students, especially regarding "dingen over die je niet hoeft te praten". The canteen would be dull and empty without Marga, who runs the business with such motherly friendliness. I have most appreciation for Tineke and her team who keep AMOLF clean and tidy while always maintaining their friendly attitude. It has been a great pleasure to chat with Jan v. E., who always knew about the weather at home in Bavaria.

Importantly, I could not have pursued my work at AMOLF without a home in which I felt comfortable and safe. I am most indebted to AMOLF for supplying me with such a place and I therefore thank the management team around Bart. Most importantly, it have been Wenda, Juanita, and Lenny who took care of my housing problem. Thank you girls, you solved a problem that I failed to crack. Furthermore, I thank Ivana, Marko, and Sema for sheltering me during my homeless periods.

Finally, I am most thankful for the support I received from my family during the period of my PhD and throughout my entire life. Furthermore, it has been a great relief for me to realize that my friends at home are still my friends, even with me being away most of the time. Thank you Holger, Martin, and Johannes. Thomas, thank you for proof-reading my thesis with so much care and interest. I especially thank my friends Raider and Karl-Heinz for their generous help during the last years. Last but not least I thank my friends I made in Amsterdam for the good times we spent together. Thank you Megan, Verena, Agata, Corianne, and Ruben.